Doctoral Thesis

Understanding the mechanisms of movement of kinesin motors-based molecular shuttle under external force

キネシンモーターによる分子シャトルの外力下での運動メカニズムの理解

Gifu University

Graduate School of Engineering Doctor`s Program

Applied Physics Course

MAY SWEET

June 2022

Understanding the mechanisms of movement of kinesin motors-based molecular shuttle under external force

キネシンモーターによる分子シャトルの外力下での運動メカニズムの理解

By

MAY SWEET

1183915007

PhD Advisor: Professor Takahiro Nitta

Signature:

Co-PhD Advisor: Professor Minoru Sasaki

PhD Program in Electronic and Information Systems Engineering

Applied Physics Course

Graduate School of Engineering

Gifu University

Acknowledgements

Foremost, I would like to express my sincere gratitude to my advisor Prof. Takahiro Nitta for the continuous support of my Ph.D. study and research, for his patience, motivation, enthusiasm, and immerse knowledge. His guidance helped me in all the time of my academic research, writing publication papers, writing of this thesis and daily life. I could not have imagined having a better advisor for my Ph.D. study in Japan.

I would like to thank Prof. Minoru Sasaki and Prof. Kondo for being on my thesis committee and for his co-supervision. Besides my research advisor, I would like to thank Prof. Henry Hess (Columbia University, New York) for his insightful comment and questions for my research papers.

My sincere thanks also go to Professor. Hiratsuka Yuichi, for giving me the internship opportunities in his laboratory (Japan Advanced Institute of Science and Technology) which was really influential in developing my experiment methods for my research.

I would also like to thank Dr. Yoshihara Sawada for his technical support on my study in Gifu university. I would like to thank my friends, lab mates and colleagues for a cherished time spend together in the lab, and in social settings.

I thankful my best friend or fellow lab mate, Dr. Sam Macharia (From Kenya), for the stimulating discussions, for the sleepless nights we were working together before deadlines, and for all the fun we have had over 3 years. Also, I am deeply grateful to all my teachers, international friends and Myanmar friends in Gifu University. And all thanks go to Kuroyanagi Kaoru for his unrivalled support through the years living in Japan.

In addition, I would like to thank Dr. Tanabashi and Mrs. Yoshie bottom of my heart who support me ever when I am living in Japan. Besides, I also want to express my deep appreciation to Rotary Yoneyama Scholarship Foundation Japan, especially Nishi Rotary Club members for their financial support to carry out my academic life and for warmly support during my stay in Japan. I also appreciate all the support I received from Graduate School of Engineering, Gifu University and Advance Global Program (AGP) memberships.

Last but not the least, I would like to thank my family: my parents for giving birth to me at the first place and supporting me spiritually throughout my life.

Abstract

Cells are the basic units of living organisms, and able to perform a variety of vital functions. In living cells, cytoskeletal filaments (microtubules) and the associated biomolecular motors serve for essential functions. Microtubules, long hollow cylinders made of the protein tubulin, serve as rails for the transport of cargo. Biomolecular motors are a general term for proteins that drive various movements in a living body that are essential for life activities. Among them, kinesin is one that is responsible for mass transport in a cell. The kinesin motors are working for the intracellular transport. Kinesin and microtubule intracellular transport systems can be taken out from living cells and used as a nanoscale mass transport mechanism in synthetic environments. Microtubules and kinesin motors are ideal power sources for sensing, computation, optics, and robotics because of their small size and very robust and efficient motilities. A well investigated implementation of kinesin-based microtubules is called molecular shuttle. The majority of the work in this thesis has concentrated on the use of molecular shuttles in biosensors and their basic information of mechanical systems.

Research is being conducted on a molecular shuttle when the kinesin motors are fixed to a substrate, microtubules move in one direction along the kinesin-coated surface. Since it moves with fluctuations, it can transport the material to a specific location within the device. To get to a certain location, the movement of the microtubule carrying the transport material must be controlled. Therefore, controlling the movement of microtubules using an external force has been considered. Our research focus on the movement of the molecular shuttle under external forces. The performance of molecular shuttles is determined by the nature of their trajectories, which are determined by the path persistence length of microtubules. Since this path persistence length is predicted to be equal to the filament persistence length of microtubules, which is a measure of flexural rigidity.

However, previous experiments have shown that the path and filament persistence lengths differ significantly. Using our own computer simulation, we investigate how this discrepancy arose in this study. The discrepancy between the path and filament persistence lengths was reproduced in experiments by simulating molecular shuttle movement under external forces.

The bending component of microtubules due to external force was extended more than the theory predicted, according to a close investigation of molecular shuttle movements. When the extended length is taken into consideration, the discrepancy can be explained. The information obtained in our research would lead to better control the molecular shuttle movements.

Moreover, to control the movement of molecular shuttles, external forces were commonly used. The use of external force has the drawback of causing microtubule detachment from gliding surfaces. The detachment leads to loss of cargo or sparse surface density of microtubules, which limits device performance and should be minimized. In doing so, detailed observation on the process of detachment would be helpful. However, due to its limited spatial and temporal resolution, experimental investigations are hampered. In the present study, we investigate the detailed mechanisms of molecular shuttle detachment that used a computer simulation we developed ourselves. We present a simulation study of microtubules detaching from surfaces coated with kinesin motors due to the external force. Two forms of detachment were discovered in this study due to the high spatial and time resolution of the computer simulation. The detailed mechanisms of the two modes were revealed, that could be effective in minimizing detachment. Our observation will guide the better understanding of the mechanism of the detachment of molecular shuttles driven by the kinesin motor.

This study performs the in-vitro motility assay experiment to observe the gold nanowires by attaching gold colloids to microtubules. With a scanning electron microscope (SEM), we investigated the biotinylated gold nanoparticles (AuNP) 10 nm binding to microtubules and observed the stabilization of binding on the microtubules. We confirmed that gold nanoparticles were slightly attached to the microtubules by SEM. EDX scanning was used to identify the gold nanoparticles in this study. However, we discovered that the gold nanoparticles' adhesion ratio on microtubules was low. In order to improve the gold nanoparticles' ability to bind to microtubules as nanowires, we need to improve our sample preparation technique. Our recent discovery would contribute to the development of nanoscale material manufacturing techniques, as well as the micro integration of electronic devices.

Table of Content

List of Figures

To investigate further details, we performed SEM observations for each pattern. It is considered that what seems to be a white filament is actually a microtubule, and what looks to be white particles is actually gold particles. The existence of gold particles on the microtubules was confirmed. It was determined whether the microtubules and gold particles visible in the SEM

List of Tables

Chapter 1: Introduction

1.1 Overview of background

Movement is one of the features of life, and it may be found on a variety of length ranges in the living world. We will investigate the movement of biomolecules with cytoskeleton filaments within the cell or in vitro in this study. The cytoskeleton of a cell is a protein structure that allows a cell to organize its cytoplasm, respond to stimuli, and create movement. A network of actin filaments, microtubules, and intermediate filaments make up the cytoskeleton. The myosin and kinesin families of motor proteins are related to actin and microtubule filaments, respectively. Microtubules and their corresponding motor, kinesin, are used by cells to transport cargo such as organelles and chromosomes inside the cell. The mechanism behavior of microtubule filaments, kinesin motors, and their performance are discussed in this research. The microtubule-kinesin system is being used to investigate some nanotechnological applications. This research focuses on the movement of microtubule-based molecular motors in molecular shuttles and their use in device applications.

1.2 The Cytoskeleton

The cytoskeleton is made up of filaments such as microtubules and actin, which form a complex network structure throughout the cytoplasm. Filaments are essential for cell form and function to be maintained. In addition, the filament itself responds to changes in the external environment by changing the shape and function of cells. In vertebrate history, the cytoskeleton is directly involved in cell movement, muscle contraction, and

morphological changes. It also serves as an intracellular motility device, moving organelles in the cytoplasm and splitting chromosomes during mitosis, among other things. Microtubules and actin filament are seen in Fig 1.1 of an animal cell.

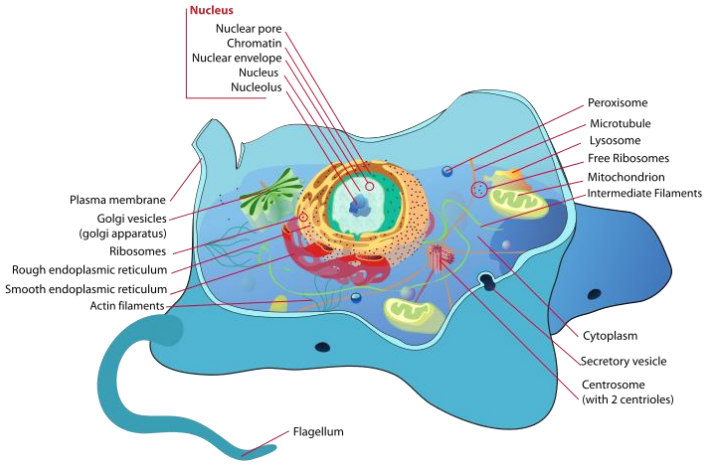

Figure 1.1: A diagram showing microtubule and actin filaments found inside a eukaryotic animal cell [1].

There are three types of filaments that play these roles: microtubule, actin filament and intermediate filaments. The microtubule filaments are the subject of this research. The function of the cell is maintained by carrying the protein produced in the cell body over it. Microtubules are fibers with a hollow tubular structure in which 13 protofilaments with a diameter of about 25 nm, it is the hardest and straightest fiber in animal cells. In animal cells, microtubules bend and align to form the mitotic spindle, which brings chromosomes together during cell division [2]. Thus, it is important to study the mechanical behavior these filaments obtain a better understanding their function as dynamic mechanical components in the cell. Researchers can now detect these filaments because to advances in simulation technology, but it still

is difficult to experimentally identify the various molecular motors that exert forces on them.

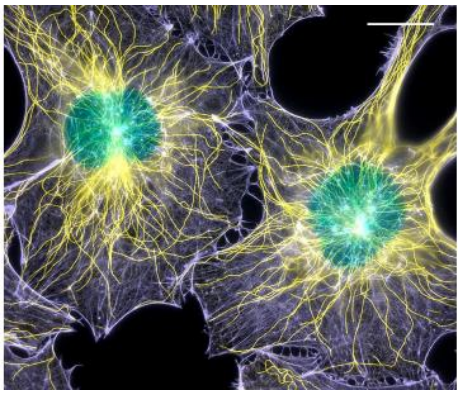

Figure 1.2: Fluorescence image of filaments of the cytoskeleton. In this cells, microtubule (yellow), actin filament (purple) and nuclei (green). The scale-bar in the upper right conner represents a distance of 15 μm. This image reproduces by the courtesy of the National Institute of General Medical Sciences [3].

1.3 Microtubule (structure and feature)

Microtubules perform a role in keeping eukaryotic cells oriented inside. Microtubules extending form the structure of the centrosome near the center of the cell spread to the cell's perimeter and act as an intercellular communication network in (Fig 1.3). Microtubules are mainly composed of two proteins, α – tubulin and β – tubulin. To make one protofilament, they are polymerized. Microtubules are formed by assembling 13 protofilaments in a 25 nm diameter circular tubular shape (Fig 1.4). Therefore, the structure of microtubules are hollow cylindrical structures generated by polymerizing tubulin, with lengths ranging from 5 to 10 nanometers. In addition, microtubules have a regular spiral shape. Tubulin is a heterodimer made up of two closely related α – tubulin, two phosphorous globular proteins, and β –

tubulin joined together by covalent bonds. The polarities of α – tubulin and β – tubulin is distinct, and microtubules that terminate at the terminus of the microtubule associated with αβ is called a negative end, while those that terminate on the side are called positive ends. Tubulin dimers are added one at a time, finally forming a hollow tubular shape (Fig 1.4). Since the chemical properties of both ends of the microtubules differ, their behaviors also differ. The polarity of structurally orientated microtubules is required for their attachment and function as completed microtubules. If microtubules have no polarity, they cannot be used in intracellular transport systems that need directionality. In addition, the subunits are organized in the same orientation on a frequent basis. Therefore, microtubules have polarity. Microtubules have a direction because of their polarity. In that direction, the positive end is the one that extends and shortens quickly and readily, whereas the negative end is the one that does not.

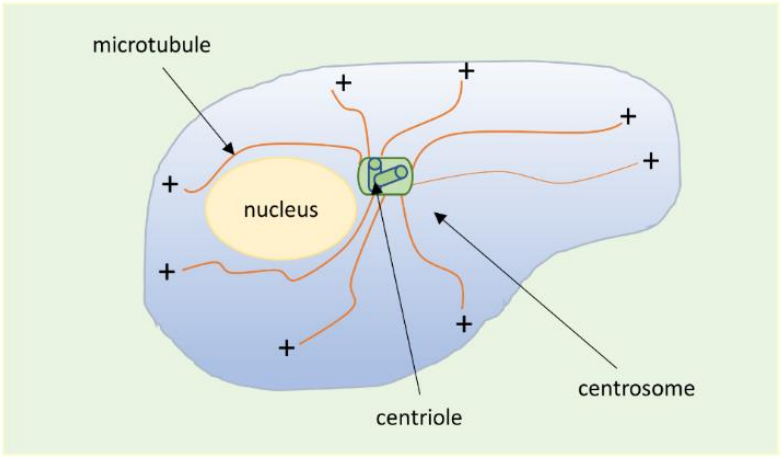

Figure 1.3: Microtubules extend out from the microtubule organizing center, which is the centrosome in animal cells.

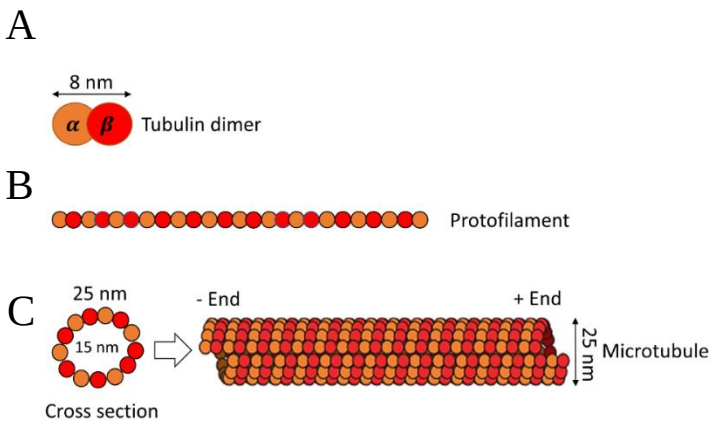

Figure 1.4: Structure of microtubule. (A) Tubulin dimers consist of α – tubulin and β – tubulin subunits. (B) Tubulin dimers join together in a head-to-tail sequence to form a protofilament. (C) 13 parallel protofilaments normally form the cylindrical and helical hollow tube microtubule wall. The polarity of the entire microtubule is parallel. Tubulin subunits are presented on one end and tubulin submits on the other. The cross-sectional area of microtubules is represented in the left circular shape figure.

1.4 Biomolecular Motor (feature and structure)

A biomolecular motor is a protein that has a motor function by itself, such as kinesin and myosin. They transfer the chemical energy when adenosine triphosphate (ATP) is hydrolyzed into adenosine diphosphate (ADP) into mechanical energy. This allows kinesin to move in one direction on microtubules and myosin to move in one direction on actin filaments. By repeating the reaction alternately on the filament, the two heads of the motor protein move as if they were walking on the filament. In this study, we deal with the kinesin motor that interacts with microtubules and has the ability to move in the microtubules plus end direction. Kinesin glides on microtubules

and uses intracellular microtubules as rails to transfer molecules required for living cell activity. They move like bipedal walking by alternately binding and dissociating with β – tubulin in microtubules. This model, which is adenosine triphosphate linked to the motor domain, is known as the hand-over-hand model (Fig 1.5). Each motor domain has two spherical head domains and a tail in (Fig 1.6). In one hydrolysis, the motor domain moves in the positive end direction of microtubules with a stride of 8nm [4][5], which is equivalent to the interval of β – tubulin in microtubules and is repeated 100 times or more per second. Because one head does not separate until the other is formed during hydrolysis, kinesin alternates between clutching microtubules and performing a "continuous digging motion." As a result, kinesin has a long range of movement and can carry cargo continuously. This hydrolysis has a high energy efficiency. In this way, kinesin moves on microtubules by converting the chemical energy released by the hydrolysis of ATP into kinetic energy [5]. This motor protein has an energy conversion efficiency of about 50% [6][7], which is significantly higher than the 35% efficiency of combustion engines used in automobiles. These properties show that kinesin is a fascinating molecular motor with potential for new nanotechnological applications. As an example of the biomolecular motors-based application, a transportation system that transports various substances in biosensor devices.

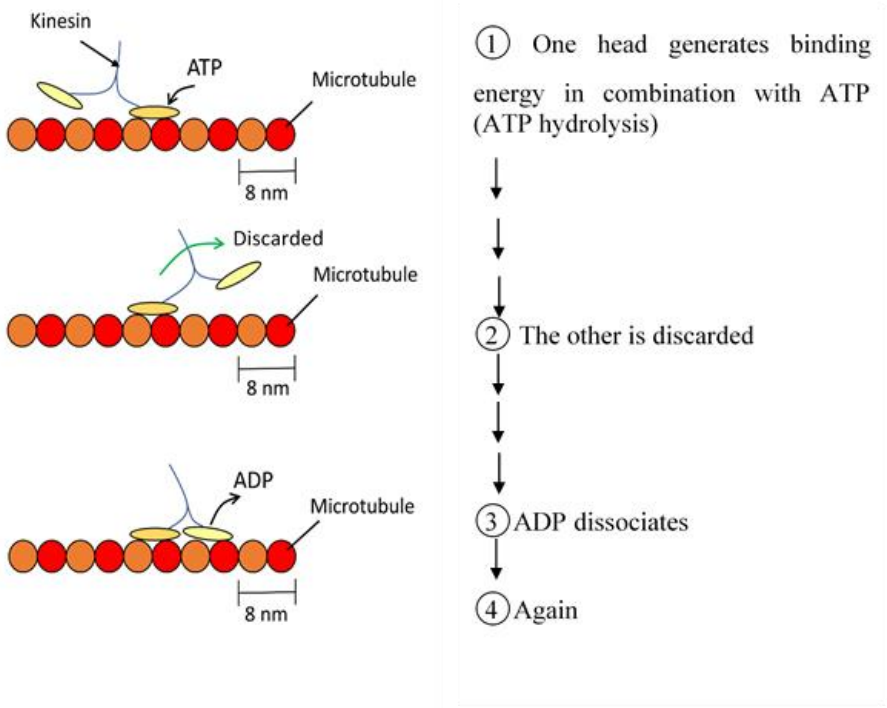

Figure 1.5: The kinesin hydrolysis cycle is presented in this diagram. According to the hand-over-hand model, kinesin travels on microtubules.

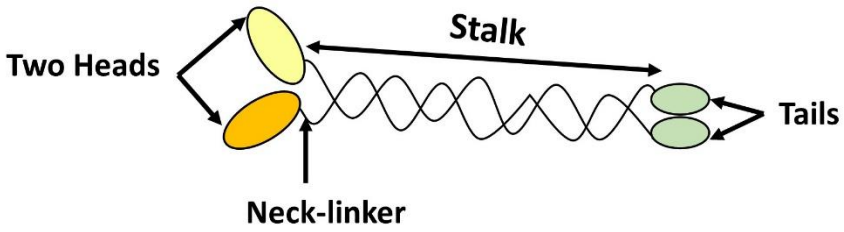

Figure 1.6: Biomolecular motor structure (Kinesin). There are two domains in the head and one in the tail.

1.5 In-vitro Motility Assay

In in-vitro assays have been used by biophysicists for a long time to investigate motor proteins and their associated cytoskeletal filaments in a synthetic environment [8][9]. Engineers have simulated the biological applications of motor proteins, particularly their role as nanoscale transport systems, using motility experiments. The geometry of the assay is most commonly inverted for in-vitro applications, with surface-attached motor proteins transporting microtubules around (commonly referred to as gliding motility assay). When microtubules are propelled by surface-bound motor proteins, the gliding experiment (Fig 1.7) can be used. The kinesin spring's high flexibility allows the motor domain to turn into a single orientation, allowing microtubule binding and movement with the minus end leading.

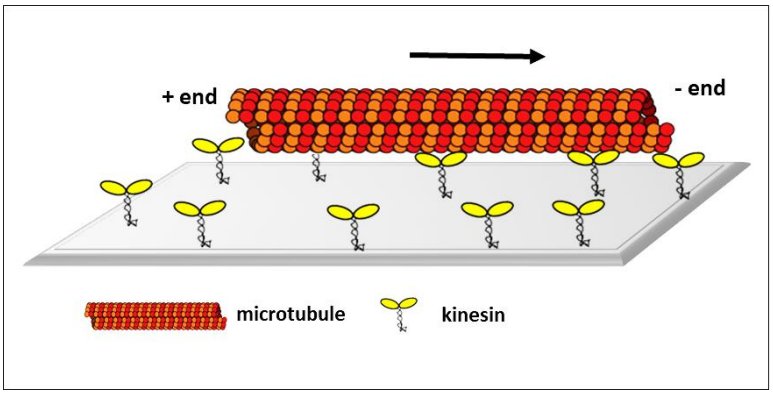

Figure 1.7: Microtubule gliding assay. The plus end directed kinesin motor is attached to a surface and drives a microtubule with its minus end.

1.6 Molecular Shuttles

Over the past several decades, progress has been achieved in the use of biomolecular motors in nanotechnology. Devices that use cytoskeletal motor proteins for molecular transport are progressing in particular. The integration of active transport into synthetic devices is inspired by active transport in cells, which uses molecular motors like kinesin and myosin. The first prototypes of molecular shuttles are hybrid devices which used motor proteins in a synthetic environment. The transportation system based on microtubules is being studied to see if it can be taken out of the living organism and used in industry. The concept is replicated in the living body by attaching kinesin to the substrate, and microtubules can be delivered in the same way. A transport chemical can be attached to a microtubule in advance and transported in this way (Figure 1.8A). This system is called a biomolecular shuttle. This molecular shuttle (MS) [7][8] takes kinesin and microtubules from cells and engineers them into a microscale mass transport device that includes biosensors. Active transport in such processes involves molecular shuttles driven by motor proteins, in which cytoskeletal filaments carrying analytes or information are carried along predefined tracks covered with related motor proteins to predetermined destinations. For driving microscopic devices, the cytoskeletal filament (microtubules) and motor proteins (kinesin) are useful power sources due to their compact size, very stable and efficient motilities in sensing, biocomputing, optics, and robotics. The performance of the device depends on the movement of molecular shuttles.

(A)

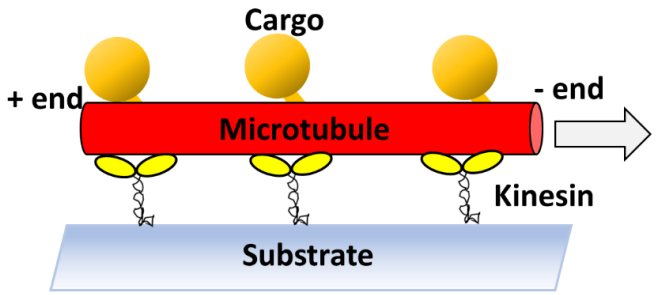
Cargo
+ end
- end
Microtubule
Kinesin
Substrate

(B)

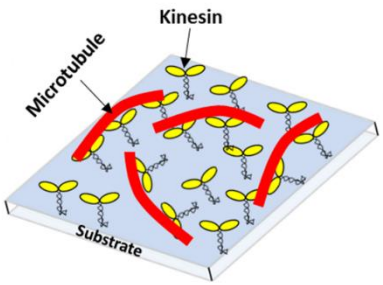
Kinesin
Microtubule
Substrate

(C)

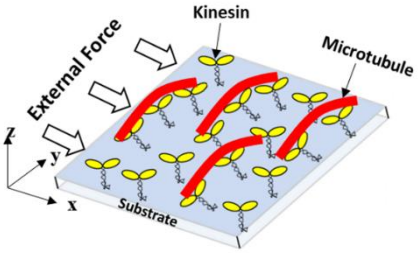
Kinesin
External Force
Microtubule
z
y
x
Substrate

(D)

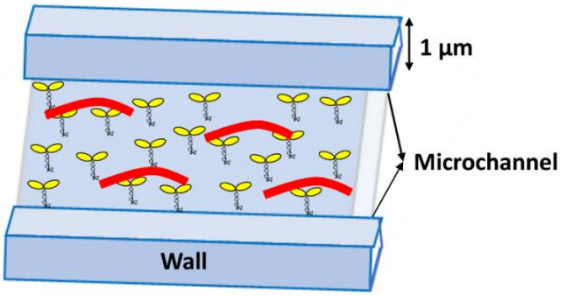
1 µm
Microchannel
Wall

Figure 1.8: On a kinesin-coated surface, microtubules transport cargo. (A) A schematic of a kinesin-driven molecular shuttle (MS) based on microtubules. (B) A schematic of microtubules moving randomly on a kinesin-coated surface. (C) A schematic illustration of a gliding microtubule in one dimension with kinesin motors under external forces. (D) Control of microtubules by microchannels.

Microtubules move randomly on a substrate uniformly coated with kinesin, constantly changing the direction of travel within a particular angle range, with fluctuations in the path in the direction of motion (Fig 1.8B). Resulting in these paths, the filament tip's Brownian motion looks for the next motor while the advancing filament is anchored to the previous motors. While some device designs can benefit from random shuttle movement, in most cases, molecular shuttles must be guided along specified trajectories. However, controlling the direction of microtubule movement is required to use it as a transportation mechanism. Furthermore, it is desirable to define a certain transport direction along the path as well as the ability to change between several paths. Therefore, as illustrated in the figures, when microtubules gliding on a kinesin-coated surface, their movement can be controlled one-dimensionally in simulation by applying external forces. (Figure 1.8C). On the other hand, it can be controlled by using photolithography microfabrication technology like microchannels (Figure 1.8D).

The purpose of this research is to identify the trajectory persistence length of microtubule filaments in detail, as well as their mechanical properties, which were discovered through simulation and experiment. This research has made it possible to simulate the motion of molecular shuttles.

1.7 Application of Molecular Shuttles

Based on the wide range of applications, the following are some general application approaches such as biosensing, biocomputation, imaging, or mapping of surface and others. Biosensor devices usually involve molecular transport systems. It's possible to obtain it from living cells and use it in synthetic environments [10][11] [12][13][14]. On biosensors [15] [16] [17] and for massively parallel computation [18], molecular shuttles transport cargo along a designated track. The majority of the work in this thesis has focused on the application of molecular shuttle biosensors, and their basic mechanical information is detailed in Chapter 3.

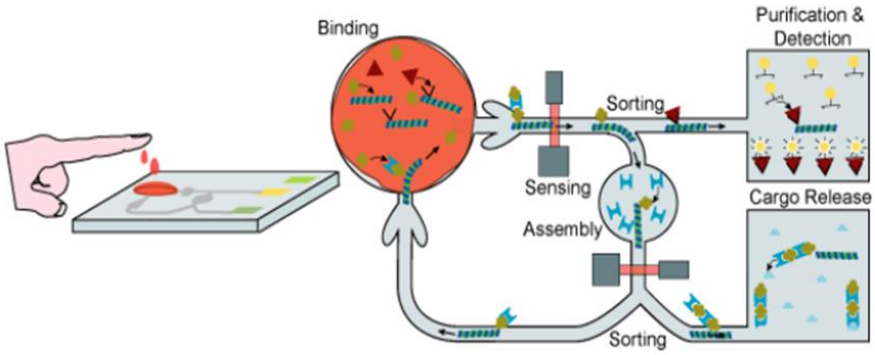

Figure 1.9: Image of Lab-on-a-Chip using molecular shuttle [19].

The most promising example of the application of the transport system by the biomolecular shuttle is the microchemical chip. A microchemical chip is an analytical device that performs numerous chemical reactions in a micrometer-wide groove (microchannel) built on a small glass substrate of several types, such as those used in blood and environmental analysis. One of the most popular is Lab-on-a-Chip (Laboratory on the chip), a microchemical device. Lab-on-a-a chip is a device that combines reagents and reaction

mechanisms on a chip the size of a fingertip that can quickly and easily examine a small amount of sample [19]. There is a plan to use a molecular shuttle for the treatment of samples from the sample injection territory to the analysis area from the outside when analyzing inside the Lab-on-a-Chip (Figure 1.9). Inside the cells, the main movement is accomplished at the nano-order scale. The sample must be transported in the right path on the microchemical chip. Therefore, at present, we currently need to develop a computer simulation technique for controlling the movement of a molecular shuttle.

Further application of molecular shuttles, which obtained the path persistence length of microtubule from a recent study, would be useful in parallel computation [18]. By using parallel processing in molecular shuttles, the microtubule-kinesin system can solve a combinatorial problem. Simulation was used to assist junction design in this study. Split and pass junctions are two different types of junctions in computational networks. The design of split-and pass-junctions for cytoskeletal filament motility in micro- and nano-fabricated channels was evaluated and optimized using simulations of motor-propelled microtubule trajectories. For scaling up biomolecular motor-based computers, the error rate created by wiggling motions at computing elements. The path persistence length should be clarified in order to reduce the error rate. Microtubule parallel computation systems can be improved by knowing the path and filament persistence length of microtubules using simulation techniques.

For predicting performance of imaging or mapping of surfaces by molecular shuttles depends on how much they move straightforward and

wiggles, which is also measured with the path persistence length. Molecular shuttles are used in a wide range of engineering applications.

Chapter 2: Methodology

2-1 Modeling and Simulation Method

The simulation method was based on our previous work [20] and extended to include external applied force to microtubules. The simulation method is simply described in the following sections. The trajectory of the molecular shuttle was modeled as a three-dimensional (3D) movement of microtubules propelled by kinesin motors. In this simulation, mainly we used the IMPLICIT and EXPLICIT (IMEX) stochastic simulation method. There have an advantages of using our developed simulation. In this simulation program, we can preset the parameter values of microtubule filament and the precise locations of bound kinesins are easily obtained in the simulation.

2-1.1 Modelling of Microtubule (Explanation of program)

In order to simulate the movement of microtubules driven by kinesin, this program follows the trajectory of beads that are assumed to exist at regular intervals on the microtubules (MTs) in (Figure 2-1.1). In this program, since the microtubules (MTs) are made of an elastic body such as a beam, a resorting force is generated according to the bending of the microtubules. We took the microtubules to be infinitely thin and inextensible semiflexible bead-rod polymers with a flexural rigidity of 22.0 pN μm^{-2} [21]. The length of MTs was set to be 5 μm and consisted of 20 rigid segments. In addition, the microtubules are in Brownian motion. The motion of this microtubule is simulated by the trajectory of the coordinates of the beads at both ends. Kinesin also calculates the interaction with microtubules as a spring. Here, the axial torque of the microtubules is not considered. Microtubules are very elongated and are not considered here because the axial torque has little effect on the movement of

the microtubules. In this simulation, the important parameters are microtubule length and bending stiffness, etc.

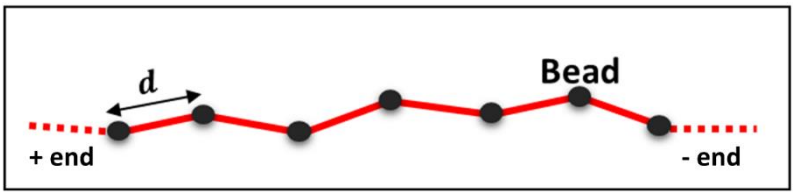

Figure 2-1.1: Microtubules are represented by the line segment connecting the beads.

The movement of microtubules are simulated by following the trajectory of beads. Microtubules do not expand or contract in the axial direction because the distance between beads are constant. The position of the bead at each time step is calculated according to the following flowchart as shown in (Fig 2-1.2).

Table 1: shows the parameters of the simulation of microtubule movement with biomolecular motors (Kinesin)

Parameters	Values	Units	References
Microtubule length	5.0	$[\mu m]$	[22]
Flexural rigidity (EI) of microtubules	22.0	$[pN.\mu m^{-2}]$	[21]
Bond length (BL) of microtubules	0.25	$[\mu m]$	[20]

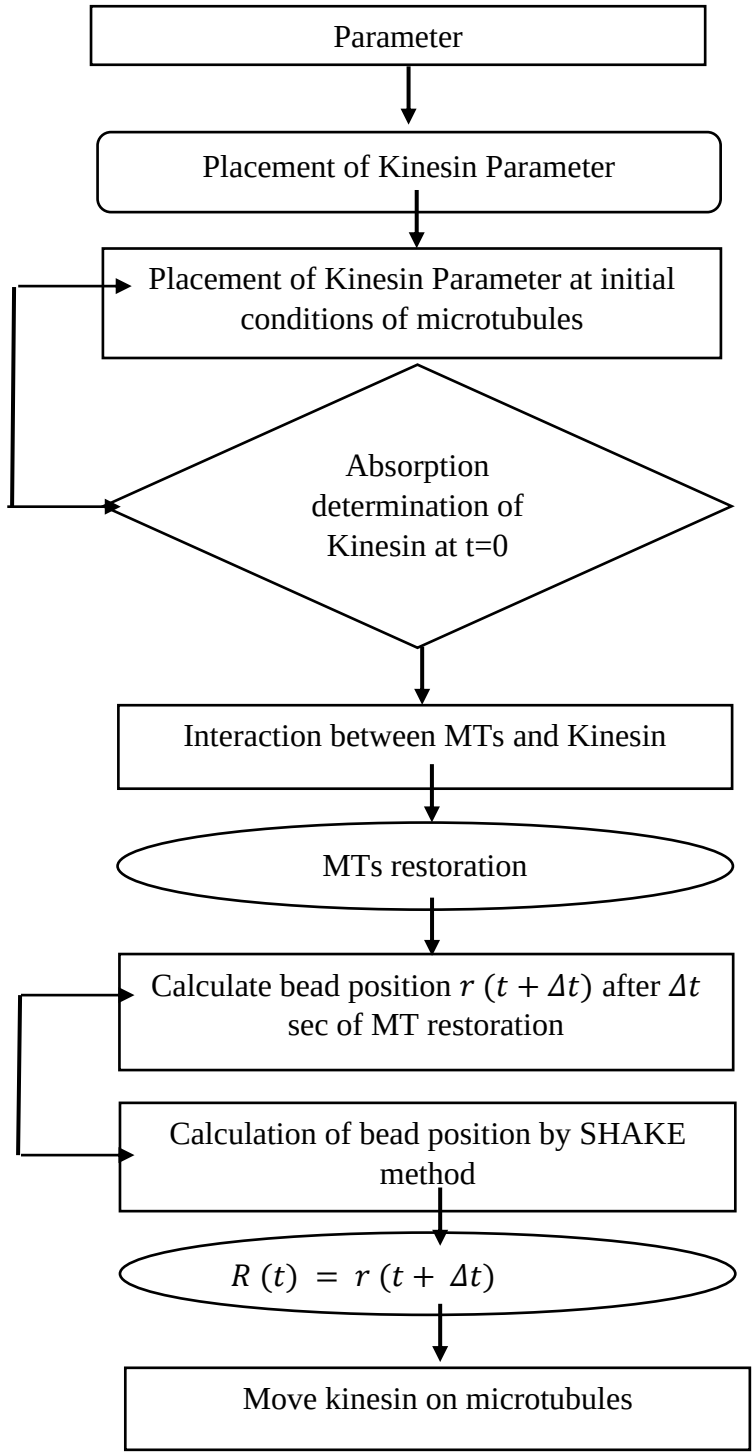
Parameter
Placement of Kinesin Parameter
Placement of Kinesin Parameter at initial conditions of microtubules
Absorption determination of Kinesin at t=0
Interaction between MTs and Kinesin
MTs restoration
Calculate bead position $r\ (t + \Delta t)$ after Δt sec of MT restoration
Calculation of bead position by SHAKE method
$R\ (t)\ =\ r\ (t +\ \Delta t)$
Move kinesin on microtubules

Figure 2-1.2: A flow chat of the main simulation program for the position of the microtubule bead on the kinesin motor surface.

2-1.2 Equation of Motion

The equation of motion of the microtubules is given by the Langevin equation as shown in eq (1).

$$\vec{0} = -\rho\overline{v}_1 - \frac{\partial \overline{U}}{\partial \overline{r}_1} + \overline{F}_{kinesin} + \overline{F}_R \qquad (1)$$

where, $\overline{r}_1$ is the bead position vector, $\overline{v}_1$ is the speed of the bead, $\overline{F}_{kinesin}$ is interaction with kinesin, $\overline{F}_R$ is random force due to collision of molecules in solution and the potential $\overline{U}$ is the bending elastic energy of the microtubule. The reason why the inertia term is zero in the eq (1) is that the movement of the microtubule is overdamped. The Reynolds number in this system is R ≈ 100, whereas R = 8×10^{-6} for microtubules [23]. If the Reynolds number is R << 1, the inertia term can be ignored for the viscous term in this case.

From eq (1), the position of the bead on the microtubule after Δt seconds is expressed by eq (2).

$$\overline{r}_i'(t + \Delta t) = \overline{r}_i'(t) + \frac{\Delta t}{\zeta}\left(-\frac{\partial \overline{U}}{\partial \overline{r}_i}\right) + \frac{\Delta t}{\zeta}\overline{F}_{kinesin} + \overline{R} \quad ,(i = 1, \dots, n) \qquad (2)$$

The return is the displacement of the bead position due to the random force. The displacement of the bead position by random force can be represented using a normal distribution having an average value of “0” and a standard

deviation of $\sqrt{2D\Delta t}$. The beads representing a microtubule are moved without considering any constraint, using the following expression:

$$\overline{r}_i'(t\ +\ \Delta t) = \overline{r}_i'(t) + \frac{\Delta t}{\zeta}\overline{F}_{bending,i} + \frac{\Delta t}{\zeta}\overline{F}_{ext} + \sqrt{2D\Delta t}\ \ N(0,1)$$

$$(\ i = 1, \dots, n) \qquad (3)$$

where ζ is the viscous drag coefficient, $\bar{F}_{bending,i}$ is the restoring force of MT bending, $\bar{F}_{bending,i}$ is a force exerted by bound kinesin, $\bar{F}_{ext}$ is an external force, $D = {k_B T}/{\zeta}$ is a diffusion coefficient and $N(0,1)$ is a normalized random number with the mean of zero and the variance of one. n is the number of beads representing the MT. Here Δt was set at $0.5 \times 10^{-6} s$ to ensure numerical stability. The viscous drag coefficient was the average of the parallel and perpendicular drag coefficient [24]. The viscous drag coefficient can be calculated from the parameter value $\zeta = {3\pi\eta d}/{ln\left(\frac{d}{2r}\right)}$, where η is the viscosity of water (0.001 Pa. s), d is the length of MT segment (0.25 μm), and r is the radius of MT (12.5 nm). If the position at t seconds and the acting force are known from the eq (3), the position after Δt seconds can be determined. By repeating this calculation, it is possible to calculate the position of the microtubule after $2\Delta t$ seconds and after $3\Delta t$ seconds. However, as described in section 2.1.1, in order to follow the trajectory of the beads, the movement of the microtubule is simulated by calculating the position of the beads after Δt seconds. In dealing with the eq (3), we used an implicit method, where the restoring force of microtubule bending is implicitly calculated. To derive the implicit term of constraint movement of microtubule in eq (3), we use the SHAKE method.

In this program, microtubules are made into elastic bodies such as beams. Naturally, when microtubules bend, bending elastic energy is generated. The bending elastic energy when a beam of length L and bending rigidity EI is bend with a radius of curvature ρ can be calculated using eq (3).

$$U = \frac{1}{2} EIL \left(\frac{1}{\rho}\right)^2 \qquad (4)$$

The radius of curvature can be calculated from the positional relationship of the beads on the microtubule. As shown in (Fig 2-1.4) let θ be the angle between the two segments formed by the i-th, $i+1st$ and $i+2nd$ beads. The angle θ can be calculated from the positions of the i-th term, the $i+1st$ and $i+2nd$ beads, and the radius of curvature of these two-line segments can be calculated from the angle θ from eq (5).

$$\rho = \frac{L}{\Delta\theta} \qquad (5)$$

The bending elastic potential of microtubules can be calculated from the position of the beads, and the force acting on each bead can be calculated.

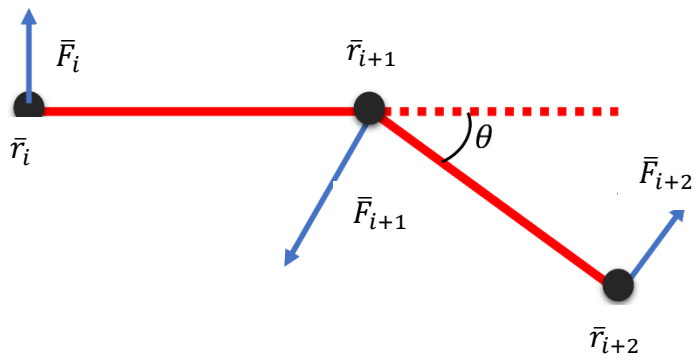

Figure 2-1.4: Force acting on beads due to bending elastic energy.

The force acting on each beads due to the bending energy can be calculated using eq (6) [24]. This calculation must be made for all line segments that represent microtubules. The calculations for the two-line segments are performed in order to the end of the microtubule from the tip, and the forces acting on the beads obtained in each calculation are superimposed.

$$\overline{F}_i = -\frac{\partial U}{\partial \bar{r}_i} \qquad (6)$$

The resorting force of MT bending was calculated from the following bending potential eq (7):

$$U = \frac{1}{2}\frac{EI}{d^3}\sum_{i=2}^{n-1}(\bar{r}_{i+1} - 2\bar{r}_i + \bar{r}_{i-1})^2 \quad (7)$$

where EI is the flexural rigidity. By substituting eq (7) into eq (6), the bending force of microtubules is calculated as follows: eq (8).

$$\overline{F}_{bending,i} = -\frac{\partial}{\partial \bar{r}_i}\frac{1}{2}\frac{EI}{d^3}\sum_{i=2}^{n-1}(\bar{r}_{i+1} - 2\bar{r}_i + \bar{r}_{i-1})^2 \quad (8)$$

2-1.3 Biomolecular motor modeling

Kinesin is modeled as a linear spring. The head and tail of kinesin are connected by a spring, and its spring constant is 100 pN/μm in (Fig 2-1.3). Table 2 shows the important parameters for that purpose. In order to investigate kinesin and microtubules to interact with each other, it is necessary to adsorb the kinesin. First, as a hypothesis, if microtubules are present in a hemisphere with a radius *w* centered on the tail of kinesin, the kinesin is considered to be adsorbed on the microtubules. In addition, regarding the

adsorption position, it is considered that the adsorption is made at the position where the distance between the tail of kinesin and the microtubule is the shortest. For one kinesin, calculate the shortest distance to the line segment between all the beads of microtubules. Then, all the line segment between kinesin and the closed bead is selected among them, and if the distance is shorter than w , it is considered to be adsorbed. The handling of this kinesin will be explained in the next section.

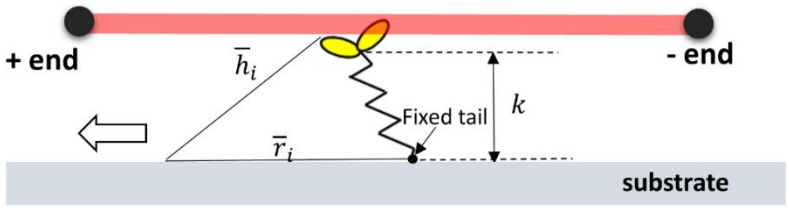

Figure 2-1.3: A schematic diagram of a kinesin motor walking on a microtubule, indicating the position of the center of mass of the microtubule between two beads, the fixed tail of the ith motor $\overline{r}_i$ on the substrate and the moving head at $\overline{h}_i$. Kinesin is a plus-end-directed motor, as indicated by the arrow marked. Note that only a small section of the microtubule is shown, because it is so much larger than the motor. Kinesin was modeled as a spring shape (k).

Table 2: Kinesin motor-related parameters used in simulation

Parameters	Values	Units	References
Kinesin spring constant, k	100	$[pN/\mu m]$	[5]

Kinesin adsorption value, w	0.02	$[\mu m]$	[5]
The load at which kinesin stops	5.0	$[pN]$	[23]
Kinesin speed without load	0.8	$[pN/s]$	[23]

2-1.4 Kinesin after adsorption

The treatment of kinesin that is not adsorbed in the previous time step, but this will explain the treatment of kinesin that has already been adsorbed. Kinesin is a thread that sticks to microtubules. The moving speed of kinesin depends on the magnitude of the load applied to the kinesin head in (Fig 2-1.4). The speed of movement of kinesin depends on the load generated by the interaction with microtubules. Therefore, in this simulation, the speed of movement of kinesin depends on the bead generated by the interaction with microtubule and the head of the bound kinesin motor moved toward the microtubule plus end with a force-dependent velocity is calculated using eq (28),

$$v(F_{pull}) = v_0\left(1 - \frac{F_{pull}}{F_{stall}}\right) \quad (9)$$

where v_0 is the translational velocity without applied force. Here, F_{pull} is the component of the pulling force along the microtubule, and F_{stall} is the stall force of the kinesin motors. v_0 is the moving speed of kinesin in the absence of load, its set at 0.8 μm/s, and F_{stall} is the magnitude of the load at which kinesin stops, its set at 5 pN.

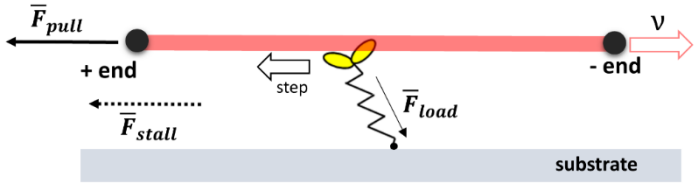

Figure 2-1.4: Schematic diagram of the force-dependent velocity of bound kinesin motor toward the plus end of microtubule.

The pulling force was divided into two forces which acted on the two beads located at either end of the microtubule segment where the kinesin motor was bound, under the condition that the total force and torque on the segment remained the same. A kinesin motor bound to a microtubule detached when tension reached 7 pN in (Fig 2-1.5). By following the approach taken by Gibbons et al., [23] we neglected the spontaneous dissociation of the bound kinesin from the microtubule.

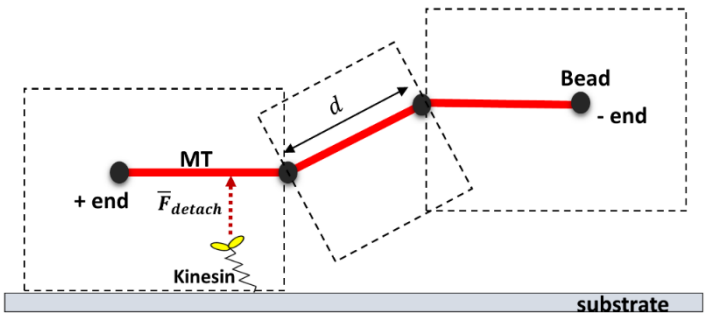

Figure 2-1.5: Schematic drawing of the molecular motors (Kinesin) detach movement on microtubule. An unbound motor (Kinesin) is represented by a position. Attachment occurs on the closet site on the microtubule bead-segment, provided this site is within a distance from the kinesin head and microtubule (red dashed lines). When the filament load is not straight, the gaps and overlaps exactly compensate each other.

2-1.5 Interaction between kinesin and microtubule

For the interaction between kinesin and microtubules, the interaction is calculated from the elongation of kinesin using kinesin as a linear spring. From section 2-1.4, the distance between the head and the tail of kinesin adsorbed on microtubules can be known, so that the force exerted by kinesin on microtubules can be calculated. However, it should be noted that the force acting on the microtubule must be distributed to the beads of the microtubules. This is because the movement of microtubule is simulated by following the trajectory of the beads. Here, the bound kinesin exerted a pulling force on the microtubule segment. The pulling force was divided into two forces which acted on the two beads located at either end of the microtubule segment where the kinesin motors was bound, under the condition that the total force and torque on the segment remained the same.

2-1.6 Constraints on microtubule length

In order to reproduce the phenomenon of microtubule network formation, the total length of microtubules must be constant. Therefore, the constraint for simulating the movement of microtubules is that the distance between the beads is always constant. The distance between the beads is constant means that the microtubules do not expand and contract in the axial direction. Consider the constraint condition g , where the distance between beads is always d.

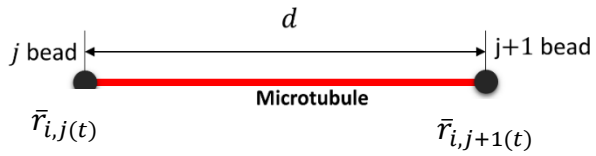

Figure 2-1.6: The distance between the bead j and the bead $j+1$ in the microtubule i and the bead j and the bead $j+1$ is always constant d due to the confinement condition.

If the distance between the beads is large when calculating the position of the beads after Δt seconds in the calculation eq (3), the constraint condition is satisfied by giving a displacement due to the binding force. Let the position of the beads can be calculated at this time in eq (10). The formula for calculating γ differs depending on the constraint, but the value of γ that satisfies the constraint condition g_1 calculated using eq (7a). To keep the segment length constant, the coordinates of the beads representing the microtubule $\{r_i\}$ as shown were subject to the following holonomic constraints:

$$g_1 = (\overline{r}_{i+1}(t) - \overline{r}_i(t))^2 - d^2 = 0 \qquad (10)$$

In order to correct the position of the beads for one constraint g_n, the equation of the motion in eq (4) is solved with the constraint added to eq (3). From eq (3), the position of the bead eq (5) after Δt seconds satisfying the constraint condition g_n is calculated and the position of the bead is corrected. However, in eq (10), it is not possible to determine the detention power in advance. An undetermined multiplier is determined so that the constraint condition satisfied at $t = t$ is also satisfied at $t = t + \Delta t$. Here eq (11) is

replaced with eq (12) using to omit the description. Since the formula for calculating the value of γ differs depending on the constraint conditions, details will be described in section 2-1.7.

$$0 = -\rho v_{i,j} + \bar{F}_{kinesin} + \bar{F}_R + \lambda_n \frac{\partial g_n}{\partial \bar{r}_i} \quad (10)$$

$$\bar{r}_{i,j}(t + \Delta t) = \bar{r}_{i,j}(t) + \frac{\Delta t}{\rho}\bar{F}_{kinesin} + \sqrt{2D\Delta t}N(0,1) + \frac{\Delta t}{\rho}\lambda_n \frac{\partial g_n}{\partial \bar{r}_{i,j}} \quad (11)$$

Rewrite the eq (10) to eq (11) by using the eq (12),

$$\gamma = \frac{\Delta t}{\rho}\lambda_n \quad (12)$$

$$\bar{r}_{i,j}(t + \Delta t) = \bar{r}_{i,j}(t) + \frac{\Delta t}{\rho}F_{kinesin} + \sqrt{2D\Delta t}N(0,1) + \gamma\frac{\partial g_n}{\partial \bar{r}_{i,j}} + \overline{R} \quad (13)$$

The calculation of γ depends on the constraints. Therefore, the calculation of γ under the constraint condition by the wall of the container is performed.

$$\gamma_1 = \frac{\|\overline{r_{i+1}'}(t + \Delta t) - \overline{r_i'}(t + \Delta t)\|^2 - d^2}{4\{\overline{r_{i+1}'}(t + \Delta t) - \overline{r_i'}(t + \Delta t)\}.\{\overline{r_{i+1}}(t) - \overline{r_i}(\Delta t)\}} \quad (14)$$

The position of the bead moved without adding a constraint condition is corrected by a holonomic constraint satisfying the constraint condition.

2-1.7 Keep microtubule above the substrate

We also use the SHAKE method for confinements in our simulation program. If z < 0, g = z – 0 (to keep microtubule above the substrate). When simulating the movement of microtubules on a transport truck, it must be ensured that the microtubules do not sink into the substrate or walls of the transport truck. For that purpose, a reaction force must be received from the

substrate or the wall at the moment when the microtubule collides with the substrate or the wall. The reaction force received from the substrate, or the wall can be calculated as a constraint force based on the binding condition that the microtubule does not sink into the substrate or the wall. Restraint conditions vary depending on the transport truck.

In order not to sink in, the reaction force must be received from the substrate at the moment when the microtubule collides with the substrate. The constraint is g_2. Assuming that the surface of the substrate is z =0, when the microtubules are sunk into the substrate, a binding force is applied to the beads so that the z-direction component of the beads becomes the radius R of the microtubules. The value of y such that the position of the beads in eq (11) satisfies the constraint g_2 can be calculated in eq (15).

$$g_2 = z_i(t + \Delta t) - R = 0$$

$$\gamma_2 = R - z_i'(t + \Delta t) \qquad (15)$$

After correcting the position of the beads so as to satisfy the constraint condition that the line segment connecting the beads does not sink into the wall. When it is determined that the line segment is embedded in the wall, the distance between the position vector at the corner of the wall the position vector of the collision point between the line segment and the corner of the wall becomes 0 in the YZ plane. By applying binding force, the component of apply force is Y direction and Z direction. Each directional component can be obtained by calculating eqs (22) and (23) for the Y direction and Z direction components of the position vector of the collision point. However, since the binding force cannot be applied to the line segment, the binding force is distributed to the beads in consideration of the torque of the line segment.

$$g_3 := y_i(t + \Delta t) - b = 0 \quad (16)$$

$$g_4 := z_i(t + \Delta t) - h = 0 \quad (17)$$

Apply the restraint force by the restraint conditions g_3 and g_4 to the beads sunk into the wall. The position determines before Δt sec which constraint condition is due to the binding force.

$$\gamma_3 = b - y_i'(t + \Delta t) \quad (18)$$

$$\gamma_4 = h - z_i'(t + \Delta t) \quad (19)$$

From the above, g_3 and $g_4$which satisfy the constraint condition in each aspect, can be calculated as follow.

$$g_5 := \bar{r}(t + \Delta t) - b = 0 \quad (20)$$

$$g_6 := \bar{r}(t + \Delta t) - h = 0 \quad (21)$$

when the line segment pushes into the wall, it distributes the binding force to the beads so that the collision point corresponds with the corner of the wall.

$$\gamma_5 = b - \bar{r}(t + \Delta t) \quad (22)$$

$$\gamma_6 = h - r(t + \Delta t) \quad (23)$$

The undetermined multiplier γ, is calculated from this constraint condition. The eq (11) becomes the eq (24),

$$g_1 = \{\bar{r}_{i,j+1}(t) - \bar{r}_{i,j}(t)\}^2 - d^2 = 0 \quad (24)$$

To keep the microtubule movement above the substrate, the position of the beads representing the microtubule were subjected to the following holonomic constraints:

$$g_{track,i} = z_i = 0, \qquad if\ z_i < 0 \qquad (25)$$

The correction was carried out with the following expression:

$$\bar{r}_i(t + \Delta t) = \bar{r}_i{}'(t + \Delta t) + \Delta\bar{r}_i(t + \Delta t) \quad (26)$$

where $\Delta\bar{r}_i(t + \Delta t)$ is the correction term.

$$\Delta\bar{r}_i(t + \Delta t) = \frac{\Delta t}{\zeta}\sum_{k=1}^{n-1}\lambda_{segment,k}\frac{\partial g_{segment,k}}{\partial r_i} + \frac{\Delta t}{\zeta}\lambda_{track,i}\frac{\partial g_{track,i}}{\partial r_i} \quad (27)$$

$\lambda_{segment,k}$ and $\lambda_{track,i}$ are Lagrangian multipliers, which were determined in order for the coordinate at $t + \Delta t$ to satisfy the constraints expressed eqs (24) and (27), respectively. For this, we went through the calculations for the constraints one by one, cyclically, adjusting the coordinates until the constraints were satisfied with a tolerance of 10^{-6}.

2-1.8 IMEX method

In dealing with the eq (3), we used an implicit-explicit (IMEX) method, where the restoring force of microtubule bending was implicitly calculated while other terms were explicitly calculated. In the unconstrained movements were corrected by considering the constraints due to the microtubule segment length and the guiding tracks of microtubules.

2-1.9 Solving equation of motion with constraints

The most fundamental form of the Lagrangian equation of motion is as follow

$$\frac{d}{dt}\left(\partial L/\partial \dot{q}_k\right) - \left(\partial L/\partial q_k\right) = 0 \qquad (28)$$

where the Lagrangian function $L(q, \dot{q})$ is defined in terms of kinesin and potential energies

$$L = K - V \qquad (29)$$

and is considered to be a function of the generalized coordinates q_k and their time derivatives $\dot{q}_k$. If we consider a system of atoms, with Cartesian coordinates r_i and the usual definitions of K and V then eq (28) becomes

$$m_i \ddot{r}_i = f_i \qquad (30)$$

where m_i is the mass of atom i and

$$f_i = \nabla_{r_i} L = -\nabla_{r_i} V \qquad (31)$$

is the force on that atom. These equations also apply to a molecule's center of mass motion, with f_i representing the total force on molecule i; the equations for rotational motion may also be expressed in the form of eq (28) and dealt with in this section.

By solving the equation of motion with constraint, we are using Lagrangian multiplier.

$$m_1 \frac{d^2_{\overline{r}_1}}{dt^2} = \overline{F}_1 \qquad (32)$$

$$m_2 \frac{d^2_{\overline{r}_2}}{dt^2} = \overline{F}_1 = -\overline{F}_2 \qquad (33)$$

with constraints, six coordinates are not independent. We cannot treat systems with constraints as ones with constraints. In general case,

$$g_k(\overline{r}_{i1}, \overline{r}_{i2}, \ldots\ldots\ldots, \overline{r}_{il}) = 0 \qquad k = 1 \sim \text{(N-1)} \quad (34)$$

$$\frac{d}{dt}\left(\frac{\partial}{\partial \dot{\overline{r}}_{i\alpha}}\right) - \frac{\partial L}{\partial \overline{r}_{i\alpha}} = \sum_{k=1}^{N-1} \lambda_k \frac{\partial_g}{\partial \overline{r}_{i\alpha}} \qquad (35)$$

were, λ_k is a Lagrangian multiplier. The general equation is shown in eq (36). The Lagrangian multiplier is the constant (or constants) used in the method of Lagrange multipliers; in the case of one constant, it is represented by the variable. A method of solving an optimization problem subject to one or more constraints.

$$m\ddot{\overline{r}}_{i\alpha} = \overline{F}_{i\alpha} + \sum_{k=1}^{N-1} \lambda_k \frac{\partial_g}{\partial \overline{r}_{i\alpha}} \qquad (36)$$

The $m\ddot{\overline{r}}_{i\alpha}$ is an inertia force, $F_{i\alpha}$ is an external force and $\sum_{k=1}^{N-1} \lambda_k \frac{\partial_g}{\partial \overline{r}_{i\alpha}}$ is a constraint condition.

In our simulations, we calculated the Lagrangian multiplier in the equation of motion as follow.

$$m\ddot{\overline{r}}_i = -\rho\dot{\overline{r}}_i + \overline{F}_{external,i} + \overline{R}_i + \sum_{k=1}^{N-1} \lambda_k \frac{\partial_g}{\partial \overline{r}_i} \qquad (37)$$

When neglect the inertia, the eq (37) will be changed.

$$0 = -\rho\dot{\overline{r}}_i + \overline{F}_{i(external)} + \overline{R}_i + \sum_{k=1}^{N-1} \lambda_k \frac{\partial_g}{\partial \overline{r}_i} \qquad (38)$$

$$\frac{\overline{r}_i(t+\Delta t) - \overline{r}_i(t)}{\Delta t} = \frac{1}{\rho}\overline{F}_{ex} + \frac{1}{\rho}\overline{R}_i + \frac{1}{\rho}\sum_{k=1}^{N-1} \lambda_k \frac{\partial_g}{\partial \overline{r}_i} \qquad (39)$$

$$\overline{r}_i(t+\Delta t) = \overline{r}_i(t) + \frac{\Delta t}{\rho}\overline{F}_{ex} + \frac{1}{\rho}\overline{\omega} + \frac{\Delta t}{\rho}\sum_{k=1}^{N-1} \lambda_k \frac{\partial_g}{\partial \overline{r}_i} \qquad (40)$$

The g_k can be calculated the following equation.

$$g = (\overline{r}_{i+1} - \overline{r}_i)^2 - \ d^2 = 0 \quad (k = 1, \dots., N-1) \quad (41)$$

If $t = t + \Delta t$,

$$g = \left[\left(\overline{r}_{i+1}(t+\Delta t) + \Delta r_{i+1}(t+\Delta t)\right) - \left(\overline{r}_i'(t+\Delta t) + \Delta\overline{r}_i(t+\Delta t)\right)\right]^2 - d^2 = 0 \quad (41\ a)$$

$$\left[\left(\overline{r}_{i+1}'(t+\Delta t) - \overline{r}_i'(t+\Delta t)\right) + (\Delta\overline{r}_{i+1}(t+\Delta t) - \Delta\overline{r}_i(t+\Delta t))\right]^2 - d^2 = 0 \quad (41\ b)$$

$$\left[\left(\overline{r}_{i+1}'(t+\Delta t) - \overline{r}_i'(t+\Delta t)\right) + 2\cdot\frac{\Delta t}{\rho}\lambda_k 2(\overline{r}_{i+1} - \overline{r}_i)\right]^2 - \ d^2 \ = 0 \quad (41\ c)$$

By using algebra formula, $[x+y]^2 = [x^2 + 2xy + y^2]$, the eq (41 c) can calculated as follow

$$16\frac{\Delta t}{\rho^2}(\overline{r}_{i+1} - \overline{r}_i)^2 \cdot \lambda_k^2 + 8\frac{\Delta t}{\rho}\left\{\overline{r}_{i+1}'(t+\Delta t) - \overline{r}_i'(t+\Delta t)\right\}^2$$

$$\cdot\,(\overline{r}_{i+1} - \overline{r}_i)\lambda_k + \left\{\overline{r}_{i+1}'(t+\Delta t) - \overline{r}_i'(t+\Delta t)\right\}^2 - d^2 = 0 \quad (42)$$

$$8\frac{\Delta t}{\rho}\left\{\overline{r}_{i+1}'(t+\Delta t) - \overline{r}_i'(t+\Delta t)\right\}\cdot(\overline{r}_{i+1} - \overline{r}_i)\lambda_k + \left(\overline{r}_{i+1}'(t+\Delta t) - \overline{r}_i'(t+\Delta t)\right)^2 - d^2 = 0 \quad (43)$$

By calculating the eq (3.16), we obtained the Lagrangian multiplierλ_k in eq (44):

$$\lambda_k = \frac{d^2 - \left(\overline{r}_{i+1}'(t+\Delta t) - \overline{r}_i'(t+\Delta t)\right)^2}{8\frac{\Delta t}{\rho}\left\{\overline{r}_{i+1}'(t+\Delta t) - \overline{r}_i'(t+\Delta t)\right\}\cdot(\overline{r}_{i+1} - \overline{r}_i)} \quad (44)$$

2-1.10 SHAKE Method

The position of the beads at every t seconds step can be calculated using eq (2) in section 2-1.2, but the position of the beads must always satisfy the constraint condition. There are two constraints in the simulation used in this study. One of the condition is that the microtubules do not penetrate into the substrate, or the wall and the other is that the distance between the beads is always constant. The calculation of eq (3) alone cannot calculate the position of a bead that always satisfies the constraint condition. By adding these binding forces, the positions of beads that satisfy the constraint conditions can be derived. However, when there are multiple constraints, the SHAKE method is used because the constraint force that satisfies all the constraints cannot be obtained by one calculation. The details of these two conditions are described in section 2.1.9 and 2.1.6.

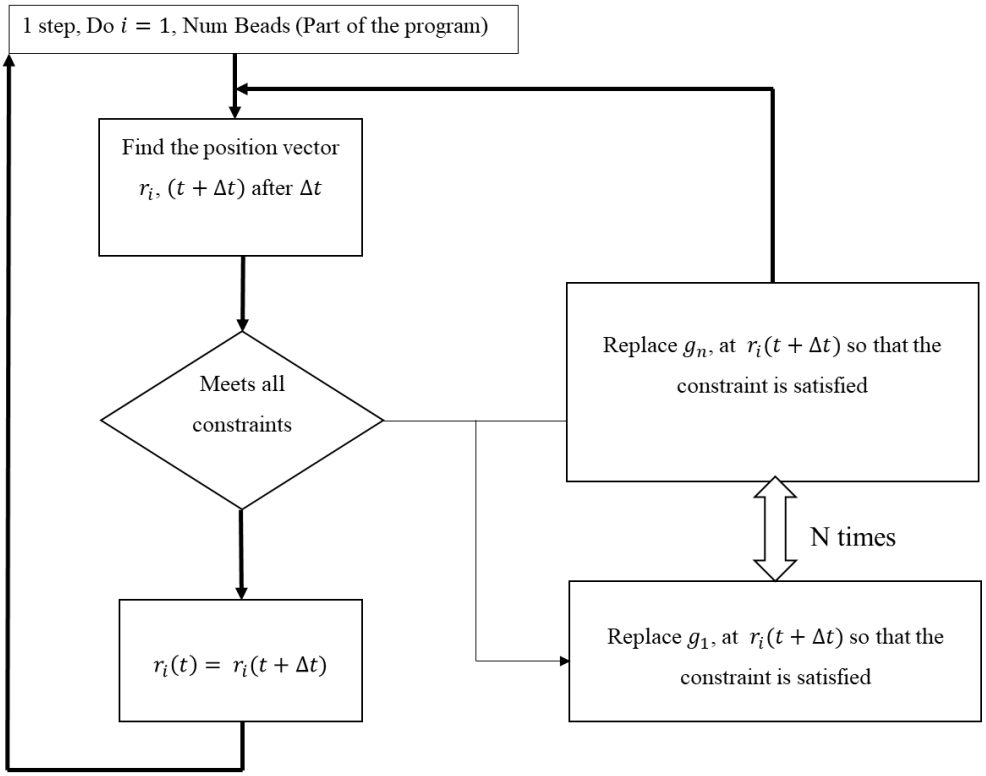

Figure 2-1.7: Algorithm of SHAKE method. Calculates the position of the quotient point after Δt seconds without the promised condition and confirms that all the constraints are satisfied. If not, the bead position is calculated until all constraints are met.

A flow chat of a part of the source code using the SHAKE method as shown in (Figure 2-1.7). First, the position of the beads after Δt seconds when the binding force is not acting is calculated by eq (2). Next, it is confirmed whether the coordinates of the bead satisfy all the constraints conditions. If the constraint condition is not satisfied, the constraint force is calculated, and the position of the bead is corrected. Do the above for all constraints and do not exist this loop until the bead positions meets all the constraints.

2-1.11 Kinesin movement on microtubules

Kinesin motors were randomly distributed over the allowed surface by specifying the positions of the kinesin tails. In this movement, bond dissociation is performed on microtubules. The simulation deals only with kinesin bound to microtubules. Then, the kinesin bound to the microtubule moves on the microtubule toward the positive end in (Fig 2-1.8). Its movement speed depends on the load applied to the kinesin head as shown in (Fig 2-1.4). Details of modeling the movement of kinesin on this microtubule are described below. In addition, kinesin bound to microtubule interacts with each other. Kinesin head bind to microtubules during the capture radius of 20 nm around the microtubule length.

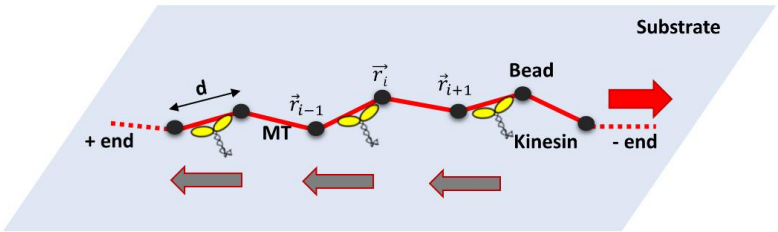

Figure 2-1.8: Kinesin motors bound to the microtubule on the substrate.

2-1.12 Applied external force

External force applied to microtubules by an electric field includes electrophoresis and electroosmotic flow in the previous experiments [25][26]. Since there are actual experiments on the movement of microtubules due to them, the parameters of external force are determined with reference to them. The external force is expressed by applying a force per unit length of

microtubules to each bead. As the external force in (Fig 2-1.9), a uniform force field pointing the x-direction was applied in eq (45):

$$F_{ext} = \begin{pmatrix} f.d \\ 0 \\ 0 \end{pmatrix} \quad (45)$$

where, f is a force density and F_{ext} is an external force.

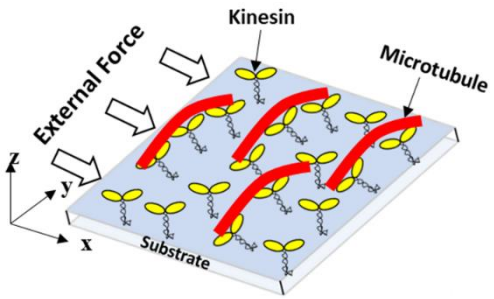

Figure 2-1.9: Microtubule movement on the kinesin motor surface under external applied force. The left arrows represented the dimensional external forces applied on the x-axis.

2-1.13 Persistence Length

In molecular shuttle study, measurement of persistence length is important for prediction of microtubules movement and their performance. We determined the two-persistence length in the following section. These are filament persistence length ($L_{p,filament}$) and path persistence length ($L_{p,path}$). In our simulation, the filament persistence length ($L_{p,filament}$) is a preset parameter.

2-1.14 Path and Filament persistence length

The wiggliness of the filament is relative to bending rigidity is called filament persistence length ($L_{p,filament}$). The filament persistence length ($L_{p,filament}$) of a long object (such as microtubule filament) is a measure of the flexibility of that object in (Fig 2-1.10). Imagine a long cord that is slightly flexible. At short distance scale, the cord will basically be rigid. If we look at the direction the cord is pointing at two points that are very close together, the cord will likely be pointing in the same direction at those two points. That means that the angles of the tangent vectors are highly correlated. If we choose two points on this flexible cord that are very far apart, however, the tangent to the cords at those locations will likely be pointing in different directions as shown in (Fig 2-1.11). That means the angles will be uncorrelated. If we plot out how correlated the tangent angles at two different points are as a function of the distance between the two points, we will get a plot that starts out at 1 (perfect correlation) at a distance zero and drops exponentially as distance increases [27]. The (L_p) is the characteristic length scale of that exponential decay in (Fig 2-1.12). In our simulation, movements of molecular shuttles (MSs) are crucial for the overall device performance. MSs take trajectories with directional fluctuations. The degree of the fluctuation determines satisfied properties of MSs trajectories, which is characterized by the path persistence length ($L_{p,path}$).

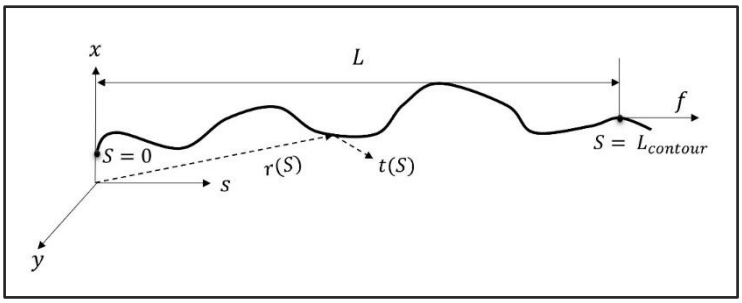

Figure 2-1.10: Schematic diagram of filament persistence length of microtubule

The path persistence length can be calculated with the following formula in general,

$$< \cos(\Delta\theta) > = \exp\left(\frac{S}{2L_p}\right) \qquad (46)$$

where, $\Delta\theta$ is tangle angle between the two beads of the microtubule length, S is a path or contour length and <> denotes averaging over filaments.

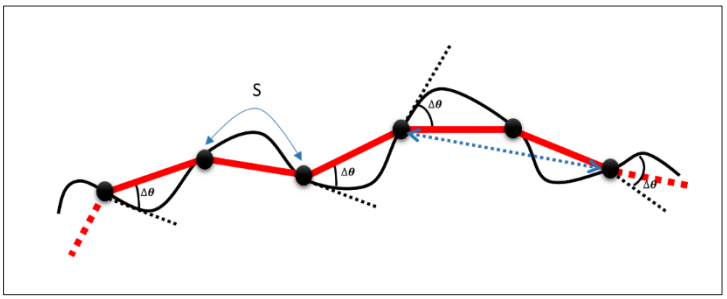

Figure 2-1.11: Schematic diagram of path persistence length of microtubule

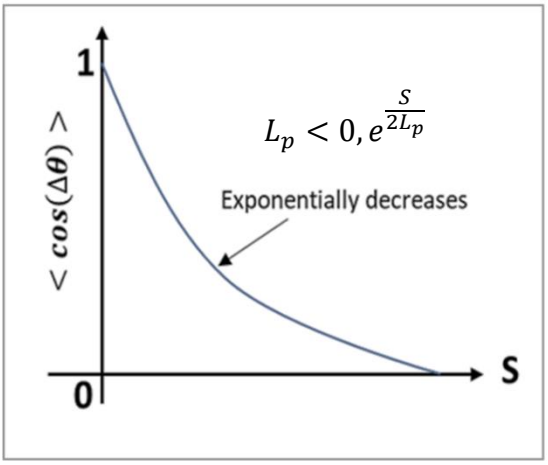

Figure 2-1.12: Schematic diagram of the angle distribution along the arc length (S). The angle is exponentially decreasing along the arc length.

But in our simulation, we calculated the path persistence length from the curvature of the averaged microtubule trajectories under external applied forces. The averaged trajectories were compared with the following eq (47) based on van den Heuvel et al., the elastic theory of bending rods in eq (48):

$$y\,(x) = R_0\, cos^{-1}\left(e^{-\frac{x}{R_0}}\right), \qquad (47)$$

$$R_0 = \frac{3k_B T L_p}{f\langle d\rangle^2}, \qquad (48)$$

where k_B is Boltzmann constant, T is absolute temperature, f is external applied force density, $\langle d\rangle$ is the average length of bending part of MTs. L_p is either path or filament persistence lengths as we will specify later. R_0 is radii of the curvature of microtubule. The detail calculation of these eqs (47) and (48) will be described in Appendix. By using this formula, we investigated the analysis of the microtubule path persistence length ($L_{p,path}$) in Chapter 3.

2-2 Materials and Experimental procedure

2-2.1 Research Purpose

In a previous study, gold nanowires were created by attaching gold colloid to microtubules, and the microtubules were successfully made electrically conductive. The development of technology for creating nanoscale microtubules and is considered by combining this with self-assembly of microtubules by molecular motors. The development of manufacturing technology for micro integrated scale materials in electronic devices is expected to enhance greatly from the realization of this technology. This work was carried out as an approach to the development of self-organizing nanocircuits by subdividing the path to their technological development. (1) investigate microtubule behavior; (2) create gold nanowires (different way than earlier studies).

2-2.2 Experimental approach for in-vitro motility assay

In a previous study, we used in-vitro motility assay procedures such as gold nanoparticle production by photochemical reduction method to efficiently bind gold nanoparticles to microtubules for conductivity. In order to carry out this study in a new approach, we examined how gold nanoparticles bind to the assembly of biotin-streptavidin-functionalized microtubules and how they move on a protein kinesin-coated surface. Biotin labeled tubulin [29] polymerizes to form microtubules in this assay. In addition, we utilized Alexa 488 Streptavidin AuNP gold nanoparticles [30] to perform a motility assay. In the following sections, we'll go through the procedure in more detail.

2-2.3 Preparation of stock solutions

Experiment 1 (Microtubule's polymerization)

We started by preparing the microtubule (MT) assembly for in-vitro motility assay experiments. Microtubules that have been polymerized in the following method are commonly used in (Table 3).

Table 3: Preparation of the stock solution of microtubule

Biotinylated tubulin (20 µg/µl)	(Source: Porcine Brain)
Buffer (3x)	3 µl
BRB80 (1x)	6 µl

In the block incubator, we initially set the temperature to 37°C. To freshly thawed biotinylated tubulin 20 µg/µl on ice, took out 7 µl of biotinylated tubulin. And made the stock solution with 3 µl of buffer (3x) and 6 µl of BRB80 (1x), totaling 9 µl. We combined these solutions and heated them to 37°C for 40 minutes. After standing between labeled tubes, 0.1 µl of 1 mM taxol is added to stabilize microtubules and stir by passing the microtubules through a yellow-tip (20-100 µl) pipet several times. Finally, the microtubules formed properly with this polymerized biotinylated tubulin. For motility experiments, they sustain 2 to 3 days at room temperature. The growing microtubules nodes were damaged if the left microtubule stock solutions were stored at room temperature for a long time. As a result, after using the microtubule stock solution, we must store it at a temperature of -80 °C. To achieve so, liquid nitrogen gas must be used to freeze the left microtubule stock solutions can be quickly frozen with stable liquid nitrogen and can be stored at -80 °C. We keep the finished product in the -80 °C refrigerator.

Experiment 2 (Basic Solution)

We prepared the essential solutions for in-vitro motility assay experiments. The following is the detailed protocol for this experiment. The BRB 80 Buffer solution was first prepared for the basic solution process.

(1) Making Assay Buffer solution:

BRB 80 Buffer:

80 mM 1, 4-piperazinediethanesulfonic acid (Pipes), free acid, 1mM MgCl2, 1 mM ethylene glycol bis (β-aminoethyl ether) N, N'-tetra acetic acid (EGTA), pH 6.85, with KOH, is filtered (0.2 µm), and 10 ml aliquots are stored at -20 °C [9].

Diluted microtubule solution for the motility assay:

We used BRB 80 (10x) of 10 µl in addition to 1 M $Mgcl_2$ 0.9 µl. Also, combined the 0.1 M GTP 3 µl and the 0.1 M GTP 3 µl. After that, 15 µl of 15 percent DMSO and 71.1 µl of milli Q (purified water). In addition, we estimated the final concentration by performing the BRB 80 (1x) procedure, which involved extracting 2 µl of BRB80 and diluting it with 18 µl of milli Q. (purified water). Finally, the 20 µl BRB80 (1x) buffer solution is ready to be used in the in-vitro motility assay process in (Table 4).

(2) Making basic solution

Table 4: Preparation of the basic solution for in-vitro motility assay

Solution 1	Solution 2	Solution 3
1 ml Assay Buffer	1 ml Assay Buffer	1 ml Assay Buffer
5 µl 2-Mercaptoethanol	5 µl 2-Mercaptoethanol	5 µl 2-Mercaptoethanol
50 µl Casein	50 µl Casein	50 µl Casein
	2 µl Taxol (10 mM)	2 µl Taxol (10 mM)
		10 µl Glucose (G)
		10 µl Catalase (C)
		10 µl Glucose Oxidase (O)
		10 µl Adenosine Triphosphate (ATP)

Glucose, catalase, and glucose oxidase (GCO) are added to solution 3 to prevent the fluorescent dye from fading due to photoexcitation. Fluorescence fading is mostly caused by active oxygen generated by photoexcitation, therefore oxygen in the solution is removed during the next catalytic reaction in this system [31].

Experiment 3 (Biotin labeled Tubulin + Alexa 488 Streptavidin AuNP [10nm])

Biotin labeled tubulin (Porcine Brain) can be bound to Alexa 488 streptavidin beads and needed to create paclitaxel stabilized biotinylated microtubules that act as a surface substrate for microtubule binding. In this part, we used the biotin labeled tubulin with the Alexa 488 Streptavidin AuNP (10nm) stock solution. A biotin-binding protein (streptavidin) is covalently bonded to a fluorescent label (Alexa Fluor® dye) in Alexa Fluor® 488 streptavidin [30]. Streptavidin has a high affinity for biotin, thus it's common to use a streptavidin conjugate with a biotin conjugation to detect a wide range of proteins. Streptavidin binds 4 moles of biotin per mole of protein. Streptavidin is a biotin-binding protein found in the bacteria Streptomyces avidin's culture broth. A fluorescently labeled streptavidin can detect a biotinylated primary antibody attached to a protein target. We prepared a stock solution of biotinylated microtubule and gold nanoparticle, AuNP 10 nm, in our experiment. To the 100 µl of motility solution 2, add 2 µl of Alexa 488 Streptavidin AuNP (10 nm). This solution was once again used in the in vitro motility assay experiments.

2-2.4 Preparation of Motility solutions

1. Make a kinesin solution

We prepared the kinesin solution to use in in-vitro motility assay experiments.

Kinesin solution (50x solution):

The stock kinesin solution used in these experiments is made accessible under a user agreement [32]. In the in-vitro motility assay

experiments, we used this kinesin stock solution. The temperature of this kinesin stock solution was kept at -80 °C. We managed to bring this kinesin stock solution to room temperature (R.T), which was 37°C. We determined the desired kinesin concentration or surface density. Estimate the concentration approximatively 50x, take 1 µl of kinesin solution and mix it with 49 µl of motility solution 1, as described (in section 2-2.3). After estimating the concentration of kinesin solution, this concentration is good enough to use in typical assays. If the kinesin concentration needs to be diluted more than ten times, dilute it in a solution of solution 1 containing 0.5 µl casein. Optimal Kinesin concentration is low in the first case of Kapila. To get a final concentration, change the kinesin to 10-50 µg/ ml in solution 1 or the quality of the refined kinesin, etc. Change accordingly etc. to reach a final concentration. Change as needed to find a good conditions. Add 3 l of kinesin stock solution to the 147 l of solution 1 used in the in-vitro motility assay process to produce a final concentration.

2. Make a microtubule solution

The microtubule solution was prepared to be used in in-vitro motility assay experiments.

Microtubule solution (50x solution):

Dissolve 0.2-0.5 µl of polymerized biotinylated microtubules synthesized in 200 µl of solution 2 to the motility solution (in section 2-2.3). Depends upon the concentration of fluorescent microtubules produced, dilute suitably. It's important to note that this motility solution could last up to 3 hours at R.T. After that duration, the taxol in solution 2 easily decomposed the nodes of polymerized microtubule filaments.

2-2.5 Assembling the flow cells

The general procedure for assembling the flow chambers is described in Figure (2-2.1). Double-sided tape is applied to both sides of the side glass, and a flow damper is created by creating a small space between the slide glass and the cover glass [33], as represented in the diagram. Apart from double-sided Scotch tape to confine the flow channels, we also used Parafilm or Nescofilm [34] as an alternative. The flow chamber is put together as follows: Cut the Para-/Nescofilm into stripes using a razorblade. Place the prepared para-/Nescofilm stripes on top of a 22 mm coverslip and cut off all the parts of the stripes that protrude over the coverslip's edges using a razor blade. Experiments were performed in 1.5 to 2 mm-wide flow cells formed by two glass coverslips (Corning 22 × 22 mm^2 coverslips [8] face down and 18 × 18 mm^2 [9]) in the stripes' center. This flow cell chamber had a thickness of 0.1 mm. After that, the flow chambers are ready to flow the in-vitro motility assay and gold nanoparticle solutions into a flow cell.

(A) **(B)**

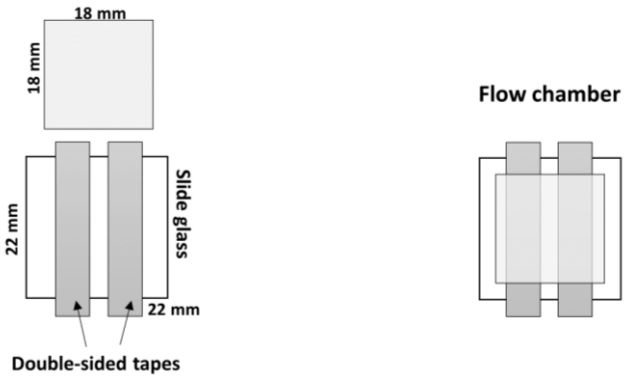

Figure 2-2.1: The flow cell of the chamber is featured in this diagram. (A) The double-sided Scotch tape used to confine the flow channels is shown in

the figures. (B) The down slide glass is (20 x 20 mm), the top slide glass is (18 x 18 mm), and parafilm is placed between the sandwich glasses throughout the flow chamber.

2-2.6 Flowing the motility solutions into the flow cell

For motility assays, section 2-2.4 (2) utilized biotinylated polymerized microtubules with Alexa 488 Streptavidin AuNP (10 nm), whereas section 2-2.4 (1) used Kinesin motor proteins to film a flow cell using standard procedures by using a fluorescent microscope. The process of the flowing motility assay with gold nanoparticles described as follows.

(1) Added 50 µl of the kinesin solution 1 to the flow chamber. Let at room temperature for 2 minutes. Tilt the flow chamber and added 100µl of solution 1 from one end and rinse the unbound kinesin.

(2) 50 µl of microtubule solution 2 was added and made to grow for 2 minutes. 100 µl of solution 3 was added, followed by a rinse to remove any unbound microtubules. To stabilize the motility solution, 50 µl of solution 3 were added. Note that we were just concerned in to see if the gold nanoparticles effectively bind to the microtubules at this moment. As a result, we skipped adding ATP to solution 3.

(3) We replaced the chamber with 50 l of Alexa 488 Streptavidin AuNP to introduce gold nanoparticles to the flow cell (10 nm). After that, wait 5 min at R.T before washing with 100 µl of solution 2. In this experiment, we observed various incubation times as (from 2 min to 15 min) to attach the gold nanoparticles with microtubule. When the incubation durations were too long, the AuNP got significantly aggregated, and the prevention of microtubule length also became short. In this technique, 5 minutes of incubation time was the optimal time to perform.

(4) Finally, add 50 µl of solution 3 to complete the process. Finally, the gold nanoparticle glowed intensely on the microtubules.

(5) After these operations were completed, the flow cell chambers were examined using florescence microscopy. These are represented in the diagram below (Fig 2-2.2)

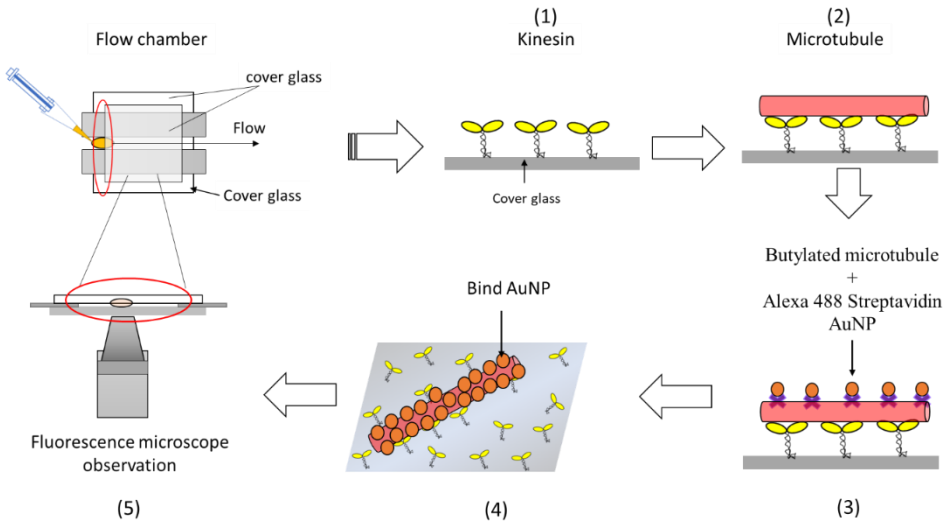

Figure 2-2.2: Schematic diagram of the process of motility solutions in the flow cell chamber as observed by a fluorescent microscope using Alexa 488 Streptavidin AuNP (10nm).

2-2.7 Imaging a flow cell

In our experiments, measurements were recorded using an (IX-71, Olympus) fluorescent microscope [35] with a CMOS camera (CS505MU Kiralux 5.0 MP Monochrome CMOS) [36]. It's important to note that the filter-set allows you to see microtubules. We used a fluorescent microscope

with a 100x magnification and an oil-immersed objective lens. We used a microscope with a 100x numerical aperture objective lens to produce photons with a wavelength of 610 nm using a green light shutter with a wavelength of ≈ 535 nm. Apply a drop of immersion oil to the objective first. After that, place the flow cell on the microscope platform and lift the objective until the oil on the objective contacts the flow cell. In this experiment, we used the X- cite XLED1 light source [37]. To prevent all X-LED1 light from escaping, I used the microscope's cover. After that turn on the LED and focus on the lower surface of the flow cell.

At a wavelength of ≈ 550 nm, fluorescently labeled microtubules are activated. Using a fluorescent microscope and green light, we investigated whether the kinesin-coated microtubules bind to AuNP by naked eye. It should be noted that LED illumination is harmful to the naked eye and can result in permanent damage. As a result, we used an opaque lid to fully conceal all lit area. We also changed the apparatus from an eye scan to a camera scan. In-vitro assay studies were used to check the microtubule behaviors again, and the photos or videos of interest were recorded. For a LED light source, the laser power is typically 50 msec to 100 msec exposure duration. As long as the flow cell is motile, images can be recorded indefinitely. The microtubules break down quickly and the length of the microtubules shortens as the laser light exposure duration is extended. To avoid this, we made sure that the light shutter was closed when we snapped the photo or camera.

Au nanoparticles (AuNP) with diameters ranging from 10 nm were examined with a fluorescent microscope and observed under a dark-field microscope with a numerical aperture condenser. All of the experiments were carried out at room temperature. After we completed all of our observations

with fluorescence and dark field microscopy, we prepared the samples for scanning electron microscopy (SEM) that will explained in the following sections.

2-2.8 Preparing samples

Washing process

After observing biotinylated microtubules containing AuNP particles in an in-vitro motility assay under a fluorescence microscope, we carefully removed the flow cells sandwich coverslips and separated these two coverslips with a tweezer. When removing the flow cells sandwich coverslips, make sure the solution's surface side is facing up. Following that, all coverslips were rinsed twice with ethanol and three times with milli Q water (pure water). Carefully these coverslips gently dip up and down several times. And then dry them for two days in a room temperature of 24-27 °C.

Drying process

Following the washing process, air dried the cleaned coverslips for two days at a room temperature of 22-25 °C. When the coverslips are completely dry with air, store them at room temperature until used. In addition, the dried samples were treated for 1 hour in a vacuum chamber to remove air bubbles. These would absolutely dry the samples.

Prepare the samples for (SEM)

Following the drying of the coverslips, a diamond cutting pen was used to cut approximately 18 mm^2 of dry MT/AuNP samples for SEM examinations. Cut incredibly tiny samples from the slips (approximately 1.5 cm x 1.5 cm) and stick them to the sample stages with conductive carbon tape. Finally, these

samples were completed on the sample stage and left to settle before being examined under the SEM.

2-2.9 SEM observations

Scanning electron microscopes used the scattered electrons from the sample's surface to produce an image. An electron gun is utilized as a light source in the transmission electron microscope, and electromagnetic lenses are used to focus the electron beam on the surface. Scattered electrons are detected while the beam is scanned [38] . For the investigation of the micro and nano structure of sample, SEM observations were made using Hitachi S4800 [39]. To enable clear observation, a 2-10 kV SEM acceleration voltage and a 10-mA current were used. Low to high magnifications, i.e., 5x and 10x, were used to examine samples. Microtubules and AuNP samples were also observed on SEM at the same time. However, in nanoscale observation, it was difficult to see the clear microtubules. Before to SEM observation, these materials were treated with osmium. The osmium coating conducted for a total of 20 seconds. [40]. The osmium coating makes samples conductive, allowing charges and heat to be quickly transferred away from the sample, allowing for clear observations. Researchers were able to see nanofeatures that would otherwise be imperceptible to the naked eye thanks to SEM observations.

Chapter 3 Results and Discussion

3-1 Simulation

3-1.1 Microtubule trajectories under external force field

Microtubule (MT) motions were modelled under lateral forces. The movement of microtubules was monitored using different external force densities and snapshots obtained at different time intervals. As indicated in the figure, these photos were superimposed (Fig 3.1). Initially moving upward, the microtubule's path was gradually moved downstream of the applied force density. Increasing strength of the force density depending on surface motor densities was done as follow.

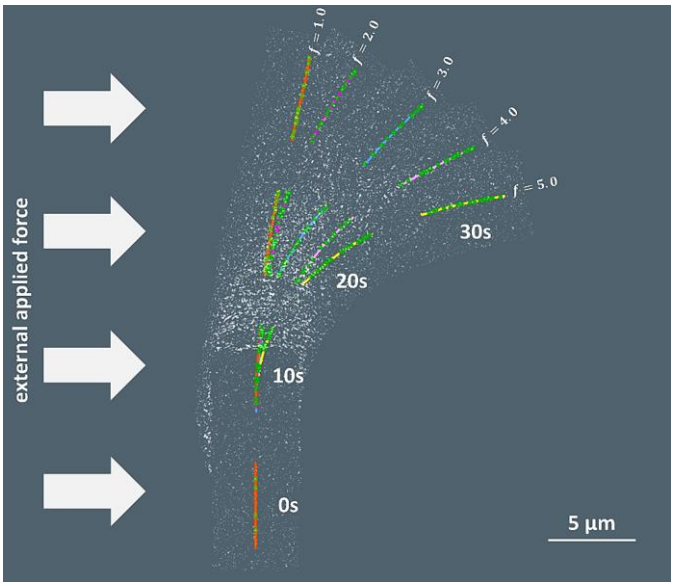

Figure 3.1: A series of snapshots of a microtubule gliding over kinesin under a uniform external force field. The density of kinesin motors was 30 µm-2. The various applied force densities were used in this case. The red line represents the external force $f = 1.0\,pN/\mu m$; the purple one shows $f = 2.0\,pN/\mu m$; the blue line represents $f = 3.0\,pN/\mu m$; the pink line shows

$f = 4.0\ pN/\mu m$ and the yellow line represents $f = 5.0\ pN/\mu m$, respectively. The white dots represent the kinesin motors, and the green dots shows the kinesin binding to the microtubule. Scale bar, 5 μm.

In our simulation, microtubules followed the paths of their leading tip. In other words, smooth movement of microtubules was observed. We concentrated on the path without detaching motions in this investigation. In section 3.1.1, we will talk about how the microtubule path moves smoothly. To better understand how kinesin motors move microtubules under external forces, we first investigated at the appropriate bond length of microtubules at each time step, dt. We simulated individual microtubules with different bond lengths to identify a specific time step dt for microtubule movement. Similarly, we simulated individual microtubules with varied time steps dt to achieve a certain bound length of microtubules. In the simulation, fifty unique microtubule paths were done. From this, we calculated the averaged microtubule trajectories with different microtubule bond lengths such as 0.25 μm, 0.5 μm, and 1.0 μm, respectively in (Fig 3.2 to Fig 3.4). Among them, we investigated microtubule movement with time increments of $dt = 0.5 \times 10^{-6}$ and $dt = 1.0 \times 10^{-6}$ for each bound length in (Fig 3.5). We discovered that the microtubule paths overlapped when they reach certain time steps. In our simulation, we used the bond length of microtubule 0.25 μm with a specific time step of $dt = 0.5 \times 10^{-6}$ based on the results of the investigation.

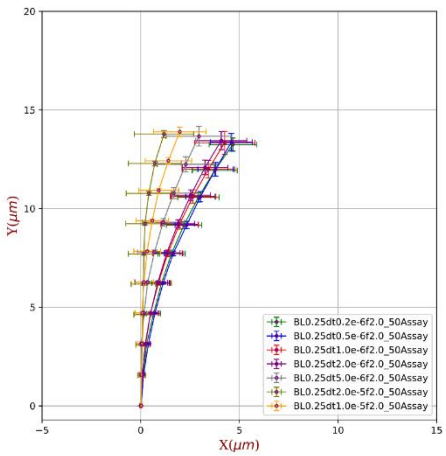

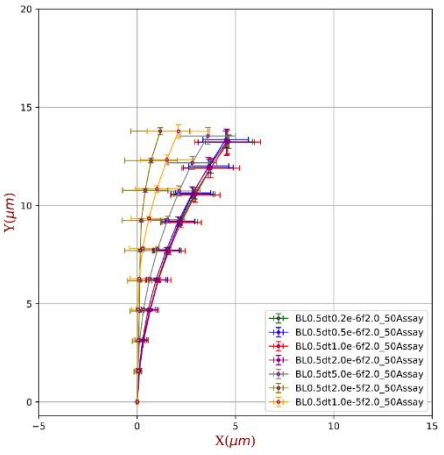

Figure 3.2: The averaged microtubule movement trajectories for different time steps dt with a bond length of 0.25 μm. Figure 3.3: The averaged microtubule movement trajectories for different time steps dt with a bond length of 0.5 μm.

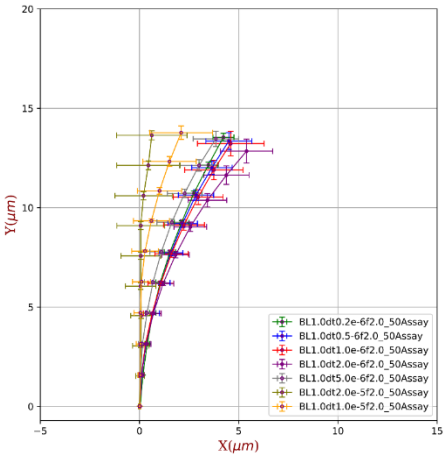

Figure 3.4: The averaged microtubule movement trajectories for different time steps dt with a bond length of 1.0 μm.

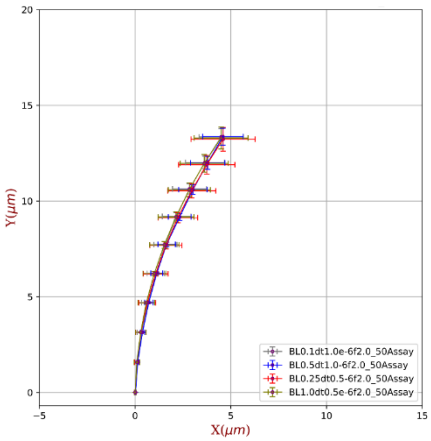

Figure 3.5: The averaged trajectories of the microtubule movement with different bond length of 1.0, 0.5, 0.25 and 1.0 μm for each time step at $dt = 1.0 \times 10^{-6}$ and $dt = 0.5 \times 10^{-6}$, respectively.

3.1.1 Microtubule smooth movement

We investigated the paths of microtubule trajectories under various external forces in our simulation. The majority of microtubule pathways follow a smooth direction with a smooth curve. To study the path persistence length of microtubule tips from individual microtubule trajectories as well as from an average over simulated microtubule trajectories, we followed the experiments of van den Heuvel et al., [25] and compared the curvature of simulated trajectories under perpendicular applied forces with their experimental ones. In our simulation, we investigated the paths of the microtubule trajectories under different fields at various applied force densities. For quantitative analysis, 60^{th} microtubule trajectories under external forces were simulated. In this section, we show each collection of averaged microtubule paths under the various applied force fields for the contradistinctive motor densities as indicated in (Fig 3.6 and 3.7).

(A) **(B)**

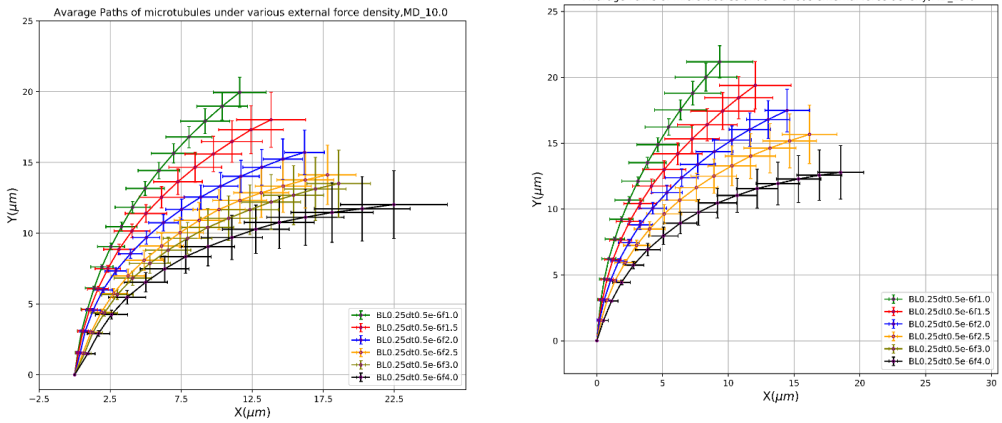

Figure 3.6: The averaged paths of the microtubules under various external forces. with the same surface motor density at 10 μm-2 and 15 μm-2. (A) Paths of microtubules with the surface motor density of 10 μm-2. (B) Paths of microtubules with the surface motor density of 15 μm-2. These all trajectories (colorful trajectories) were representing the microtubule smoothly movement under the various applied forces, $f = 1.0, 1.5, 2.0, 2.5, 3.0, 4.0\ pN/\mu m$, respectively. These are with lower motor densities.

(C) **(D)**

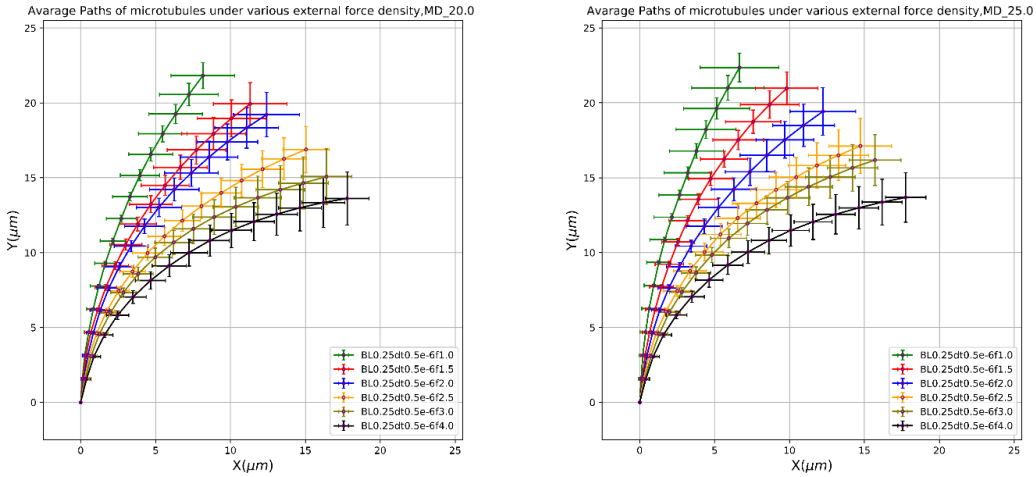

Figure 3.7: The paths of the microtubules under external forces with the surface motor densities at 20 µm-2 and 25 µm-2.

Individual microtubule trajectories moved upward from the origin in these various trajectories, with applied force densities was $f = 1.0\ pN/\mu m,\ 2.0\ pN/\mu m,\ 3.0\ pN/\mu m,\ 4.0\ pN/\mu m$ and $5.0\ pN/\mu m$, respectively. When the applied force density is increased, the bending of microtubule paths becomes more obvious. We discovered that the trajectories of microtubule movement were more detached in the lower surface density kinesin motors 10 μm^{-2} and 20 μm^{-2} when the applied force density was 4.0 pN/µm and 5.0 pN/µm, respectively, based on the above findings. We selected the only path of microtubule trajectories that moved smoothly for this analysis. Furthermore, we looked at more microtubule movement trajectories with a motor density of 30 μm^{-2} in (Fig 3.8), as compared to the higher motor densities of 40 μm^{-2} and 50 μm^{-2} in (Fig 3.9 and 3.10).

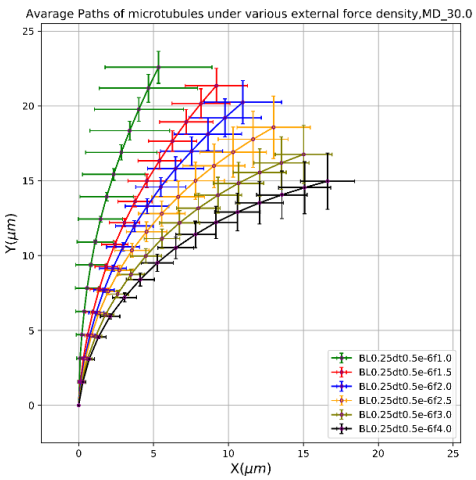

Figure 3.8: The paths of the microtubules under external forces with the same surface motor density at 30 µm-2. These all trajectories were representing the microtubule smoothly movement. The black trajectories show the averaged microtubules trajectories at higher force density $f = 4.0\ pN/\mu m$.

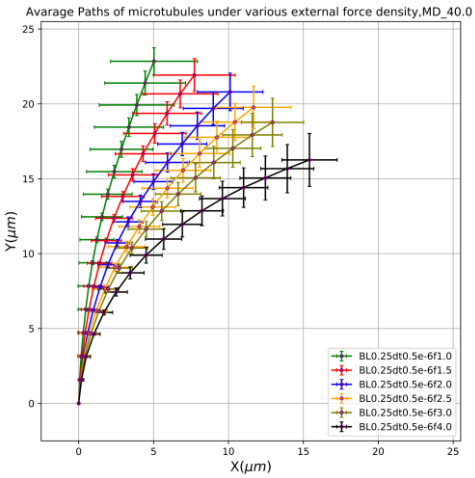

Figure 3.9: The paths of the microtubules under external forces with the same surface motor density at 40 µm-2. These all trajectories were representing the microtubule smoothly movement with the high motor density. The black trajectories show the 30th microtubules trajectories at high force density $f = 4.0\ pN/\mu m$.

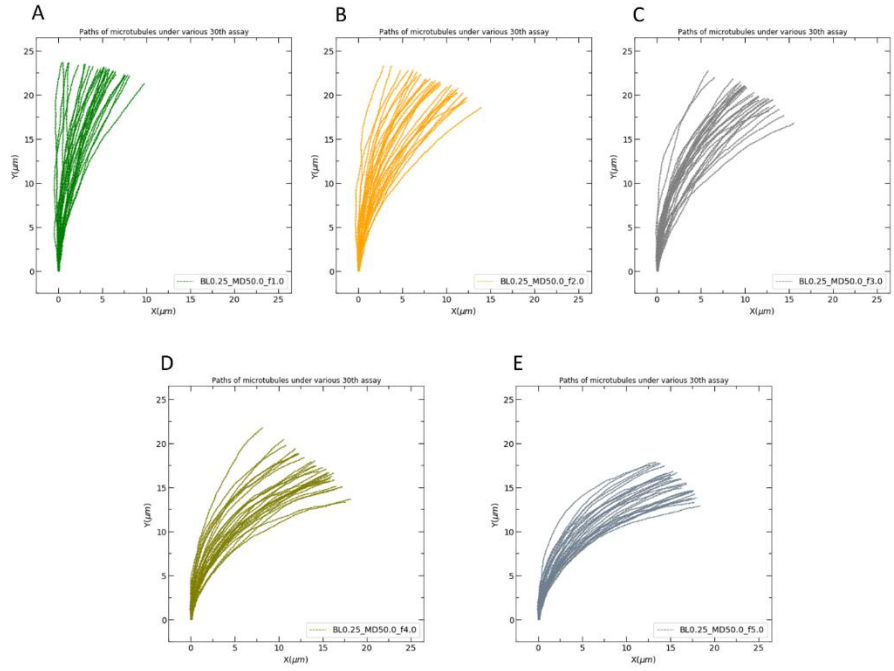

Figure 3.10: The paths of the microtubules under external forces with the same surface motor density at 50 µm-2. (A) The green trajectories represent 30th microtubules smooth paths under lower external force density at $f = 1.0\,pN/\mu m$. (B) The orange trajectories show the 30th microtubules trajectories at $f = 2.0\,pN/\mu m$. (C) The grey trajectories represent the 30th microtubules paths at $f = 3.0\,pN/\mu m$. These all trajectories were representing the microtubule smoothly movement under the lower applied force. (D) The olive color trajectories show the 30th microtubules trajectories at $f = 4.0\,pN/\mu m$. (E) The orange trajectories show the 30th microtubules trajectories at higher force density $f = 5.0\,pN/\mu m$.

As a result of the above study, we realized that increasing the strength of the force density led to a more profound bias of the pathways. Microtubules demonstrated infrequent dissociations from the kinesin coated surface below a certain force density depending on surface motor density (for example, 3.0 pN/µm for 30 μm^{-2}), as evidenced by discontinuities along trajectories in the force density (Fig 3.11).

Microtubules followed the paths of their leading tips below the force densities with occasional dissociation. In our study, we only focused on pathways that were free of such dissociations on a regular basis. To interpret more clearly, we program a selection of microtubule paths under two distinct fields at a low force density $f = 1.0\, pN/\mu m$ and a high force density at $f = 3.0\, pN/\mu m$. Microtubule trajectories showed some variation, even with the same applied force density, due to thermal fluctuations (Fig 3.12). When the applied force density is increased, the curvature of microtubule trajectories becomes more pronounced. The 30th microtubule trajectories were averaged to reduce differences among microtubules for proceeding on to quantitative analysis.

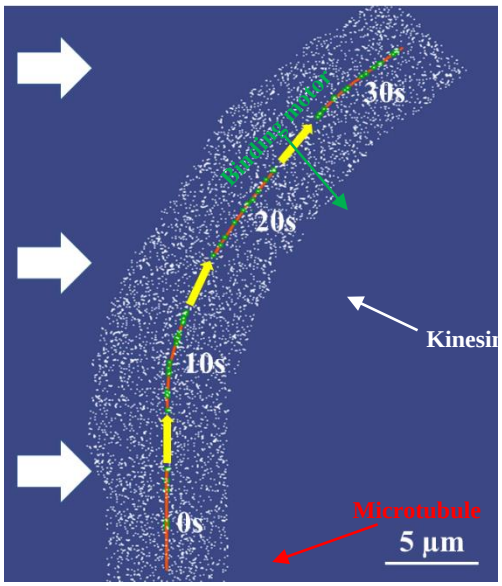

Figure 3.11: A snapshots of a trajectory of microtubule gliding over kinesin under a uniform external force filed. The red lines represent the microtubule;

white dots, kinesin; green dots, kinesin binding to the microtubule. The kinesin motor density was 30 µm-2. Scale bar, 5 µm.

(A) **(B)**

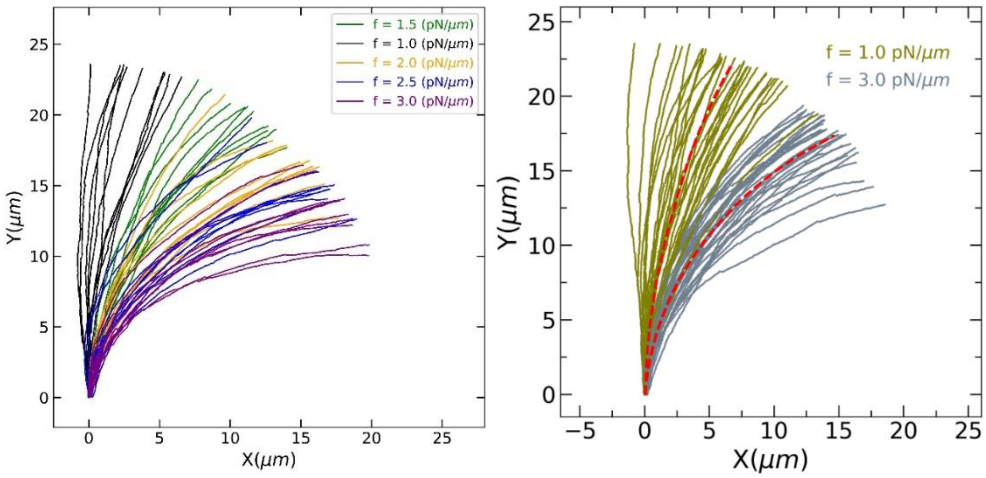

Figure 3.12: Paths of microtubules.
(A) Paths of microtubule with various external force density. (B) Paths of microtubules under two different external force densities. The grey and green curves show the 30 representative trajectories of individual microtubules under $f = 1.0\,pN/\mu m$ and at $f = 3.0\,pN/\mu m$, respectively. The dashed red curves show averages of 30 simulated individual trajectories under two applied force densities.

3.2 Calculation of the radius of curvature

To measure the curvature of the microtubules under external forces, we first calculated the average path of microtubule to obtain appropriated value, and then calculated the radius of the curvature of microtubule. We compared averaged simulated paths with the equation obtained by van den Heuvel at al., based on the elastic theory of bending rods [28] as explained in Chapter 2 section 2.4, to determine the path persistence length from the simulation path.

$$y\,(x) = R_0\, cos^{-1}\left(e^{-\frac{x}{R_0}}\right), \qquad (49)$$

$$R_0 = \frac{3k_BTL_p}{f\langle d\rangle^2}, \qquad (50)$$

where k_B is Boltzmann constant, T is absolute temperature, f is external force density, $\langle d\rangle$ is the average length of bending part of MTs. Perhaps we will see later, L_p can be either path or filament persistence lengths. The eq (49) in the averaged simulated path was well fitted (Fig 3.13).

Depending on the motor density and applied force density, the radius of curvature of microtubules can change. Microtubule curvature radii can change depending on the motor density and applied force density. However, the square residual variations of the radius of curvature remain relatively constant ($R^2 = \sim 0.98$). The statistical analysis of each radius of curvature of microtubule and their residual values were shown in (Table 5 to Table 9).

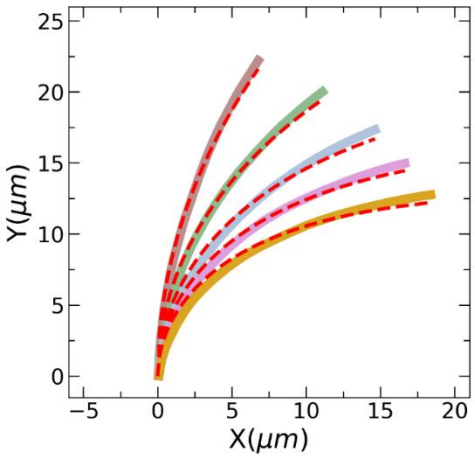

Figure 3.13: The curvature radii of the averaged path. The graphs show the average of individual simulated trajectories under various external forces of $f = 1.0$, 2.0, 3.0, 4.0 and 5.0 $pN/\mu m$, respectively. he non-linear fit to the averaged microtubule trajectories of each force density is indicated by the overlap red curve. The density of kinesin motors in this area was 30 µm-2.

Table 5: The radii of the curvature of microtubule along the kinesin motor density 10 µm-2.

Motor Density ($\boldsymbol{\sigma}$)	External Applied Force ($\boldsymbol{f}$)	Radius of curvature ($\boldsymbol{R_0}$)	Square Residual ($\boldsymbol{R^2}$)	Total Number of MT Trajectories
10 µm^{-2}	1.0 $pN/\mu m$	19.24189	0.9742	29
	2.0 $pN/\mu m$	11.64262	0.9769	25
	3.0 $pN/\mu m$	8.81317	0.9715	21
	4.0 $pN/\mu m$	-	-	Detached
	5.0 $pN/\mu m$	-	-	Detached

Table 6: The radii of the curvature of microtubule along the kinesin motor density 20 µm-2.

Motor Density ($\boldsymbol{\sigma}$)	External Applied Force ($\boldsymbol{f}$)	Radius of curvature ($\boldsymbol{R_0}$)	Square Residual ($\boldsymbol{R^2}$)	Total Number of MT Trajectories
20 µm^{-2}	1.0 $pN/\mu m$	28.00709	0.9867	30
	2.0 $pN/\mu m$	16.92060	0.9876	30
	3.0 $pN/\mu m$	11.07602	0.9864	30
	4.0 $pN/\mu m$	8.26719	0.9723	30
	5.0 $pN/\mu m$	7.22917	0.9376	28

Table 7: The radii of the curvature of microtubule along the kinesin motor density 30 μm-2.

Motor Density ($\boldsymbol{\sigma}$)	External Applied Force ($\boldsymbol{f}$)	Radius of curvature ($\boldsymbol{R_0}$)	Square Residual ($\boldsymbol{R^2}$)	Total Number of MT Trajectories
30 μm^{-2}	1.0 $pN/\mu m$	48.32090	0.9962	30
	2.0 $pN/\mu m$	20.96650	0.9866	30
	3.0 $pN/\mu m$	13.12083	0.9864	30
	4.0 $pN/\mu m$	10.71723	0.9862	29
	5.0 $pN/\mu m$	8.68287	0.9842	28

Table 8: The radii of the curvature of microtubule along the kinesin motor density 40 μm-2.

Motor Density ($\boldsymbol{\sigma}$)	External Applied Force ($\boldsymbol{f}$)	Radius of curvature ($\boldsymbol{R_0}$)	Square Residual ($\boldsymbol{R^2}$)	Total Number of MT Trajectories
40 μm^{-2}	1.0 $pN/\mu m$	51.00226	0.9935	30
	2.0 $pN/\mu m$	24.38536	0.9948	30
	3.0 $pN/\mu m$	16.70673	0.9959	30
	4.0 $pN/\mu m$	12.52326	0.9954	30
	5.0 $pN/\mu m$	10.41732	0.9880	30

Table 9: The radii of the curvature of microtubule along the kinesin motor density 50 µm-2.

Motor Density ($\boldsymbol{\sigma}$)	External Applied Force ($\boldsymbol{f}$)	Radius of curvature ($\boldsymbol{R_0}$)	Square Residual ($\boldsymbol{R^2}$)	Total Number of MT Trajectories
50 µm^{-2}	1.0 $pN/\mu m$	51.33457	0.9945	30
	2.0 $pN/\mu m$	27.81228	0.9927	30
	3.0 $pN/\mu m$	21.16993	0.9954	30
	4.0 $pN/\mu m$	13.92701	0.9942	30
	5.0 $pN/\mu m$	11.61159	0.989	30

3.3 Depending on the applied force density

In this section, we looked at how applied external force affects the radius of curvature. We checked over the radius of curvature R_0, for various motor densities by considering the least-square fit model ($y = ax + b$), where a is the slope and b is an intercept for this line with applied force density. We determined R_0 with the various motor densities fitted within the error (Fig 3.14 A to E).

(A)

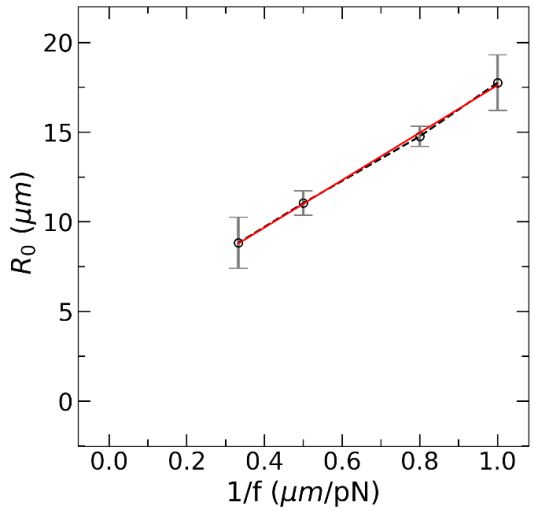
20
15
10
5
0
R_0 (μm)
0.0
0.2
0.4
0.6
0.8
1.0
1/f (μm/pN)

(B)

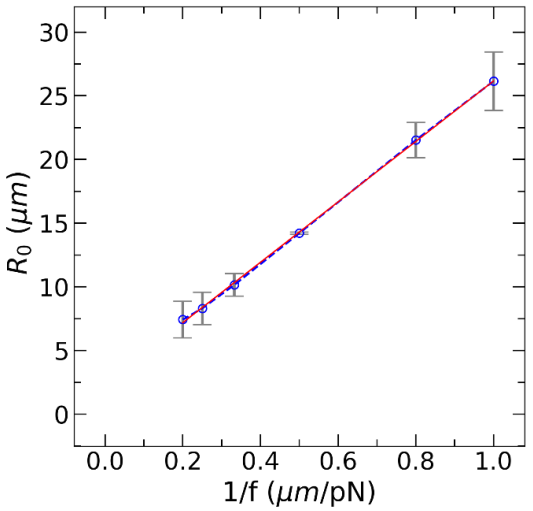
30
25
20
15
10
5
0
R_0 (μm)
0.0
0.2
0.4
0.6
0.8
1.0
1/f (μm/pN)

(C)

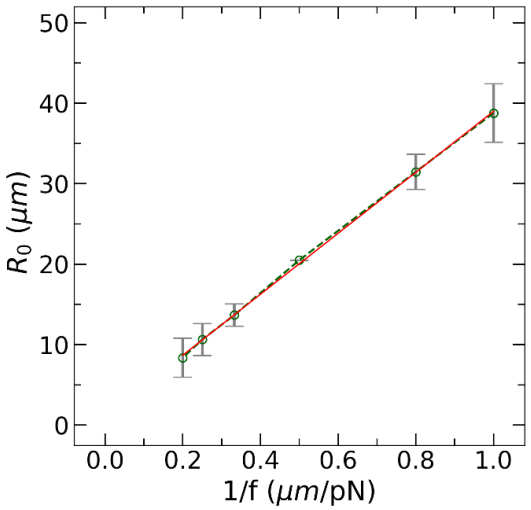
50
40
30
20
10
0
R_0 (μm)
0.0
0.2
0.4
0.6
0.8
1.0
1/f (μm/pN)

(D)

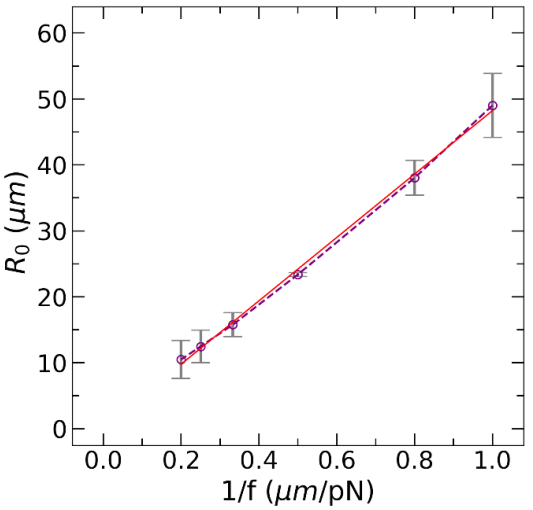
60
50
40
30
20
10
0
R_0 (μm)
0.0
0.2
0.4
0.6
0.8
1.0
1/f (μm/pN)

(E)

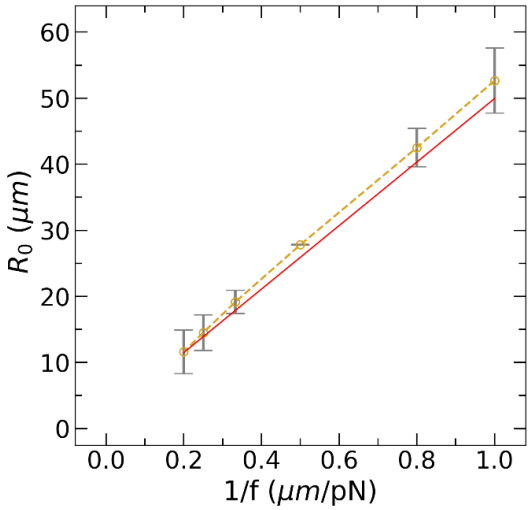

Figure 3.14: The curvature radii of microtubules are affected by the different motor densities as well as the external force density. (A) The motor density was 10 µm-2 with error. (B) With a margin of error, the motor density was 20 µm-2. (C) The motor density was 30 µm-2 with error. (D) The motor density was 40 µm-2 with error. (E) The motor density was 50 µm-2 with error. In the five pictures above, the red solid lines represent the least square linear fit (A, B, C, D and E).

According to these findings, the curvature radii R_0 are inversely proportional to the applied force density in (Fig 3.15). The proportionality is determined by the density of surface motors. The radii of the curvature increase as the motor density increases. The smooth trajectory of microtubules begins at 1.0 $pN/\mu m$ at a motor density of 10 μm^{-2}. At a motor density of 30 μm^{-2}, the microtubules exhibit smooth paths for all applied force densities. Some microtubule trajectories are detached below and above motor density 30 μm^{-2}, while all microtubules are completely detached above motor density 40 μm^{-2}. A motor density

of 30 μm^{-2} and an applied force density of 3.0 $pN/\mu m$ were used to calculate the persistence length of a microtubule.

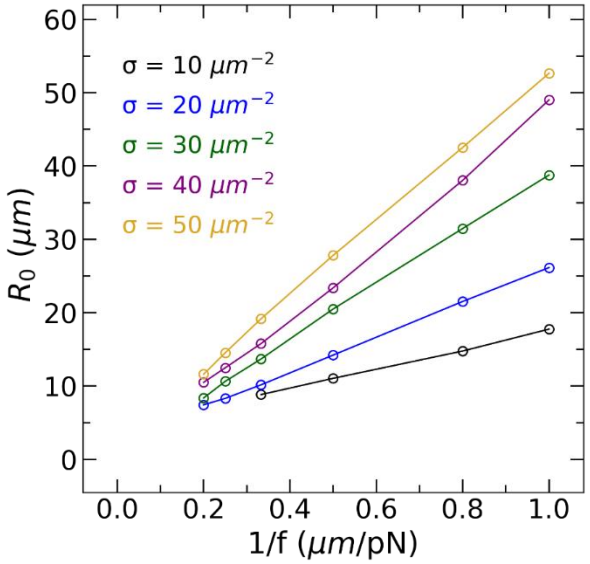

Figure 3.15: The radii of the curvature against the applied force density. This figure shows the various motor densities (Kinesins).

3.4 Measurement of the tip length of microtubule

The microtubule is driven by multiple bound kinesin molecules, as indicated by the curvature of the trajectory and the microscopic characteristics of the microtubule tips [28]. As a microtubule is driven, the leading tip of microtubule becomes longer, and it is free to fluctuate due to thermal fluctuation (Fig 3.16). The leading tip of the microtubule will gradually increase in length before binding to the next kinesin molecule as the microtubule progresses. The microtubule end looks for a new kinesin to bind to the microtubule in a specific location. The length of the microtubule end determines, where the leading tip

fluctuates, which was explained in Chapter 2. We measured tip length, defined as the length of the free-standing part between the microtubule leading end (minus-end) and the foremost kinesin motor in order to comply with the theoretical assumption [41] as shown in (Fig 3.17).

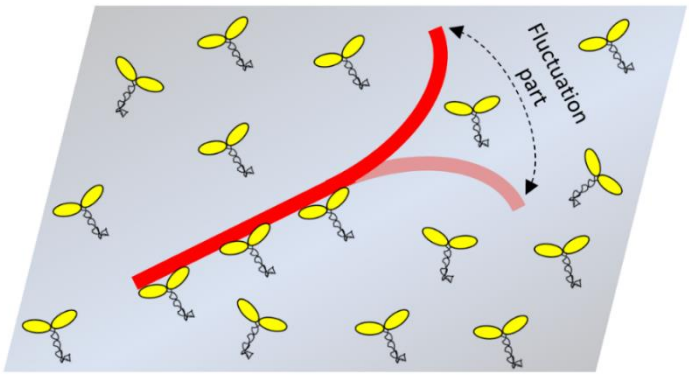

Figure 3.16: The sketch of bending microtubule follows a random trajectory due to thermal fluctuation of the leading tip.

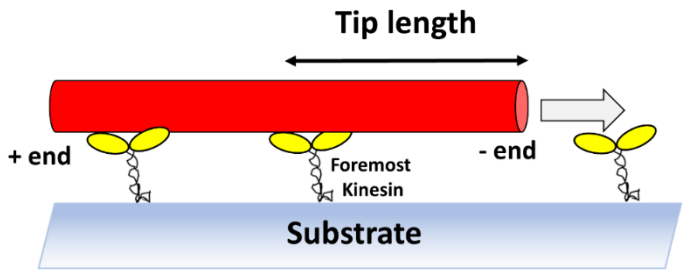

Figure 3.17: A schematic drawing of the tip length. The microtubule is represented by the red cylindrical hollow tube, and the others are as displayed in the diagram.

We measured the tip length and found its nature to be varying with the time-progression. For various motor densities and applied force

densities, the saw-teeth profile seen in (Fig 3.18) is conceivable. The tip length almost linearly elongated as the foremost kinesin moved up the microtubule plus end. The tip length suddenly shortens when a new kinesin is bound at the tip. The distribution of tip length was exponential (Fig 3.19), as predicted by random interactions between microtubules and kinesins in a previous study [25].

(A)

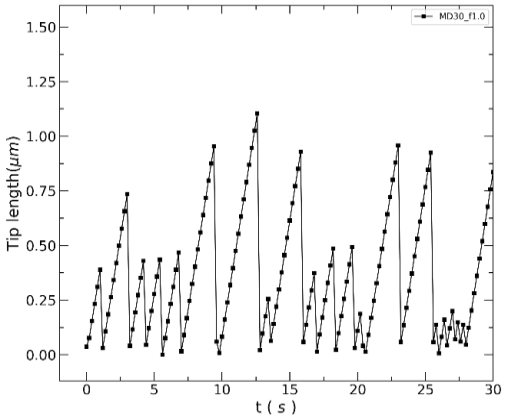

(B)

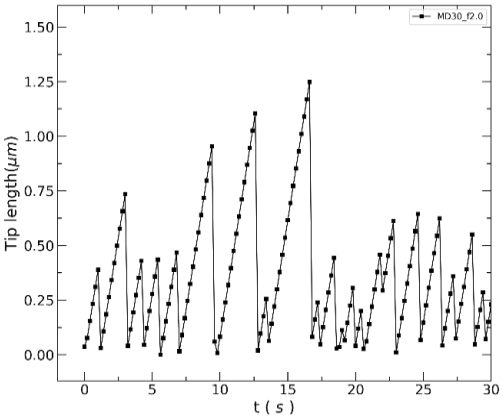

(C)

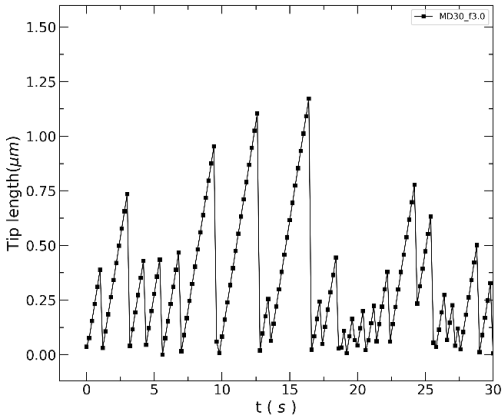

(D)

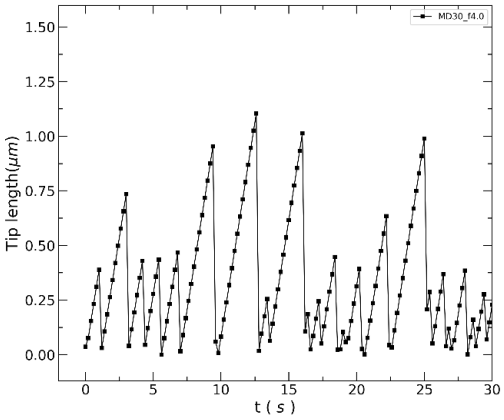

(E)

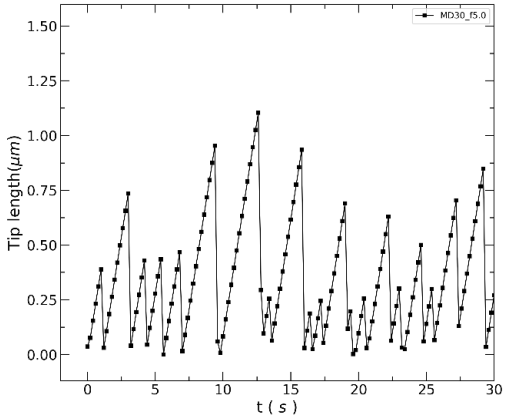

Figure 3.18: The length of a gliding microtubule's tip changes over time. (A)A motor density of 30 μm^{-2} with an applied force density 1.0 pN/μm. (A)The motor density 30 μm^{-2}, at applied force density 1.0 pN/μm. (B)A motor density of 30 μm^{-2} with an applied force density 2.0 pN/μm. (C) When the applied force density 3.0 pN/μm, the motor density is 30 μm^{-2},. (D)The motor density is 30 μm^{-2} when the applied force density is 4.0 pN/μm. (E) With an applied force density 5.0 pN/μm, the motor density is 30 μm^{-2}. As a saw-teeth profile, the entire tip length of microtubule movement is illustrated.

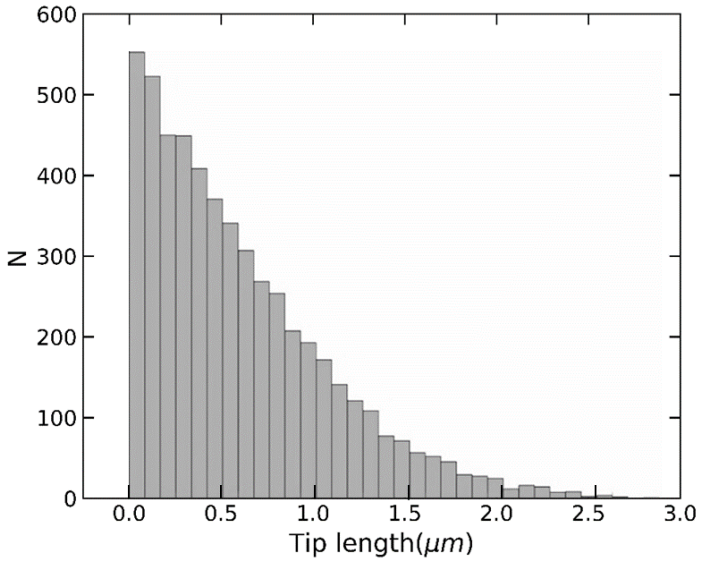

Figure 3.19: The tip length of a gliding microtubule is distributed in a frequency distribution. The Poisson distribution was implemented. The applied force density was $f = 3.0\ pN/\mu m$. The density of kinesin motor was $30\ \mu m^{-2}$.

3.4.1 Change the kinesin spring constant to determine the tip length

We measured the amount of kinesin bound to the microtubule at the surface density using the leading tip. Sometimes, microtubules move slightly differ from the kinesin motors. Kinesin motors have a spring movement after differing its can back to the trajectory ways of microtubule. In this section, we discussed at how the tip length is determined by the spring constant effect on kinesin motors. As mentioned before, we simulated the microtubules with kinesin motors under external forces by changing the kinesin spring constant as shown in (Table 10).

Table 10: shows the changing kinesin spring constants for the microtubule length parameter of 5 μm.

$\boldsymbol{BL}\ (\mu\boldsymbol{m})$	$\boldsymbol{\sigma}(\mu\boldsymbol{m^{-2}})$	$\boldsymbol{dt}\ (\boldsymbol{s})$	$\boldsymbol{f}(\boldsymbol{pN}/\mu\boldsymbol{m})$	$\boldsymbol{k}$	$< \boldsymbol{d} >$
0.25	30	0.5×10^{-6}	1.0 – 5.0	50	0.31439
			1.0 – 5.0	100	0.27425
			1.0 – 5.0	200	0.23583

According to the DHL theory, the fluctuation part of the microtubule is short when the foremost kinesin motor bound to microtubules can be treated as rigid anchors near the leading tip [41]. We further discovered that the movement of kinesin motors is dependent on their spring movement along the microtubule pathways in our simulation results. The tip length of microtubule movement is longer when the spring constant $k = 50\,pN/\mu m$. The tip length of microtubules is shorter when the spring constant $k = 200\,pN/\mu m$ is used rather than standard spring constant $k = 100\,pN/\mu m$. As a result, the averaged tip length $< d >$ decreases as the spring movement of the kinesin motors increases. The clear understanding of this explanation shown in (Fig 3.20). We could conclude from this that the foremost kinesin in our simulation may not serve as a fixed rigid anchor on microtubules.

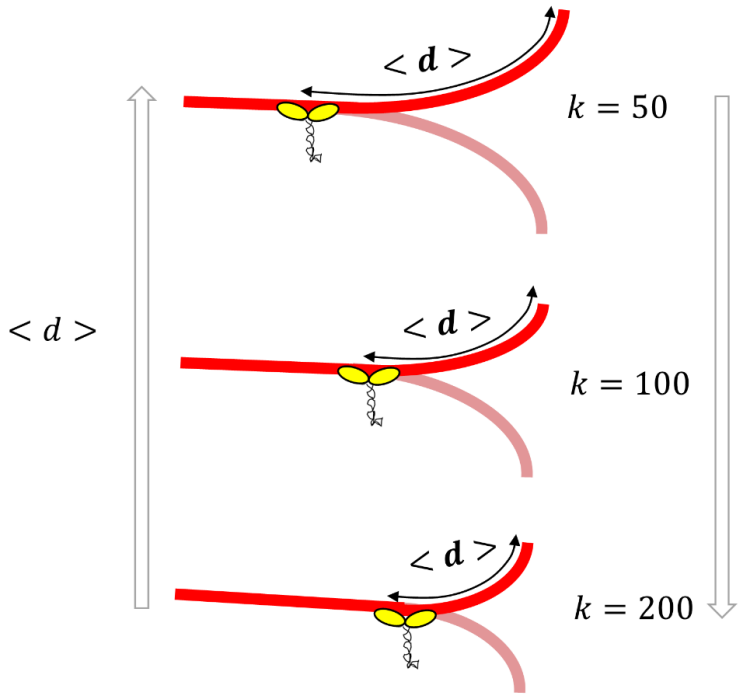

Figure 3.20: Schematic showing the determination of the tip length of microtubule depending on the kinesin motor rigid anchors point.

3.5 Calculate the path persistence length ($L_{p,path}$)

We utilized two methods to determine the path persistence length. The path persistence length ($L_{p,path}$) was calculated using the tip length of microtubule $< d >$ and considering microtubule angular fluctuation. At first, to compute the path persistence length ($L_{p,path}$) of microtubules, we used the tip length $< d >$ of kinesin attached to the microtubule at the surface density. The number of binding motors that do not bind when microtubules are moved on a kinesin surface density follows an inverse relationship with the kinesin surface density due to effects from the

moving microtubules. As a function of motor surface density, σ, the averaged value of $< d >$ was calculated various external applied forces. We used the equation (32) from section 3.2 to obtain the path persistence length ($L_{p,path}$). The next sections 3.5.1 and 3.5.2 will offer the detailed analysis of the path persistence length ($L_{p,path}$) using measured microtubule tip length $< d >$.

3.5.1 Calculate ($L_{p,path}$) from measured tip length

At first, we investigated how the applied force density f affects the tip length of microtubule movement using varied motor density $< \sigma >$ in (Fig 3.21).

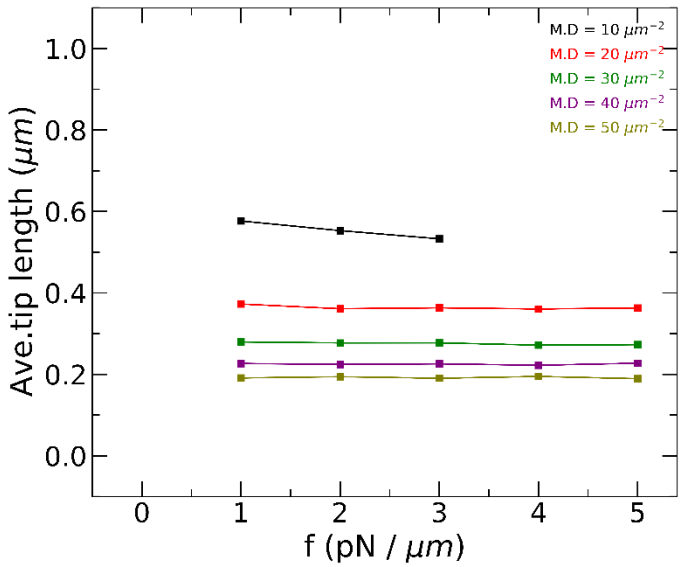

Figure 3.21: The averaged tip length against the applied force density. The lower motor densities of $10\mu m^{-2}$ are represented by the black line in figure. As illustrated in the diagram, the various colors correspond to different motor density.

We observed the average tip length of microtubule did not differ the motor density of kinesin $\sigma = 10\mu m^{-2}$ at the applied force density of $f = 1\ pN/\mu m$, $f = 2\ pN/\mu m$ and $f = 3\ pN/\mu m$. But the above the applied force density was $f = 3\ pN/\mu m$, the trajectories of microtubules were detached for motor density $\sigma = 10\mu m^{-2}$. Nevertheless, the trajectories of microtubule did not detach at high motor densities. In this research, we calculated the path persistence length ($L_{p,path}$) of microtubule using only smooth movement of microtubule. As a result, we found out that the average microtubule tip length decreased as the motor density increased but did not change significantly with the applied force densities.

When microtubules are moved on a surface density of kinesin, there is the probability for the number of motors do not bind follow an inverse relationship with the kinesin surface density due to effects from the moving microtubules. The averaged value of $< d >$ was determined as a function of motor surface density. The measurements are in agreement with the scaling model of Duke, Holy and Libeler, which predicts that $< d > \sim \sigma^{-1} w^{-1}$ [41]. As predicted from $\sigma \cdot 2w.d = 1$, in (Fig 3.22) the average tip length of microtubule was inversely proportional to the surface density of kinesins.

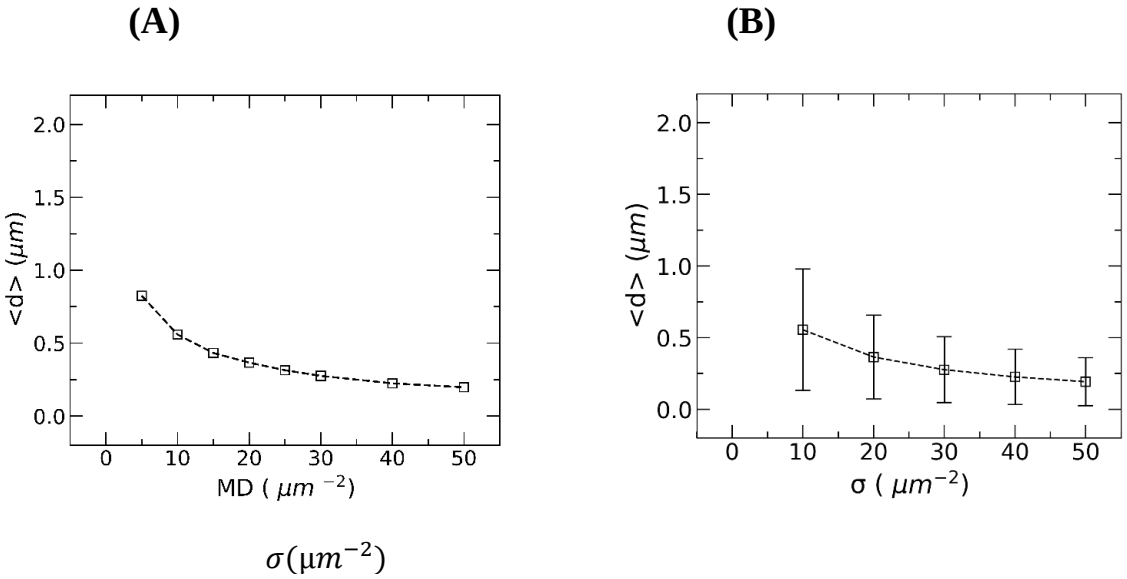

Figure 3.22: The average tip $< d >$ against the motor density. (A) The effective tip length of MT for various motor densities is shown by black line with squares. (B) The black squares with error bars indicate the average tip length of microtubule with range of motor density from $\sigma = 10\ \mu m^{-2}$ to $\sigma = 50\ \mu m^{-2}$, respectively.

We calculated the path persistence length ($L_{p,path}$) in this study by substituting the obtained the average tip length $< d >$ as represented into Eq. (31). When the motor density increased, the path persistence length decreased. The path persistence length of microtubules was discovered to be around 0.25–0.6 mm (Fig 3.23), which is much lower than the average preset filament persistence length of microtubules of 5 mm. Our simulation's comparable results, as well as the literal results shown in (Fig 3.24). We calculated the path persistence length for various motor densities in our analysis. The path persistence length obtained here is comparable to previously reported experimental values of 0.1–0.5 mm [42][28][25][43]. This simulation result revealed that

$L_{p,path}$ is not always equivalent to $L_{p,filament}$. It is important to note that the discrepancy between $L_{p,path}$ and $L_{p,filament}$ was reproduced without assuming the length-dependent rigidity of microtubule [44][45].

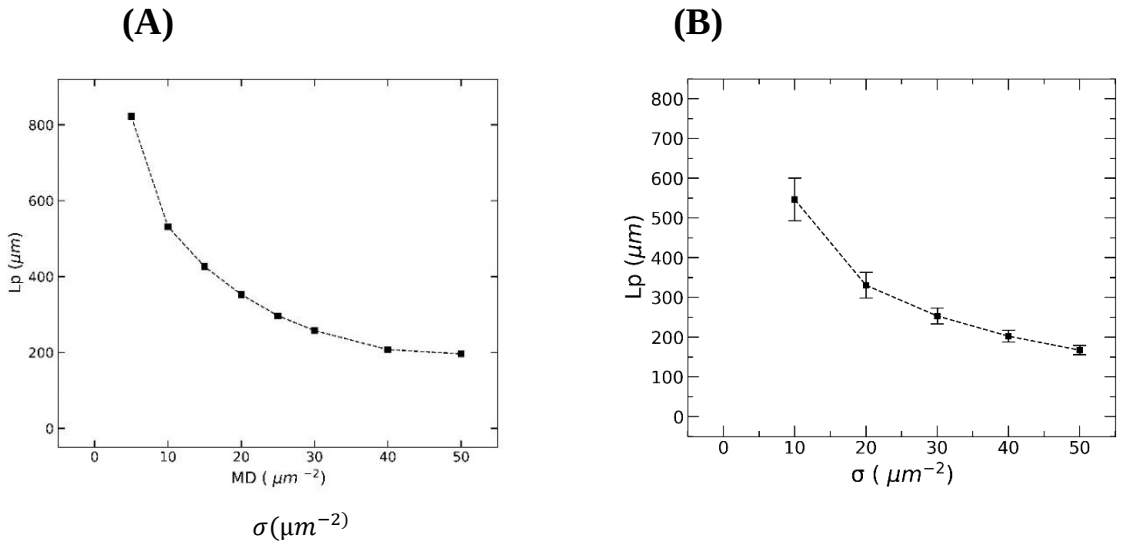

Figure 3.23: The path persistence length as a function of motor density, σ. (A) The calculated path persistence length is plotted against the various motor densities, 5 µm-2, 10 µm-2, 15 µm-2, 20 µm-2, 25 µm-2, 30 µm-2, 40 µm-2, 50 µm-2, respectively. (B) The standard values of calculated path persistence length vs motor density ranging from 10 µm-2 to 50 µm-2 with errors.

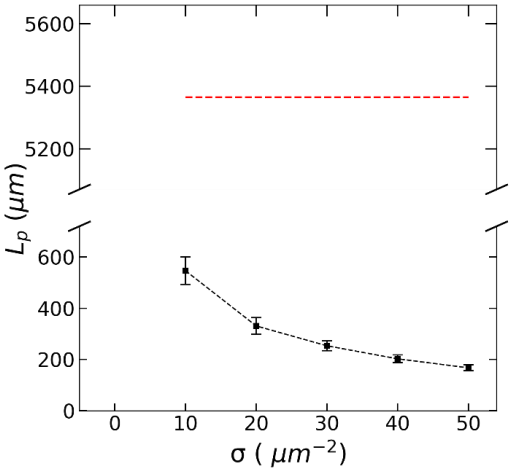

Figure 3.24: The path persistence length as a function of motor density, σ with comparable results. The filament persistence length is represented by the red broken line, which indicates the preset value.

3.5.2 Estimation of the microtubule tip length $< d >$ and spacing $< s >$

The tip length $< d >$ and spacing $< s >$ between binding kinesin motors on microtubules are discussed in this section. According to the Duke, Holy and Leibler devised a theory (DHL) that predicts how the average spacing of motors on filaments $< s >$, should change in proportion to motor surface density, σ [41]. The free tip of the microtubule filament does not have time to explore the surface before reaching a motor at high kinesin surface density as mentioned in regime I (Fig 3.24) thus the area explored by the filament tip is determined by the capture radius of the motor, w. The average spacing of the motors will be $\langle d \rangle \sim \sigma^{-1} w^{-1}$.

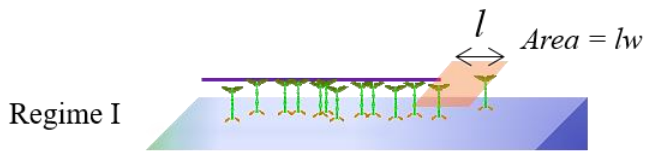

Figure 3.24: A cartoon illustration of the regime I of DHL theory. The kinesin motors are so dense in regime I that the bound kinesin spacing is determined by the kinesin's capture radius (w). [46]

We followed the same concept as Uyeda et al. and Duke et al., which were previously discussed. The estimates for tip length and spacing, as indicated graphically in (Fig 3.25), have been used in our simulation analysis. The average tip length, $< d >$, spacing $< s >$, can be calculated using the following formula:

$$\langle s \rangle = \frac{L}{2\sigma L w} \qquad (50)$$

$$\langle d \rangle = \frac{1}{2}\langle s \rangle \qquad (51)$$

where σ is the motor density on the substrate and L is the length of microtubules. To estimate the kinesin of tip length $< d >$, we apply the equation of capture radius for the lower limit $w = 20\ nm$ and the upper limit of $w = {}^{F_{detached}}/_{k}$, 70 nm which is the maximum extension of kinesin motors on microtubules. In our simulation, we used the detached force is $F_{detached} = 7pN$ and kinesin motor spring constant is $k = 100\ pN/\mu m$. The estimated results of the tip length and spacing between kinesins on microtubules were shown in (Fig 3.26 and Fig 3.27).

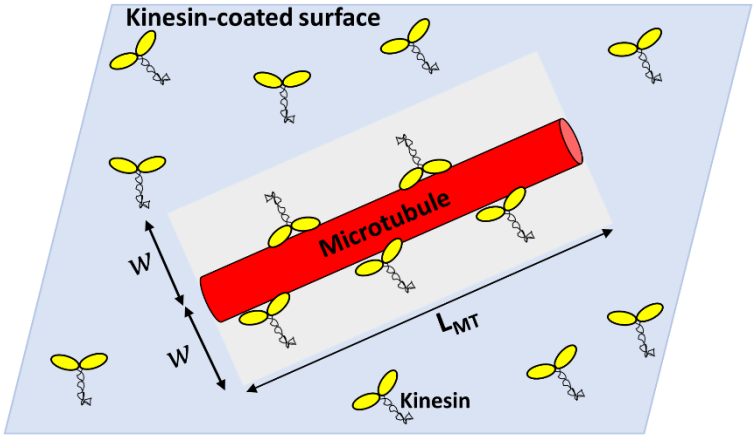

Figure 3.25: The tip length and spacing between binding kinesins on microtubules are graphically represented.

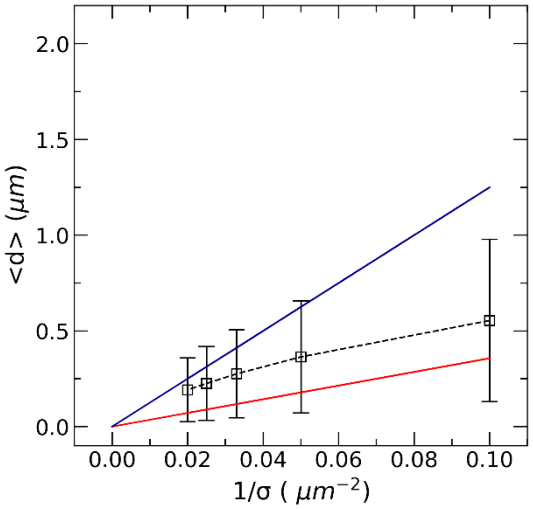

Figure 3.26: The average tip length of microtubules is plotted against the inverse of motor density. The upper and lower estimations are represented by the blue and red lines, respectively.

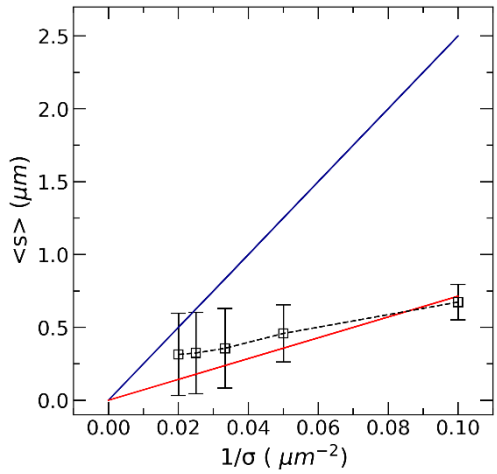

Figure 3.27: Inverse of the motor density, the average spacing between binding kinesins on microtubules. The blue and red lines show the highest and lowest estimates, respectively.

3.6 Calculate the ($L_{p,path}$) from the angular fluctuation of microtubules

We calculated the angular fluctuation of microtubule segments to test the theoretical assumption that the length of the bending part of microtubules is equal to the tip length. The angular fluctuation of segments composed of microtubules was measured to see how discrepancy emerged. We described the microtubule trajectory using variance angle and their contour length. The variance angles, θ, to each point along a trajectory are calculated by averaging the cosine of the angle difference for every set of points separated by a contour length, as shown in (Fig 3.28). The variance of microtubule segment angular fluctuations was measured as a function of contour distance from the microtubules' leading ends in (Fig 3.29).

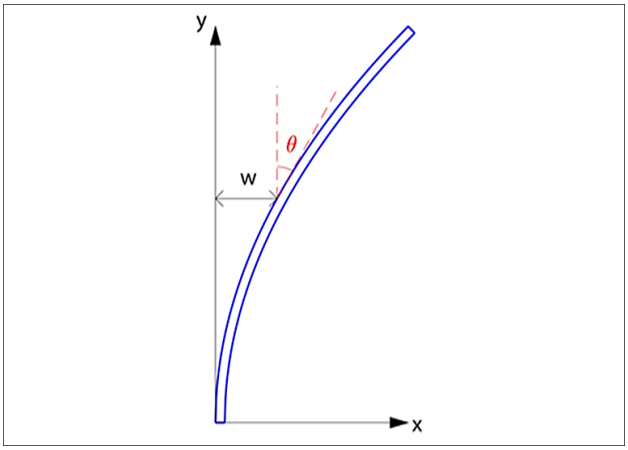

Figure 3.28: Schematic diagram of the measured the variant of correlation angle from the path trajectory curvature of the microtubule.

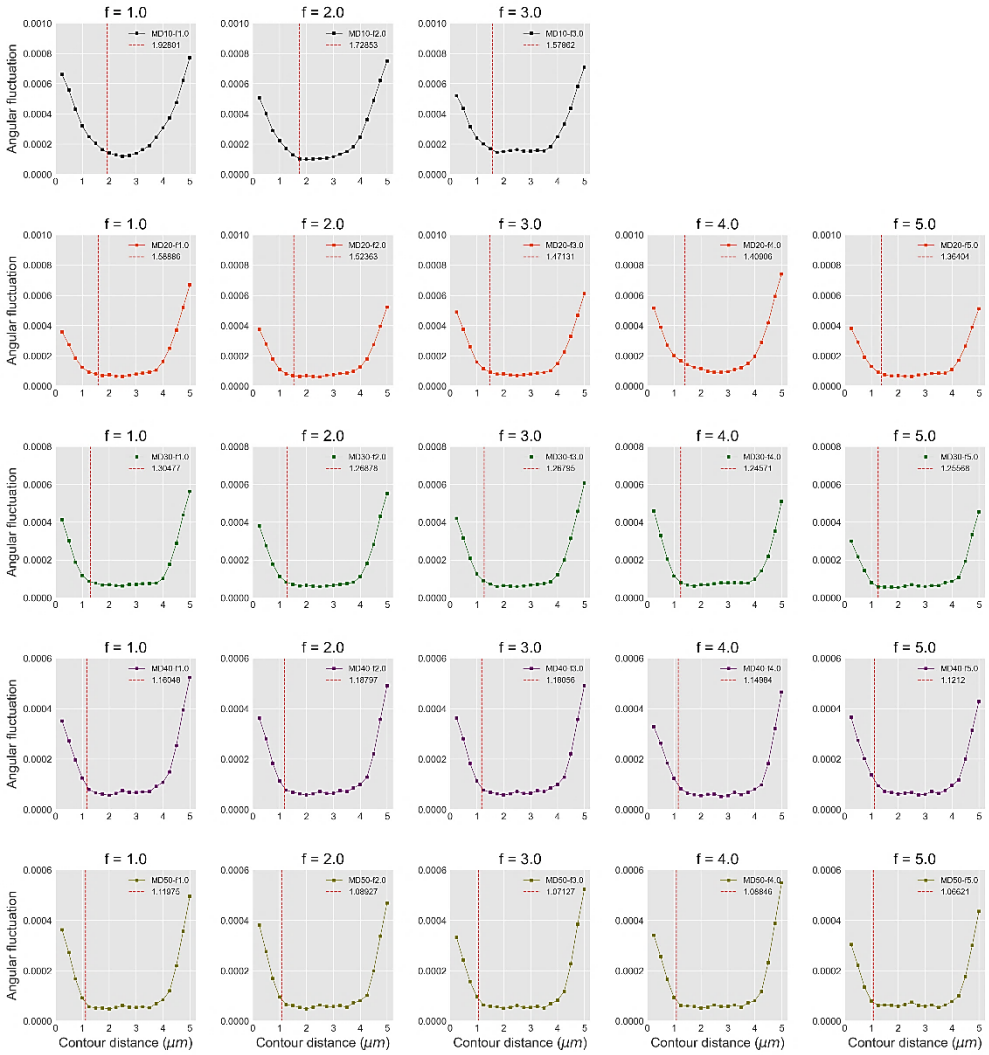

Figure 3.29: Microtubule segments' angular fluctuation at various locations, as indicated by contour distances from their leading tips (minus ends). The solid lines with full squares indicate the angular fluctuation of the MT segment at various external force densities (f = 1.0 pN/μm, 2.0 pN/μm, 3.0 pN/μm, 4.0 pN/μm and 5.0 pN/μm) with the motor density of 10 μm-2 (the first row), 20 μm-2 (the second row), 30 μm-2 (the third row), 40 μm-2 (the fourth row) and 50 μm-2 (the fifth row). The predicted length of the bending part of microtubules is shown by the red dashed lines.

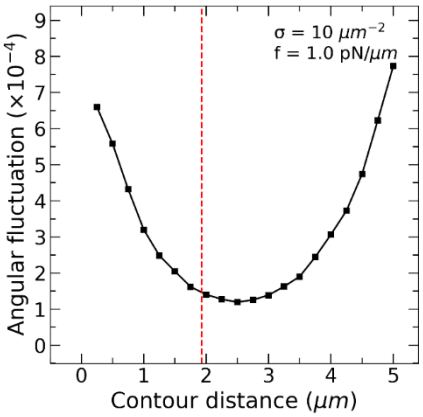
σ = 10 μm^{-2}
f = 1.0 pN/μm
Angular fluctuation (×10^{-4})
Contour distance (μm)

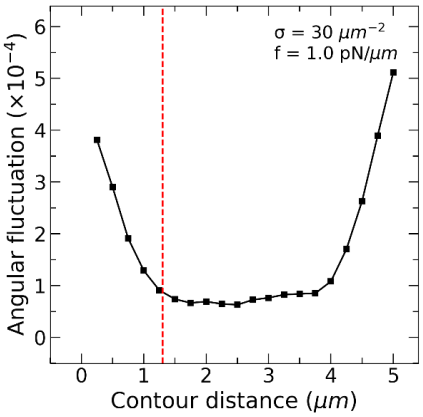
σ = 30 μm^{-2}
f = 1.0 pN/μm
Angular fluctuation (×10^{-4})
Contour distance (μm)

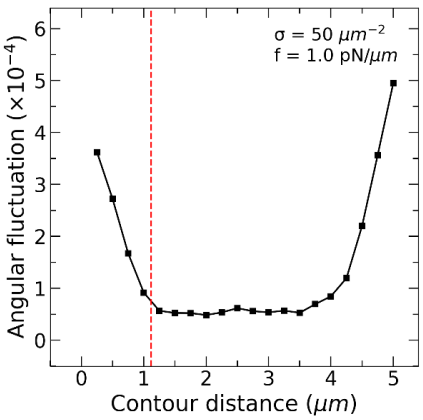
σ = 50 μm^{-2}
f = 1.0 pN/μm
Angular fluctuation (×10^{-4})
Contour distance (μm)

Figure 3.30: Angular fluctuation of microtubule segments at motor density $\sigma = 10\ \mu m^{-2}$, $30\ \mu m^{-2}$ and $50\ \mu m^{-2}$, respectively for applied force density $f = 1.0\ pN/\mu m$. The length of the bending part of the microtubule is indicated by the broken red line.

The angular fluctuations at both ends of microtubules were significantly larger than those at the central parts of microtubules, according to several measurements. Since the measured tip length of microtubule was 0.25-0.6 μm as determined in Section 3.5.1 (Fig 3.23), the length of the bending part of the microtubules was longer than that assumed by Duke et al [41] in theoretically.

3.6.1 Comparison between microtubule bending part and tip length

We calculated the length of the bending part of microtubules using the obtained R_0 values and the preset value of filament persistence length ($L_{p,filament}$) to determine if the extended length of fluctuating parts is realistic in our simulation. The length of the microtubule bending part, along with the binding kinesin motor anchors, is represented in (Fig 3.31). The length of the bending part was calculated to be 1.1-1.7 μm (see, Fig 3.32) by substituting the obtained values of R_0 and other preset parameters into Eq (30.2) and solving for the tip length $< d >$. The calculated length of the bending part is approximately three times longer than the previously calculated tip length (defined as the distance between the microtubule leading tip and the foremost kinesin in (Fig 3.33)), and it agrees well with the length of the fluctuating part obtained from the fluctuation analysis (see section 3.6).

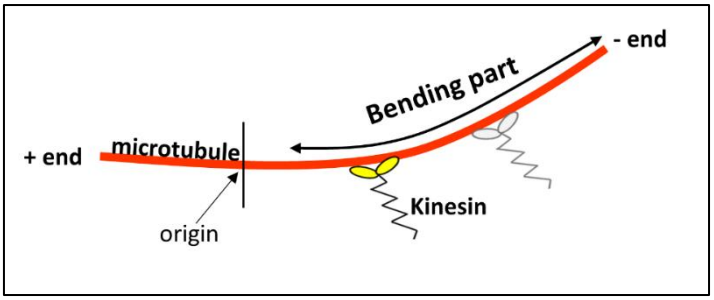

Figure 3.31: Figure 3.31: A diagram explaining the microtubule bending part's length. The length of the microtubule from the origin to the bending part is described by the red rigid rods. The bending part occurs at the microtubule leading ends (minus-end).

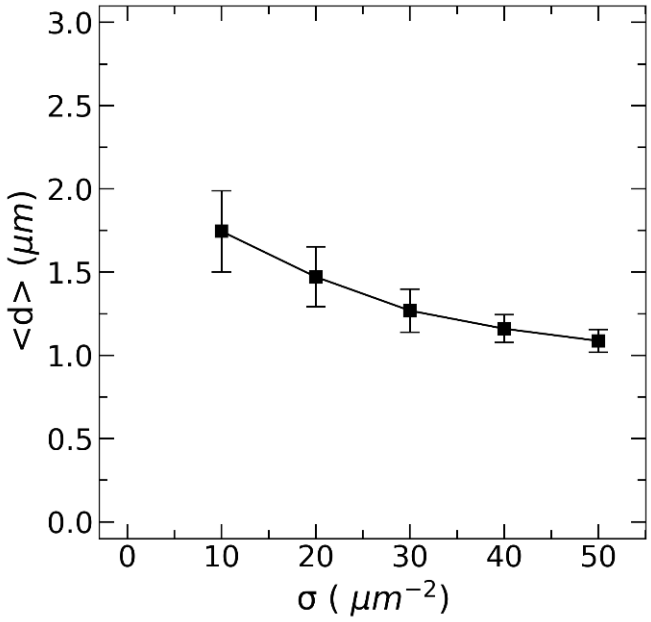

Figure 3.32: The indicated plot shows the length of a microtubule's bending part. The bending part of the microtubule against the surface motor densities with the error as represented by the bold solid line.

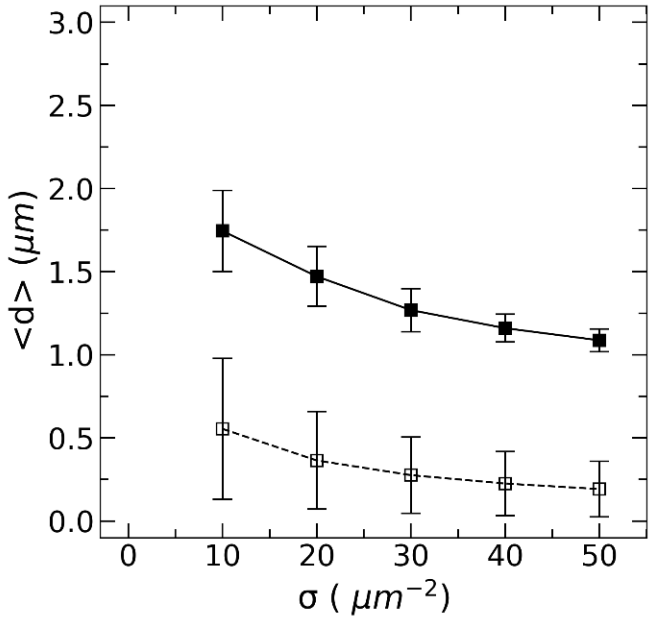

Figure 3.33: The averaged tip length and the length of the microtubule's bending part are compared. The length of the bending part is shown by the solid squares, while the length of the tip is represented by the open squares.

3.6.2 Interpretation of microtubule fluctuation

Our extensive investigation supports up the general statement that kinesins may not act as rigid anchors, allowing the fluctuating part of the microtubule to extend beyond the length between the leading tip of the microtubule and the foremost kinesin, as illustrated schematically in (Fig 3.34). Because the average separation between neighboring kinesins on microtubules was 0.35-0.67 μm (Fig 3.27), two or three kinesin motors bind to microtubules within the bending part of microtubules on average.

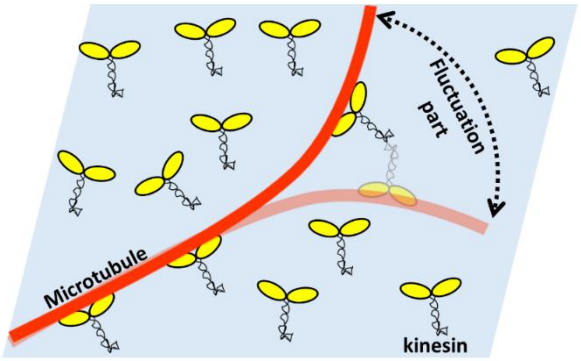

Figure 3.34: Figure 3.34: A schematic interpretation of the microtubule segments' angular fluctuation over the kinesin-coated surface.

3.7 Movement of microtubule under high external forces

The movement of microtubules under high external forces on a kinesin-coated surface discuss in this section. The flow of the above expression, as described in section 3.1, were basically followed for this study. In our simulation, we used the following parameters: (see Table 11). Microtubules were arranged so that the high external force was perpendicular to the setting. As a result, it became as shown in (Fig 3.35). Here, a high external force is applied from the left side to the right side in this case. We demonstrated the superimposed snapshots of configurations of a microtubule moving over kinesin motors with a lower surface motor density of $10\mu m^{-2}$ under a high external force of $5.0\ pN/\mu m$. From Fig 3.35, it can be seen that microtubules are affected by external force. From this, it was found that the external force can be expressed by this program. In addition, a graph as shown in (Fig 3.36) was created from the simulation results. It is a graph that follows the trajectories of the microtubule under high external forces. From this, it

can be observed that the higher external force, the larger the effect on microtubules.

Table 11: Table below presents the detach microtubule simulation's parameter values.

L_{MT}	Bound Length (BL)	Time step (dt)	Total simulation time (T)	Number of Assay
5 μ*m*	0.25 μ*m*	0.5×10^{-6}	30 *s*	50

(A)

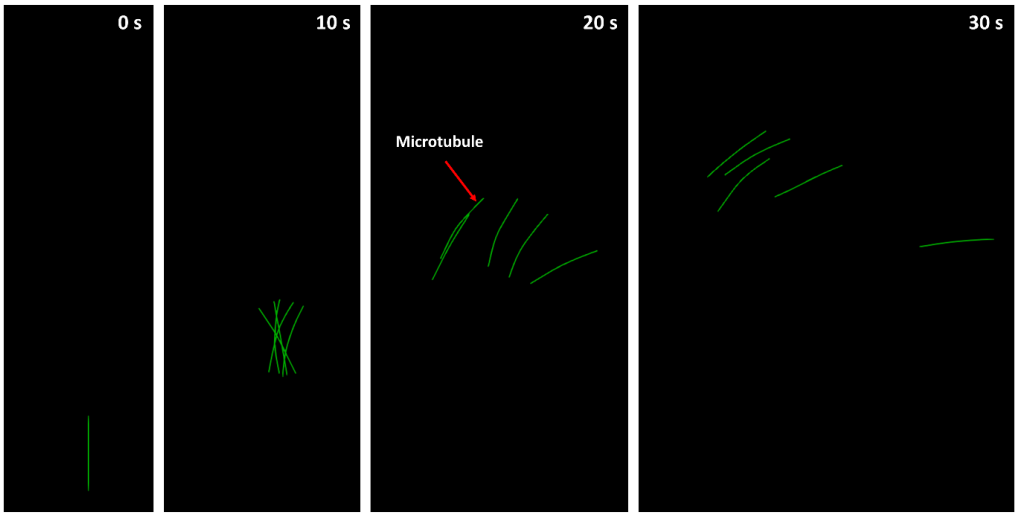

(B)

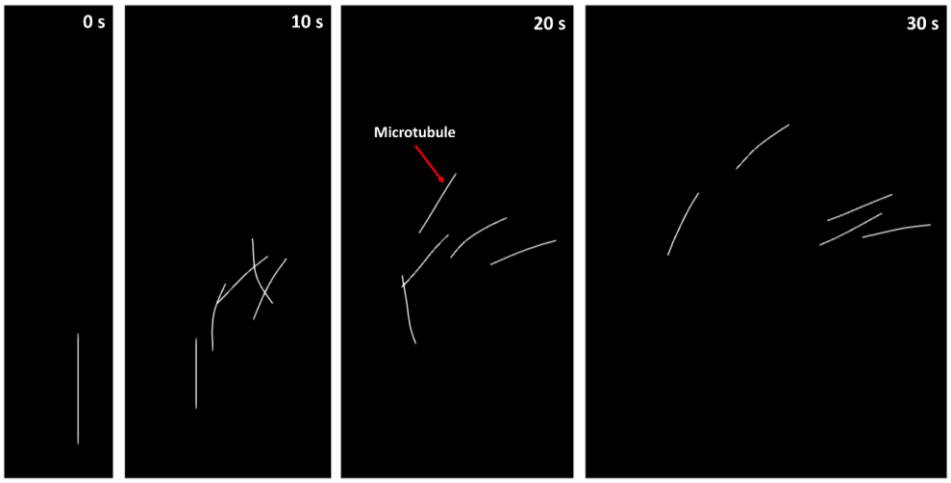

(C)

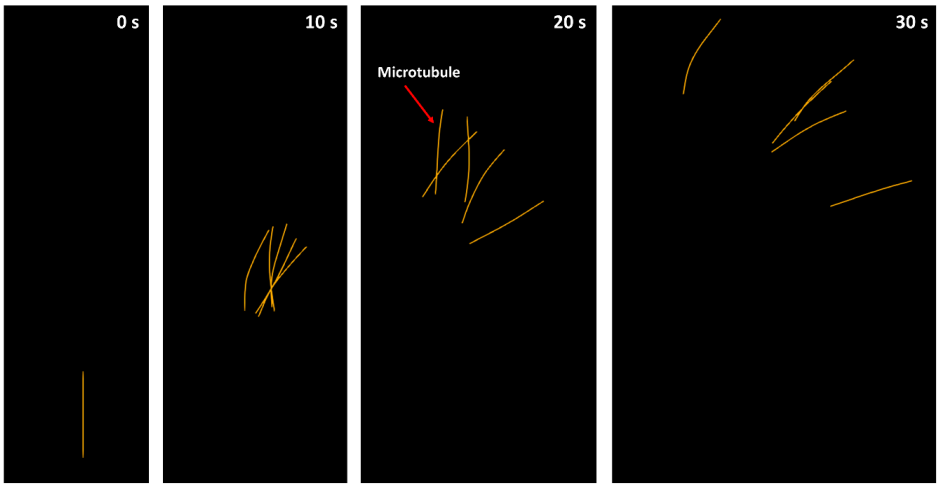

Figure 3.35: The movement of microtubules oriented perpendicular to external forces was illustrated in this simulation image. Figures (A, B and C) demonstrated the microtubule trajectories for lower surface motor density $\sigma = 10\mu m^{-2}$, at under a high external force of $f = 5.0\ pN/\mu m$.

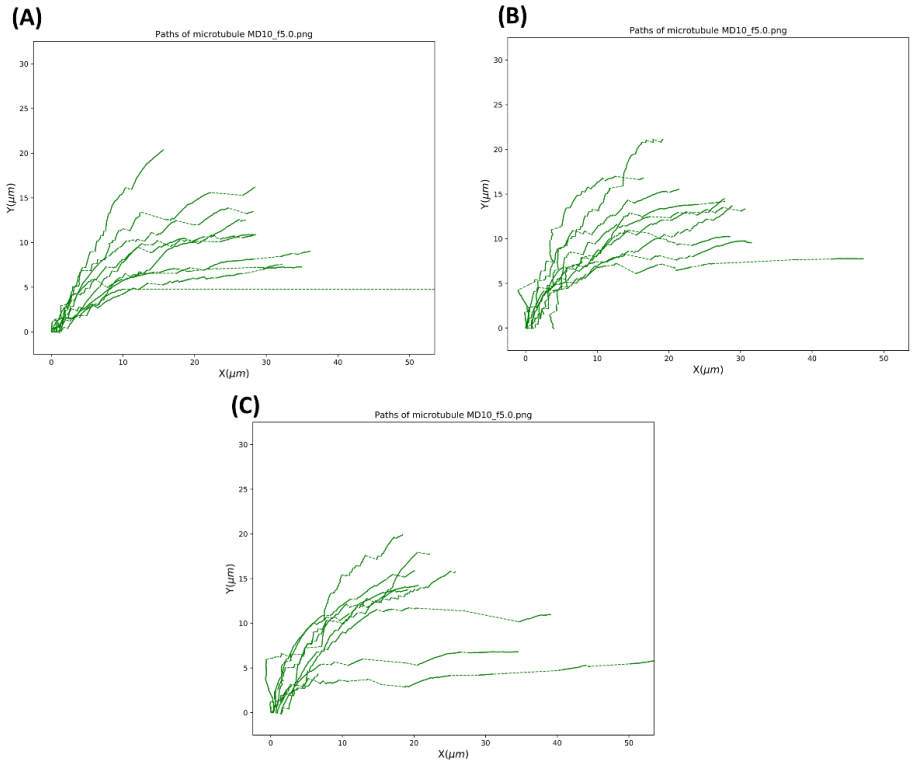

Figure 3.36: The trajectories of detached microtubules under high external forces $f = 5.0\, pN/\mu m$ at motor density $10 \mu m^{-2}$. (A, B and C) The three graph represent the10th microtubule trajectories detached for each.

3.7.1 Investigation of the detach position of microtubule

The trajectories revealed (Fig 3.37) that they were discontinuous, indicating partial or complete microtubule detachment from the surface. Trajectories with a higher motor density but a lower external force, on the other hand, did not exhibit the same intermittencies. The control of microtubule movement was declined because partial and complete microtubule detachments occurred stochastically. The moving speed was irregular and disturbed by horizontal sliding. The microtubule detached after moving horizontally. External force induces horizontal

movement and dissociation, according to experiments. Our simulation demonstrated that we had a good working relationship with them.

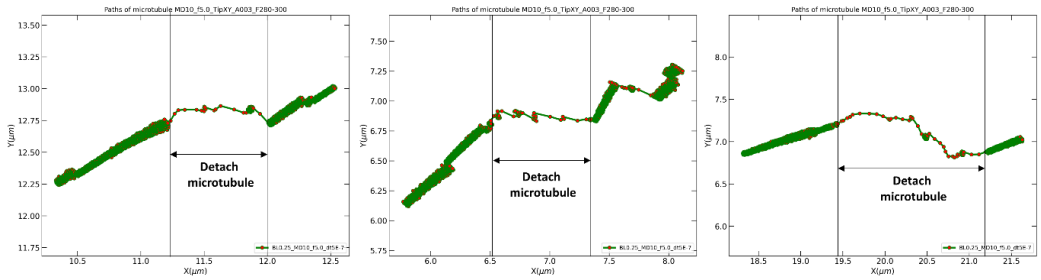

Figure 3.37: Representative trajectories of microtubule movement over kinesin motors with a surface motor density $10\mu m^{-2}$ under a high external force of 5.0 $pN/\mu m$. The arrows region indicated the microtubule detach movement during the 30 sec time step in the simulation.

3.7.2 Microtubule binding motors along the time step

The kinesin binding motors to the microtubule are examined in this section. Kinesins are randomly distributed on the surface, according to our simulation model. Howard et al. [47] previously observed spontaneous detachment at a high rate in experiments using very low densities of kinesin and short microtubules, before the microtubule unbinds from the last kinesin holding it, it is quite likely that it will be unable to contact another kinesin. Our close examination of microtubule movement on surfaces coated with a low motor densities with a typical microtubule lengths 5 μm [20], the microtubule detachment occurred.

We analyzed the motor binding rate with a certain time step to check the position of detach microtubules along their moving

trajectories with the kinesin motors (Fig 3.39). We calculated the binding motor density using Eq (30.3) as estimated ($N_{motor} = \sigma \cdot L_{MT} \cdot 2w$), kinesin may easily bind to microtubules when its radius of capture is 20 nm. When the kinesin radius of capture is 70 nm, microtubules fluctuate, making it difficult to reach the microtubule with kinesin motors. As a result, the estimated kinesin binding motor was ≈ 7. So that, kinesin motors to reach the microtubule is difficult. The estimated binding motor rate and our simulated binding motor number were in good agreement.

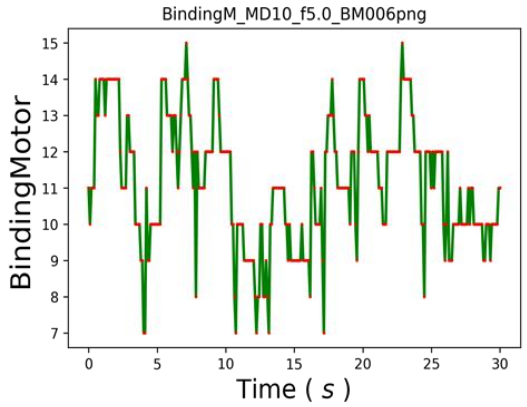

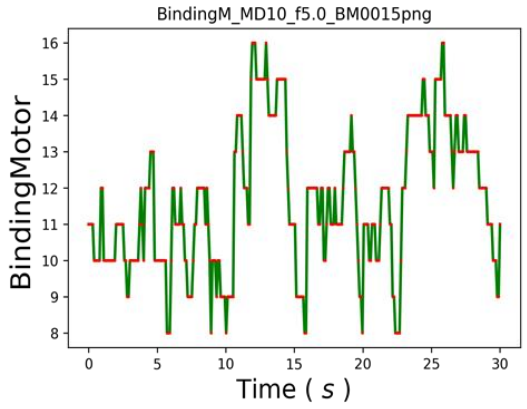

Figure 3.39: Microtubule binding motor vs time step. The motor density was 10 $10\mu m^{-2}$, the applied external force density was 5.0 $pN/\mu m$.

3.8 Calculation of microtubule leading tips and trailing ends

We examined at both the leading tips and the trailing ends of microtubules to see whether they became detached. In our simulation, we determined the trajectories of the detach movement for the leading tips and trailing ends of microtubules over kinesin motors with a surface motor density of $\sigma = 10\ \mu m^{-2}$ at an external force density of $f = 5.0\ pN/\mu m$ (Fig 3.40). The microtubules moved forward when the force density was increased, eventually dissociating from the motor's substrate. The leading tips of the microtubule were not followed by the microtubule. At the same occasion, we noticed that the microtubule tailing end had detached.

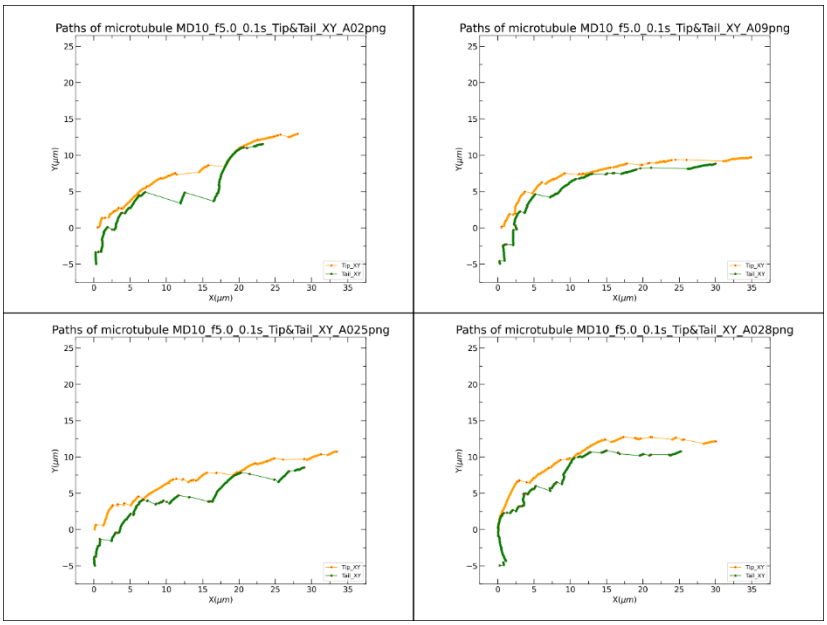

Figure 3.40: The detach microtubule movement paths along their leading tips and trailing ends. The leading tip of the microtubule is represented by the orange dissociation paths. The green dissociation trajectories show the microtubule's trailing end.

The intermittencies of the trajectories were measured by determining the instantaneous speed of the leading tips and trailing ends. The instantaneous speed was determined using the formula $v = d/t$, where v represents the speed of the microtubule trajectories, d represents the distance between microtubules along their trajectories, and t represents the time step of the microtubule movement in our simulation. We calculated the time evolution of the instantaneous speeds for sixty simulated microtubule trajectories based on these findings, which indicated distinct isolated peaks over an average speed of $0.8\ \mu m/s$, indicating partial and complete microtubule detachments (Fig 3.41). At the peaks, instantaneous speeds could reach 50 times the average speed of $0.8\ \mu m/s$. The instantaneous speed was distributed exponentially. The distributions of the leading tips and trailing ends did not differ significantly (Fig 3.42). Detachments happened equally from the leading tips and trailing ends, according to this observation (Fig 3.38).

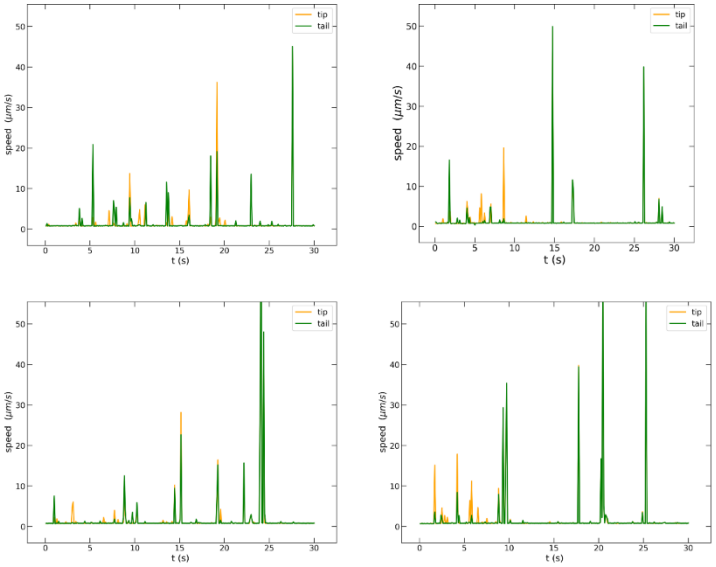

Figure 3.41: Instantaneous speeds of the leading tip and trailing end of a microtubule over time.

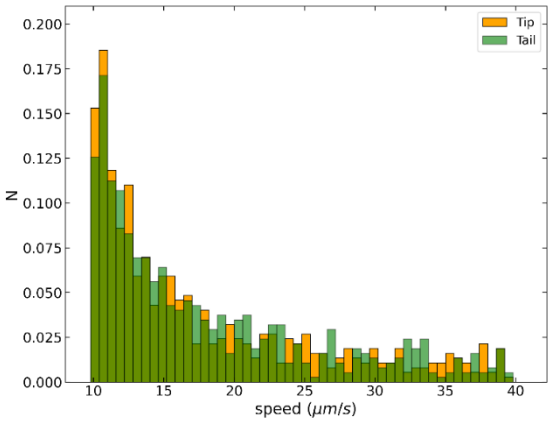

Figure 3.42: Histograms of the instantaneous speeds of 60 microtubules' leading tips and trailing ends. Only the segment with a speed > 1.0 µm/s is displayed to emphasize the abrupt changes in gliding speed corresponding to the peaks in Fig 3.41.

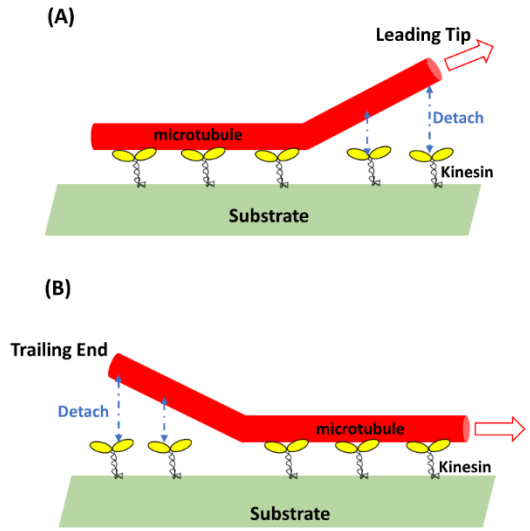

Figure 3.38: Schematic diagram of the microtubule detachment from binding motor densities. (A) The microtubule leading tip detaches. On the microtubule, kinesin motors are difficult to bind. (B) Microtubule detachment occurs at the trailing end. The microtubule is not anchored by kinesin anchors.

3.9 Classification of the microtubule detachment

We simulated the several microtubules under high external force was 5.0 $pN/\mu m$, over the kinesin coated surface as described in section 3.6. With a 0.1 second time resolution, we were able to observe multiple microtubule movements (Videos of each detached microtubule movement can be viewed in the APPENDED SECTION, CD(A)-D3.9-v1). Detachment events could be directly observed and manually counted by analyzing the peak detection of the microtubule leading tips and trailing ends as discussed in section 3.8. According to the above determination results, there are two types of detachment events that can be observed: Unzipping/swiveling and jumping are two of the main categories. With 0.1 sec time resolution, the figures below demonstrate

the observed types of microtubule unzipping/swiveling and jumping events change the process (Fig 3.43 and 3.44). In the following section (3.9.1 and 3.9.2), we will go through each process and mechanism in detail.

(A)

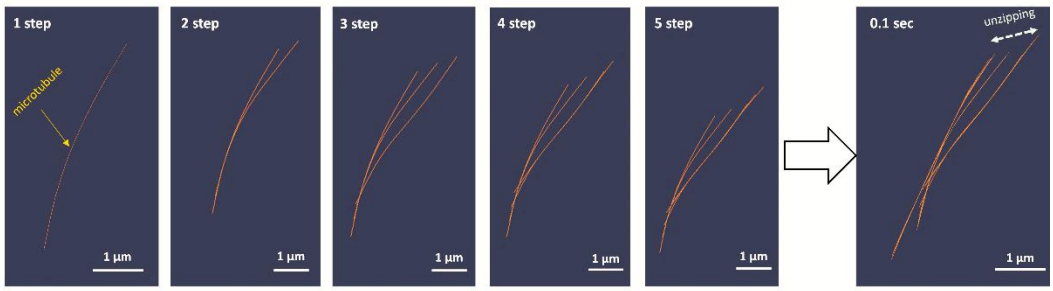

(B)

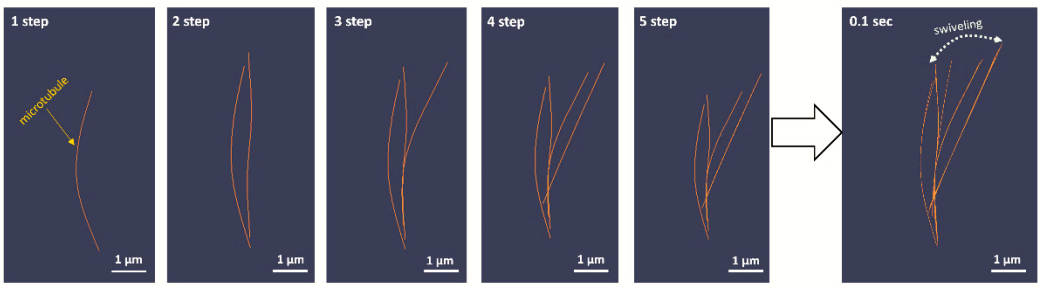

Figure 3.43: Unzipping/swiveling movement. (A) Time resolution of 0.1 seconds for unzipping detached microtubule movement. (B) Time resolution of 0.1 sec for swiveling movement of detached microtubule. A microtubule's superimposed conformations are represented by the orange lines. The

behaviors of the microtubule detach movement are indicated by the white dashed arrow lines.

(C)

Figure 3.44: Microtubule jumping movement with 0.1 second time resolution. The microtubule jumping detachment movement is represented by the orange lines. For each time step, the white dashed arrow lines show the jumping step.

3.9.1 Unzipping/swiveling of microtubule

The unzipping/swiveling category of microtubule occurred during the moment of microtubule detachment. The process of unbinding kinesin motors from either the leading tip or the trailing end of microtubules is called as unzipping. The statistical simulated impacts of the unzipping/swiveling movement among the sixty microtubule trajectories shown in (Table 12). A representative microtubule undergoing unzipping followed by swiveling is shown in (Fig 3.43A). Firstly, we simulated the microtubules under high external forces $5.0\ pN/\mu m$ with a motor density of $10\ \mu m^{-2}$ and time resolution of 0.1 sec.

Table 12: Observed detachment events, unzipping/swiveling movement of microtubules with 0.1 sec time resolution

Motor density (σ)	External force (f)	Total simulation time (T)	Time resolution	Number of observed microtubules	Unzipping/swiveling events number
10 μm^{-2}	5.0 $pN/\mu m$	30 sec	0.1 sec	60	36

The phenomena of microtubule detachment could not be clearly identified due to the 0.1 sec time resolution. We magnified with 1,000 times higher time resolution to determine the precise phenomenon of microtubules in (Table 13). The path of the microtubule shifted a few of times see in (Fig 3.45). The population of binding kinesin motors was gradually replaced as the zip was unzipped. Microtubules showed thermal fluctuations between shifts, but the population of binding kinesin motors did not change. Swiveling of microtubules occurred sometimes after unzipping, causing significant changes in their gliding direction.

It was found that unzipping from leading tips affected trajectories more than from trailing ends, since their leading tips determine most of their trajectories. A higher percentage of unzipping and swiveling events

took place when the microtubules moved perpendicular to an applied force.

Table 13: Observed detachment events, unzipping/swiveling movement of microtubules with 0.1 msec time step

Motor density (σ)	External force (f)	Total simulation time (T)	Time resolution	Unzipping/swiveling events number
10 μm^{-2}	5.0 pN $/\mu m$	30 sec	0.1 $msec$	7

(A)

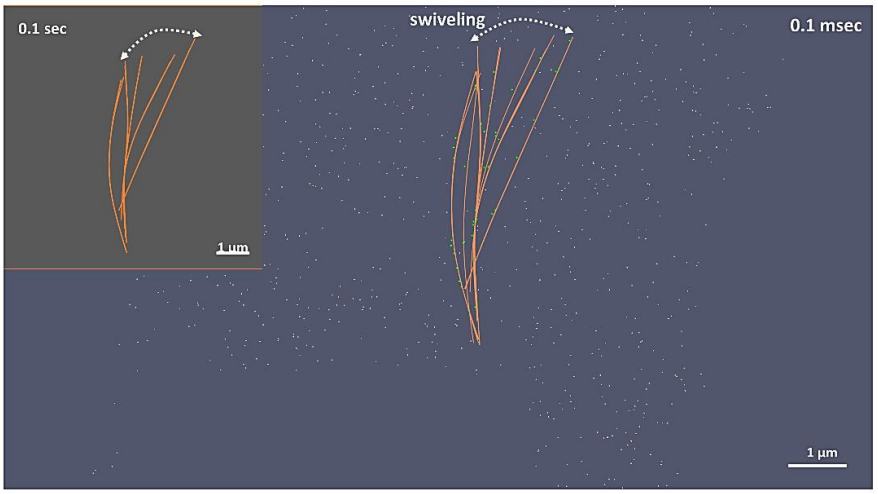

(B)

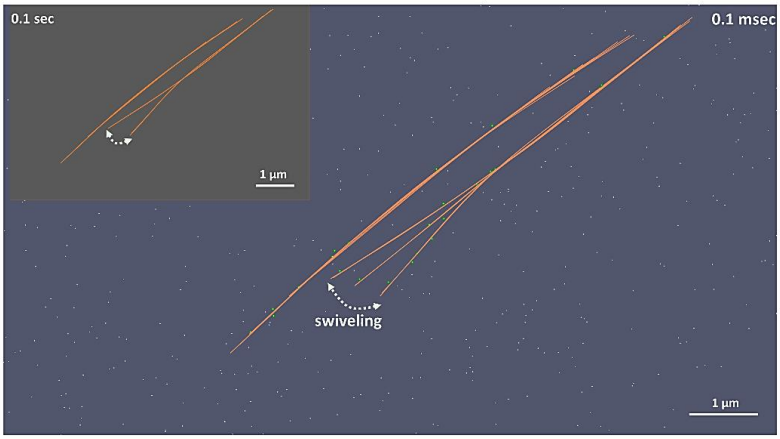

(C)

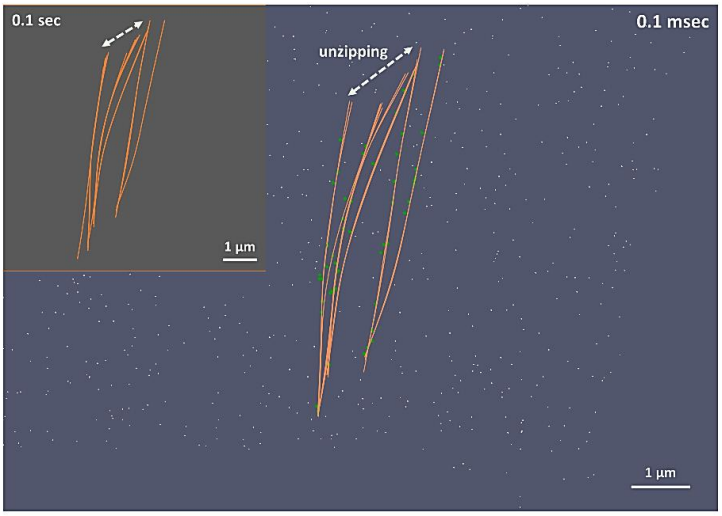

Figure 3.45: Unzipping and swiveling observed with 0.1 msec time resolution. (A) On the left side, the swiveling movement of microtubule which has a 0.1 sec time resolution and the right-side, 0.1 msec time resolution of the swiveling movement. (B) Swiveling movement of microtubules, as a result, 0.1 msec is magnified by 0.1 sec in the left and right figures. (C) Both figures indicate the unzipping movement of microtubule. The orange lines represent

a microtubule's superimposed conformation. In this case, white dots represent motors of the kinesin motors. As the kinesin motors attach to microtubules, green dots are visible on them.

3.9.2 Jump of microtubules

To the basis of evidence, the jumps occurred suddenly within 0.1 seconds of the time resolution. The statistical simulated impacts of the jumping microtubule among the sixty trajectories shown in (Table 14). The 0.1-second time resolution, however, made it difficult to identify the phenomenon of microtubule detachment. Microtubules were observed with a 1,000-fold increase in time resolution (Table 15). In many cases, microtubules simply shifted downstream of the applied force without any significant change in direction. (Fig. 3.46) shows a microtubule undergoing a jump with 0.1 msec time resolution. Upon jumping, a whole binding kinesin motor population was replaced. It is possible to cover a distance that is greater than the length of microtubules in a single jump. Jumps observed with a 0.1 sec time window consisted of smaller jumps without changing the direction of microtubules, the studies observed.

Table 14: Observed detachment events, jumping movement of microtubules with 0.1 sec time resolution

Motor density (σ)	External force (f)	Total simulation time (T)	Time resolution	Number of observed microtubules	Unzipping/swiveling events number
10 μm^{-2}	5.0	30 sec	0.1 sec	60	24

Table 15: Observed detachment events, jumping movement of microtubules with 0.1 msec time step

Motor density (σ)	External force (f)	Total simulation time (T)	Time resolution	Unzipping/swiveling events number
10 $\boldsymbol{\mu m^{-2}}$	5.0 $pN/\mu m$	30 sec	0.1 $msec$	8

All along the trajectories, microtubules jumped with almost equal frequency. lowering the applied force from 5.0 $pN/\mu m$ to 4.0 $pN/\mu m$ greatly diminished the jump of microtubules.

(A)

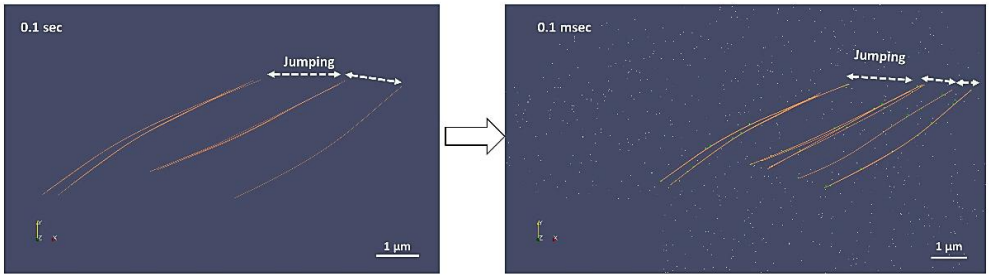

(B)

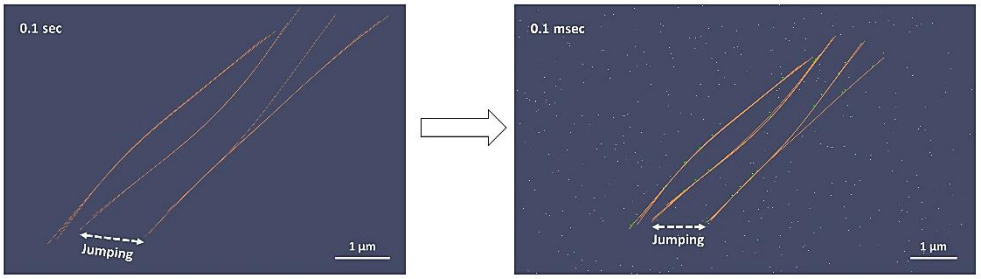

(C)

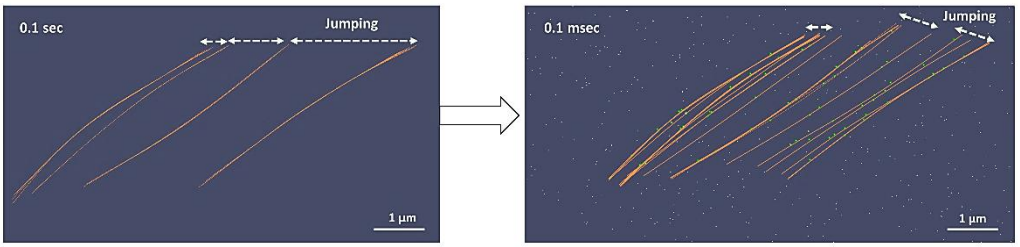

Figure 3.46: Observation of small jumps with time resolution of 0.1 msec. (A) On the left is a time resolution of 0.1 seconds, while on the right is 0.1 microseconds. (B) These figures represent the microtubule's jump to the left

and to the right, respectively. (C) In the left figure, the jump microtubules are shown with a time resolution of 0.1 seconds. We have magnified the time resolution by 1,000 times at the right side. White dots represent kinesin motors and green dots represent kinesin motors binding to microtubules in the right-hand figures.

3-2 Experimental Results and Discussion

In this experiment, biotinylated microtubules-based gold nanowires were investigated. In in-vitro motility assay experiments, Alexa 488 Streptavidin AuNP (10nm) was utilized to ensure that gold nanoparticles only bind along the microtubules. Fluorescence and scanning electron microscopy were performed for detailed observation and confirmation of the diameter size of the microtubules with AuNP in in vitro motility assay experiments. In the next sub sessions, the outcomes of this experiment will be discussed.

3-2.1 Observation of microtubule with AuNP particles under fluorescent microscopy

Fluorescence microscopy monitoring is carried out to visualize the biotinylated microtubules bind with Alexa 488 Streptavidin AuNP (10nm) gold nanoparticles in-vitro motility assay. In an in-vitro motility assay experiment, microtubules with gold nanoparticles were generated by varying the concentrations of biotinylated microtubules stock solutions and AuNP solutions to form a microtubules length of approximately 4-5 mm and a diameter of 25 nm. We discovered that the length of stable microtubules is dependent on the amount of taxol provided. The length of the microtubules was shown to be shorter than expected in (Fig 3-2.1 A). Furthermore, some microtubules generated white aggregates, as shown in (Fig 3-2.1 B). Because the incubation durations of the in-vitro motility solutions took a long time at

room temperature, these conditions were dependent on the concentration of taxol in motility solution 2 as indicated in chapter 2-2.3. In room temperature, the biotinylated tubulin and kinesin solutions are quick and easy to decompose. Finally, we investigated that a particular microtubule length operates after adjusting these conditions in our simulation (Fig 3-2.1 C and D). All of the results were examined using a fluorescence microscope.

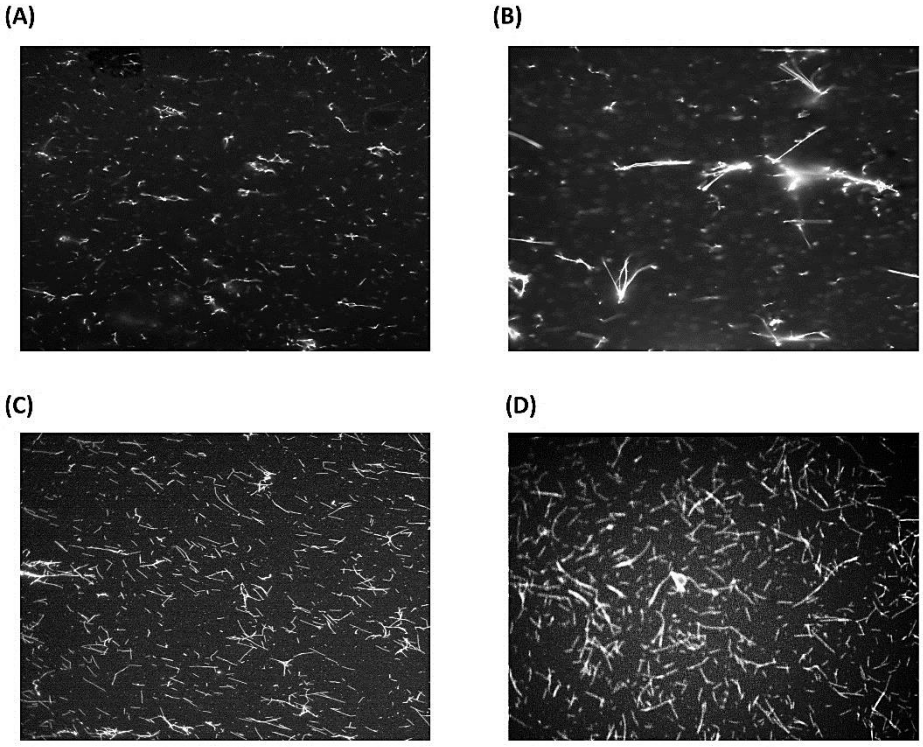

Figure 3-2.1: Observation of the microtubule behaviors under fluorescence microscopy.

3-2.2 Observation of microtubules with gold nanowires by SEM

3-2.2.1 Surface reorganization of the sample

A scanning electron microscope was used to analyze the microtubules, which were coated with gold nanowires. To proceed, we examined the sample stage settings using a scanning electron microscope, and we discovered that the electron beam must be focused at relevant positions on the samples. The edge of the samples under the electron beam is shown in the following sample images (Fig 3-2.2). White filamentous substances, as well as objects such as white spots or crystals, can be seen in the image. According to the conducted part of the samples' surface, we inferred the white filaments were microtubules and the white particles were gold nanoparticles (Fig 3-2.3 and Fig 3-2.4). The observation results at four different magnifications are represented in the SEM photographs.

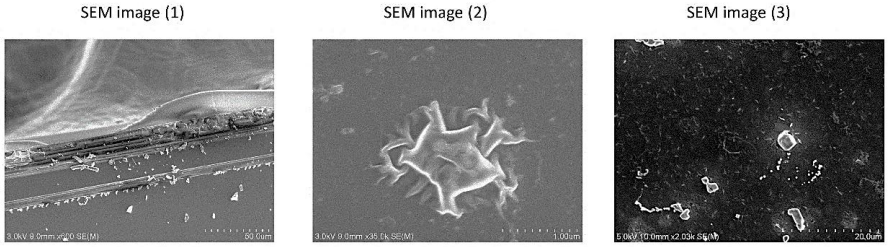

Figure 3-2.2: Sample surface reorganization under SEM. The three figures represent the sample area's edge.

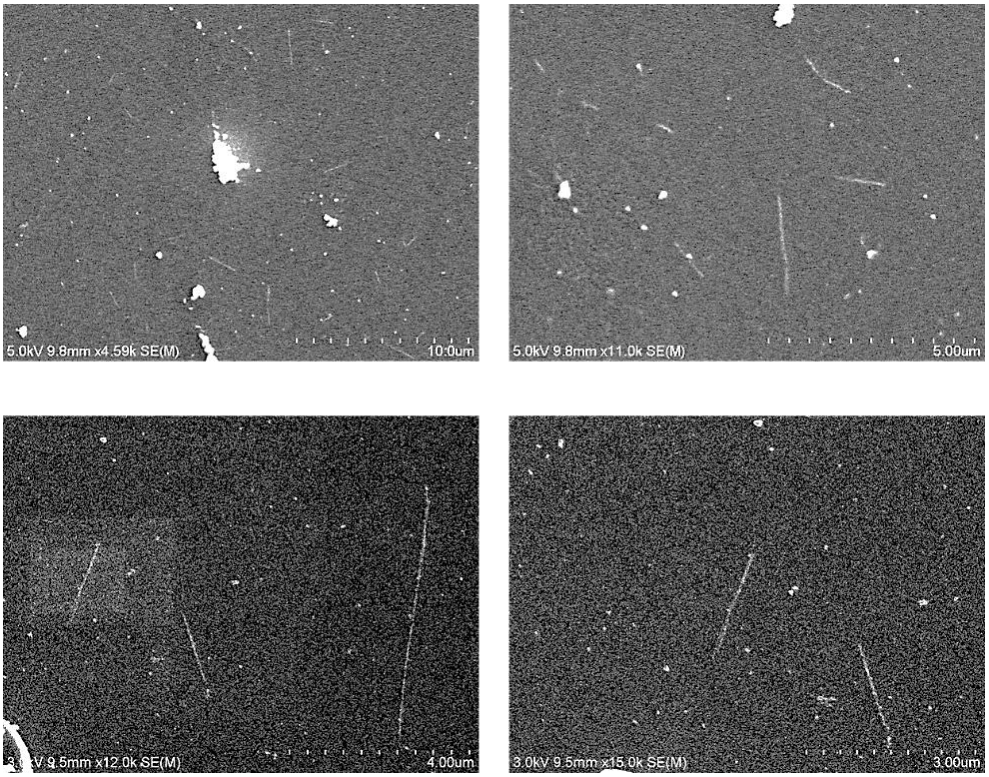

Figure 3-2.3: Sample surface reorganization under SEM. The electron beam conducted part of the samples' surface is shown in this diagram. The black surfaces represent the sample background, whereas the white lines denote the AuNP-coated microtubule filaments.

To investigate further details, we performed SEM observations for each pattern. It is considered that what seems to be a white filament is actually a microtubule, and what looks to be white particles is actually gold particles. The existence of gold particles on the microtubules was confirmed. It was determined whether the microtubules and gold particles visible in the SEM were actually microtubules and gold particles. The presence of a filamentous substance observable under a SEM microscope was investigated to see whether it was microtubule. Since, microtubules have an average length of 5 μm and a thickness of 25 nm. This time, we checked some of the filaments

observed by SEM to see if they had the typical shape of microtubules. Although (Fig 3-2.4) only shows a part of the microtubule filaments that could be seen, the filaments seen by SEM may be considered to be microtubules because all of the filaments visible had the same shape as those shown in the following pictures.

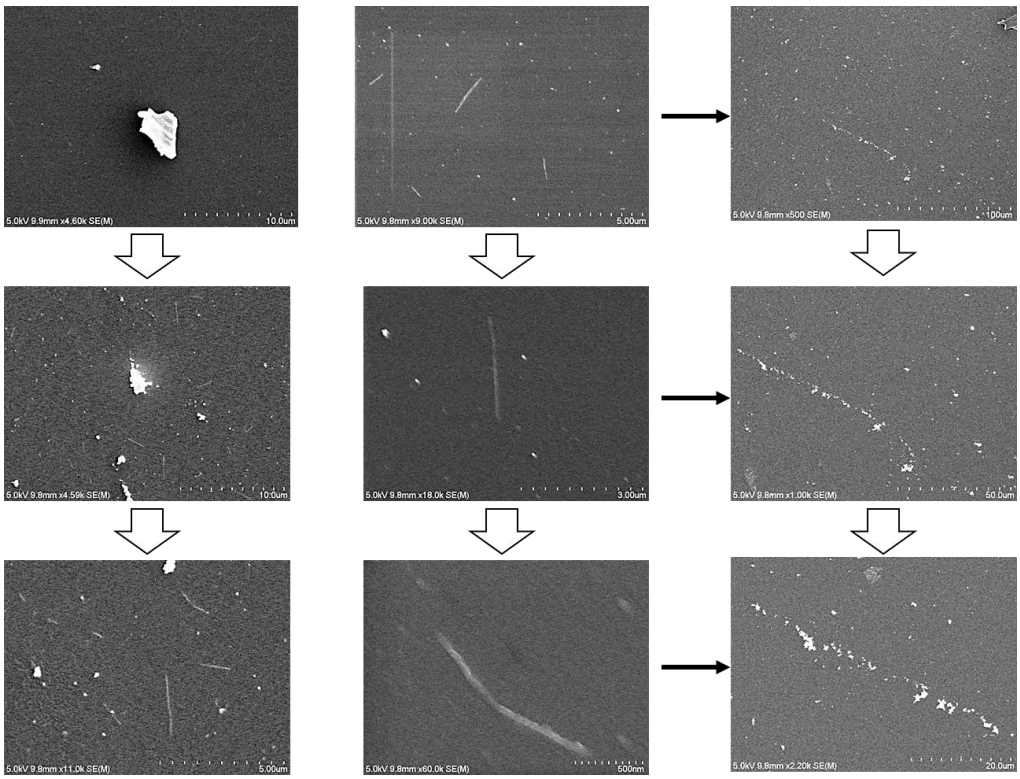

Figure 3-2.4: Confirmation of the microtubule filaments and AuNP in various pattern.

3-2.2.2 Quantitative measurement of the microtubules

In order to confirm that the white filamentous object in the figure (3-2.5) is a microtubule, the average length was calculated from several samples and found to be ≈ 3 - 4 μm. The diameter was around 40 nm. Microtubules

have an average length of 5 m and a thickness of 25 nm, and the shape of these items leads to the expectation that they are microtubules.

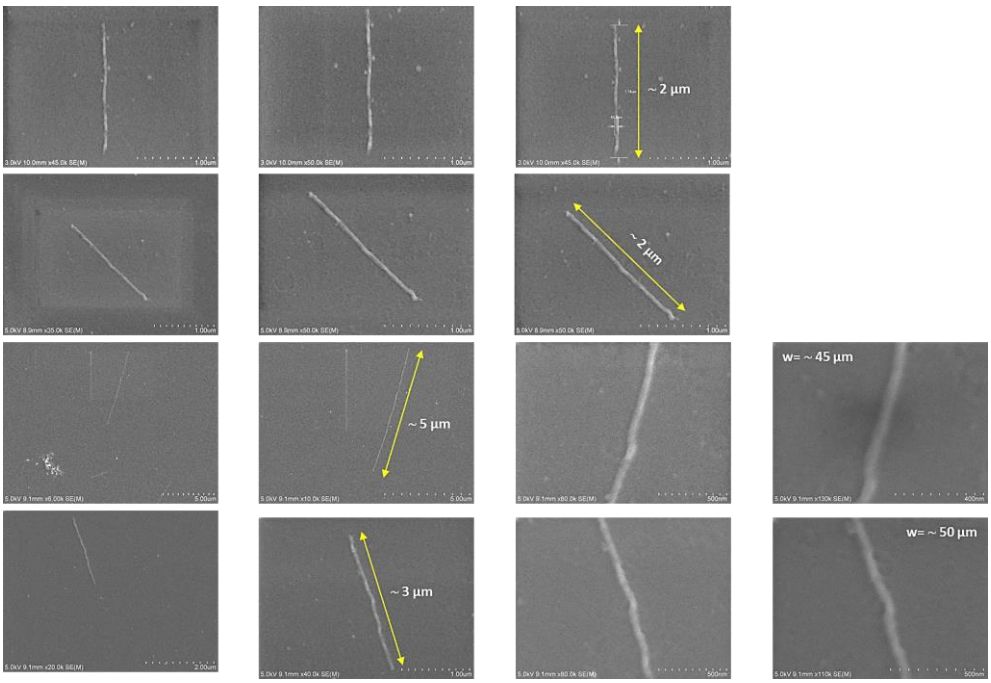

Figure 3-2.5: Quantitative measurement of the microtubule filaments at high magnification under SEM. In this figures, the yellow arrow lines indicate the length of the microtubules, while "w" represent the diameter of the microtubule at the right-hand side of the images.

3-2.3 Observation of gold nanoparticles by SEM

The SEM examination was done directly on the particles, which required for a more precise characterization of the actual particles. The samples were magnified with varied resolutions in the SEM measurement. Figures (3-2.6) show SEM images taken at a magnification of 100x, with gold nanoparticles to the left and right of the images. Adjusted the acceleration voltage and scanning time to magnify these particles under SEM conditions.

Because the electron beam exposure voltage was insufficient, these particles could not be detected at acceleration voltages of 1.0 kV or less. In SEM analysis, a lower voltage is appropriate for measuring the particles. However, detecting AuNP in an in-vitro motility assay sample containing microtubule filaments was too difficult. As a result, in this case, a high acceleration voltage is required. For example, in our detections, the acceleration voltage of a scanning electron beam was 5.0 kV or 7.0 kV. Again, the images show evidence of particle aggregation. In the magnified images, a substantial AuNP aggregate can be seen.

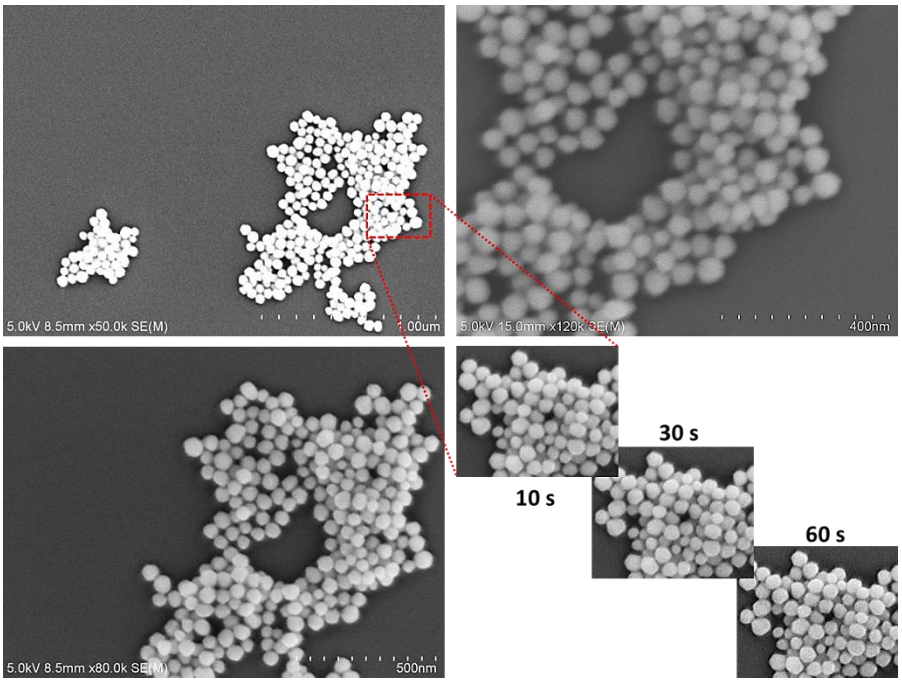

Figure 3-2.6: SEM images of aggregated gold nanoparticles on the surface at 100x magnification. The electron beam was accelerated at 5.0 kV and various scanning times were performed.

3-2.4 Detection of AuNP by EDX

Elemental analysis was performed using EDX (Energy-dispersive-Xray spectroscopy) to confirm that the white dots in the (Figure 3-2.7) are gold nanoparticles. Elemental analysis was performed at three points. (1) aggregated white points, (2) single white points, and (3) binding on microtubule white points. Figures shows the result of these performance. From the figure, it can be confirmed that the white dots are gold nanoparticles. From this result, it can be seen that some gold nanoparticles are attached to the microtubules, and some are not attached at all, and the concentration of the attached gold particles varies. Moreover, from the SEM image, it can be seen that many gold nanoparticles not attached to the microtubules are present on the substrate. Furthermore, since it can be confirmed that white dots are gathered to form relatively large dots, it is considered that gold nanoparticle may be attached to substances other than microtubules.

(A)

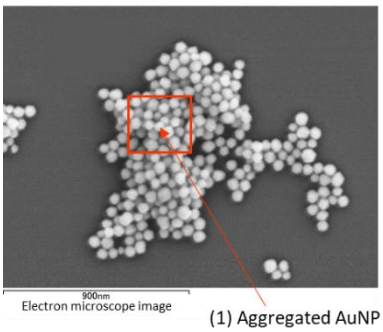
900nm
Electron microscope image
(1) Aggregated AuNP

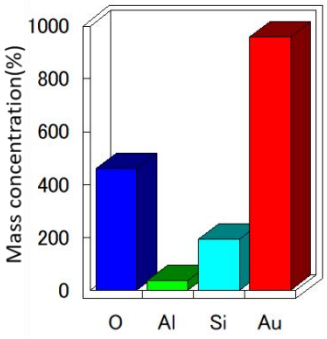
Mass concentration(%)
1000
800
600
400
200
0
O
Al
Si
Au

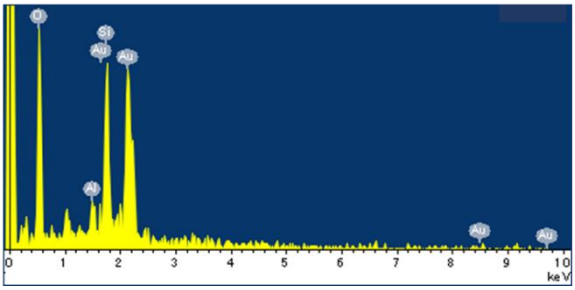
O
Si
Au
Au
Al
Au
Au
0
1
2
3
4
5
6
7
8
9
10
keV

(B)

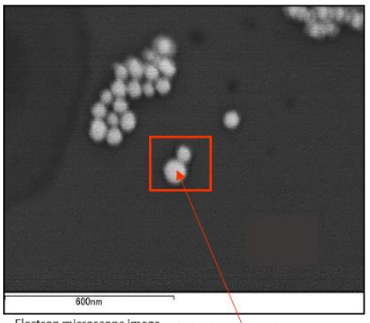
900nm
Electron microscope image
(2) Single point AuNP

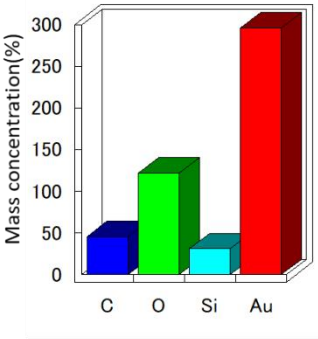
Mass concentration(%)
300
250
200
150
100
50
0
C
O
Si
Au

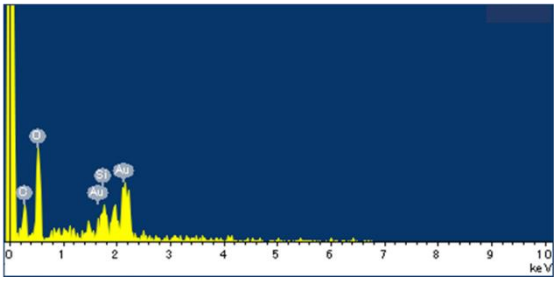
O
C
Si
Au
Au
0
1
2
3
4
5
6
7
8
9
10
keV

(C)

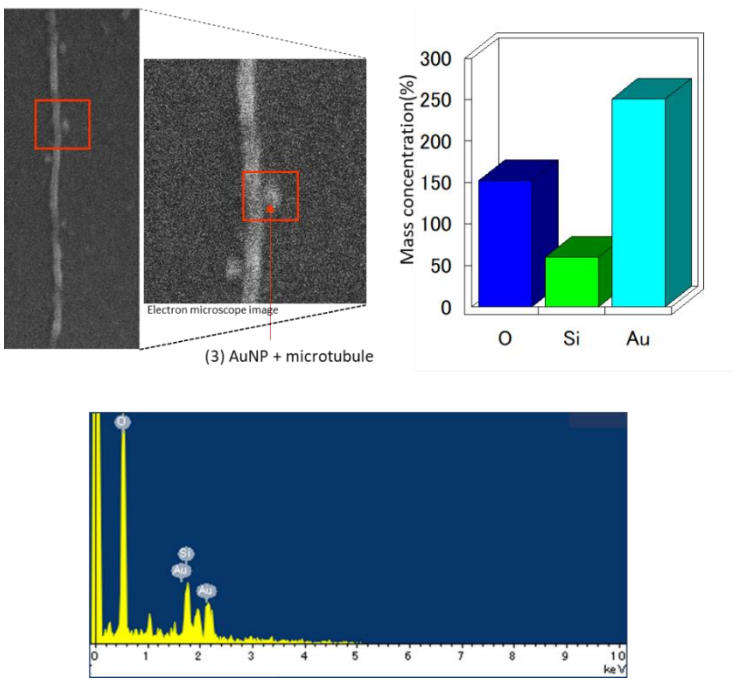

Figure 3-2.7: Identify the gold nanoparticles used EDX scanning. (A) The detection of aggregated AuNP is shown in the figure. (B) Indicate that only one particle, AuNP, was detected. (C) Gold nanoparticles recognized with in microtubule filament. The white spots were identified as gold nanoparticles in all of the investigations, as was expected.

Conclusion

In this research, we investigated in great detail mechanism of molecular shuttles driven by kinesin motors. We examined microtubule paths under external forces using a computer simulation that we developed by ourselves. The simulation research has a number of advantages over experimental ones. The simulation results were qualitatively in agreement with previous literatures. We have demonstrated that we can determine the path and filament persistence lengths of microtubules gliding over kinesin by

monitoring stochastic microtubule trajectories. The path persistence length of microtubules was measured using curvature analysis of microtubule trajectories. Then we calculated that path persistence length from the tip length of the microtubules. Through our analysis, we have found the path persistence length from the simulated results can significantly differ from the microtubule filament persistence length.

We observed that the path persistence length of gliding microtubules over kinesin coated surfaces can differ significantly from the microtubule filament persistence length, contrary to earlier theoretical predictions. This difference is due to fact that the fluctuating part of the microtubule during gliding over a kinesin-coated surface is much longer than the tip length. This happened because bound kinesin did not act as rigid anchors as opposed to the assumption in the theory that kinesins behave as rigid anchors. Our simulation showed that a significant difference between path persistence and filament persistence length can occur without considering the length dependent microtubule bending stiffness. As a result, the length-dependent MT bending stiffness is prerequisite to distinguish between the two persistence lengths. When measuring microtubule filament persistence length using gliding microtubule trajectories, the theoretical prediction that the path persistence length is equal to the filament persistence length may need to be taken into consideration.

The path persistence length was shown to be determined by both the mechanical properties of microtubules and the surface density of kinesin. Because the path persistence length of gliding microtubules over the kinesin-coated surface is an important parameter for determining the performance of molecular shuttle applications, the insights could be useful in designing and

predicting devices such as biosensors, biocomputation, and imagining or mapping of the surface. Ultimately, elucidation of the path persistence length would be helpful for better understanding of the biophysics and bioengineering.

We subsequently investigated we focused upon how microtubules behaved when high external forces were applied. The paths of the microtubules became detached when a larger external force was applied. Through the use of simulation, we discovered the detailed mechanism of the detachment of molecular shuttles driven by kinesin motors. Based on our findings, two types of microtubule detachment have been identified such as jumping and unzipping/swiveling.

We realized that jumping detachment is characterized by sudden shifts in microtubule position downstream of the external force without a significant change in direction. The sequential unbinding of kinesin motors from microtubules at either the leading or trailing ends is described as unzipping/swiveling. These types of observations could not be produced previously due to the limited space and time resolution in experiments.

From these observations, the two possible factors need to be considered to prevent microtubule detachment from track surfaces. The applied force should be less than that which generates a significant microtubule jump. When the microtubules are moving perpendicularly to the force, a high external force should not be applied to avoid unzipping/swiveling. This should be noted that when the applied force is greater, the molecular shuttles' movements are better controlled. The results are found to provide a good basis toward a more detailed understanding of the mechanism of molecular shuttle detachment.

Furthermore, we performed an experiment in which the gold nanowire was manufactured using the in-vitro motility assay method, and the presence of microtubules and gold nanoparticles was confirmed using SEM scans and EDX particle analyzation. The nanowires were made using biotinylated microtubules and Alexa 488 streptavidin gold nanoparticles in this work. By observing with SEM, we confirmed that gold nanoparticles were slightly attached to the microtubules. However, the adhesion rate of AuNP on microtubules was low, and a complete gold nanowires could not be produced. According to our observations, it is important to improve the sample preparation process in order to identify AuNP from EDX scanning results. Because the surface recognition of the samples should be uniformed under the SEM, the samples must be properly conducted with electron beams. Moreover, in order to prevent depolymerization of microtubules, the cleaning process for nanowire production must be improved such that the solution does not remain on the sample when dried. In this work, we were able to confirm the gold nano particles adhered to microtubules. To summarize, in order to obtain quantitative results, we also need to improve gold nanowire manufacturing and the particle identification method in the future.

Reference

[1] F. W. Commons, “File : Animal cell structure en . svg.”

[2] J. Howard, *Mechanics of Motor Proteins and the Cytoskeleton*. 2001.

[3] T. Wittmann, “Colorful cells,” *Colorful cells,* 2006.

[4] K. Svoboda, C. F. Schmidt, B. J. Schnapp, and S. M. Block, “Direct observation of kinesin stepping by optical trapping interferometry,” *Nature*, vol. 365, no. 6448, pp. 721–727, 1993, doi: 10.1038/365721a0.

[5] D. L. Coy, M. Wagenbach, and J. Howard, “Kinesin takes one 8-nm step for each ATP that it hydrolyzes,” *J. Biol. Chem.*, vol. 274, no. 6, pp. 3667–3671, 1999, doi: 10.1074/jbc.274.6.3667.

[6] K. Kawaguchi, “Energetics of kinesin-1 stepping mechanism,” *FEBS Lett.*, vol. 582, no. 27, pp. 3719–3722, 2008, doi: 10.1016/j.febslet.2008.10.019.

[7] M. Heuvel and C. Dekker, “Motor Proteins at Work for Nanotechnology,” *Science*, vol. 317, pp. 333–336, Aug. 2007, doi: 10.1126/science.1139570.

[8] T. Yanagida, M. Nakase, K. Nishiyama, and F. Oosawa, “Direct observation of motion of single F-actin filaments in the presence of myosin,” *Nature*, vol. 307, no. 5946, pp. 58–60, 1984, doi: 10.1038/307058a0.

[9] J. Howard, A. J. Hunt, and S. Baek, “Chapter 10 Assay of Microtubule Movement Driven by Single Kinesin Molecules,” *Methods Cell Biol.*, vol. 39, no. C, pp. 137–147, Jan. 1993, doi: 10.1016/S0091-679X(08)60167-3.

[10] H. Hess, “Engineering Applications of Biomolecular Motors,” *Annu. Rev. Biomed. Eng.*, 2011.

[11] A. Goel and V. Vogel, “Harnessing biological motors to engineer

systems for nanoscale transport and assembly," *Nat. Nanotechnol.*, vol. 3, no. 8, pp. 465–475, 2008, doi: 10.1038/nnano.2008.190.

[12] A. Agarwal and H. Hess, "Biomolecular motors at the intersection of nanotechnology and polymer science," *Prog. Polym. Sci.*, vol. 35, no. 1–2, pp. 252–277, 2010, doi: 10.1016/j.progpolymsci.2009.10.007.

[13] G. D. Bachand, N. F. Bouxsein, V. Vandelinder, and M. Bachand, "Biomolecular motors in nanoscale materials, devices, and systems," *WIREs Nanomed Nanobiotechnol*, vol. 6, pp. 163–177, 2014, doi: 10.1002/wnan.1252.

[14] G. Saper and H. Hess, "Synthetic Systems Powered by Biological Molecular Motors," *Chem. Rev.*, vol. 120, no. 1, pp. 288–309, 2020, doi: 10.1021/acs.chemrev.9b00249.

[15] C. T. Lin, M. T. Kao, K. Kurabayashi, and E. Meyhofer, "Self-contained, biomolecular motor-driven protein sorting and concentrating in an ultrasensitive microfluidic chip," *Nano Lett.*, vol. 8, no. 4, pp. 1041–1046, 2008, doi: 10.1021/nl072742x.

[16] M. Lard *et al.*, "Ultrafast molecular motor driven nanoseparation and biosensing," *Biosens. Bioelectron.*, vol. 48, pp. 145–152, 2013, doi: 10.1016/j.bios.2013.03.071.

[17] T. Fischer, A. Agarwal, and H. Hess, "A smart dust biosensor powered by kinesin motors," *Nat. Nanotechnol.*, vol. 4, no. 3, pp. 162–166, 2009, doi: 10.1038/nnano.2008.393.

[18] D. V. Nicolau *et al.*, "Parallel computation with molecular-motor-propelled agents in nanofabricated networks," *Proc. Natl. Acad. Sci. U. S. A.*, vol. 113, no. 10, pp. 2591–2596, 2016, doi: 10.1073/pnas.1510825113.

[19] M. G. L. Van Den Heuvel and C. Dekker, "Motor proteins at work for nanotechnology," *Science (80-.).*, vol. 317, no. 5836, pp. 333–336, 2007, doi: 10.1126/science.1139570.

[20] Y. Ishigure and T. Nitta, “Understanding the Guiding of Kinesin/Microtubule-Based Microtransporters in Microfabricated Tracks,” *Langmuir*, vol. 30, no. 40, pp. 12089–12096, Oct. 2014, doi: 10.1021/la5021884.

[21] F. Gittes, B. Mickey, J. Nettleton, and J. Howard, “Flexural rigidity of microtubules and actin filaments measured from thermal fluctuations in shape,” *J. Cell Biol.*, vol. 120, no. 4, pp. 923–934, 1993, doi: 10.1083/jcb.120.4.923.

[22] J. Clemmens *et al.*, “Mechanisms of microtubule guiding on microfabricated kinesin-coated surfaces: Chemical and topographic surface patterns,” *Langmuir*, vol. 19, no. 26, pp. 10967–10974, 2003, doi: 10.1021/la035519y.

[23] F. Gibbons, J. F. Chauwin, M. Despósito, and J. V. José, “A dynamical model of kinesin-microtubule motility assays,” *Biophys. J.*, vol. 80, no. 6, pp. 2515–2526, 2001, doi: 10.1016/S0006-3495(01)76223-6.

[24] F. Nedelec and D. Foethke, “Collective Langevin dynamics of flexible cytoskeletal fibers,” *New J. Phys.*, vol. 9, no. March 2017, 2007, doi: 10.1088/1367-2630/9/11/427.

[25] M. G. L. Van Den Heuvel, M. P. De Graaff, and C. Dekker, “Microtubule curvatures under perpendicular electric forces reveal a low persistence length,” *Proc. Natl. Acad. Sci. U. S. A.*, vol. 105, no. 23, pp. 7941–7946, 2008, doi: 10.1073/pnas.0704169105.

[26] N. Isozaki, H. Shintaku, H. Kotera, T. L. Hawkins, J. L. Ross, and R. Yokokawa, “Control of molecular shuttles by designing electrical and mechanical properties of microtubules,” *Sci. Robot.*, vol. 2, no. 10, pp. 1–11, 2017, doi: 10.1126/scirobotics.aan4882.

[27] J. Howard, *Mechanics of motor proteins and the cytoskeleton*. Sinauer Associates, Inc., 2001.

[28] M. G. L. Van Den Heuvel, S. Bolhuis, and C. Dekker, “Persistence length

measurements from stochastic single-microtubule trajectories," *Nano Lett.*, vol. 7, no. 10, pp. 3138–3144, 2007, doi: 10.1021/nl071696y.

[29] I. Cytoskeleton, "Biotin Labeled Tubulin," no. 303, pp. 1–2.

[30] "Alexa Fluor™ 488 Streptavidin, 10 nm colloidal gold conjugate." .

[31] J. D. Zahn, "Methods in Bioengineering - Biomicrofabrication and BioMicrofluidics," *Bioengineering*. p. 367, 2010, [Online]. Available: https://books.google.com/books?id=0t6X82OGvJYC&pgis=1.

[32] J. Y.-T. K. Ming-Ju Chen, Kreuter, "Nanoparticles and microparticles for drug and vaccine delivery.," *J. Anat.*, vol. 189 (Pt 3, no. Ii, pp. 503–505, 1996, doi: 10.1002/bit.

[33] "FisherbrandPremium Plain Glass Microscope Slides Type_ plain glass; Size_ _ Fisher Scientific." .

[34] L. J. Juszczak, "Parafilm M," *Newsletter (Western Association for Art Conservation)*, vol. 2, no. 3. pp. 1–2, 1980.

[35] Olympus, "Olympus IX71 inverted microscopes," p. 30, 2015.

[36] C. S. Series and C. Scientific, "Thorlabs CS2100M Compact Scientific Cameras."

[37] "X-Cite XLED1 Multi-Triggering LED Illumination System _ Excelitas." .

[38] "Molecular Biology of the Cell (4th Ed)," *Journal of Biological Education*, vol. 37, no. 1. pp. 45–47, 2002, doi: 10.1080/00219266.2002.9655847.

[39] H. H. Corporation and P. No, "Instruction Manual for Model S-4800 Field Emission," *Microscope*, no. 539, 2002.

[40] H. Lymphocyte, "Introduction of Osmium Plasma Coater 1. Principle," pp. 1–3.

[41] T. Duke, T. E. Holy, and S. Leibler, "'Gliding Assays' for Motor Proteins: A Theoretical Analysis," *Phys. Rev. Lett.*, vol. 74, no. 2, pp. 330–333, Jan. 1995, doi: 10.1103/PhysRevLett.74.330.

[42] T. Nitta and H. Hess, “Dispersion in active transport by kinesin-powered molecular shuttles,” *Nano Lett.*, vol. 5, no. 7, pp. 1337–1342, 2005, doi: 10.1021/nl050586t.

[43] R. R. Agayan *et al.*, “Optimization of Isopolar Microtubule Arrays,” *Langmuir*, vol. 29, no. 7, pp. 2265–2272, Feb. 2013, doi: 10.1021/la303792v.

[44] A. Kis *et al.*, “Nanomechanics of Microtubules,” *Phys. Rev. Lett.*, vol. 89, no. 24, pp. 1–4, 2002, doi: 10.1103/PhysRevLett.89.248101.

[45] F. Pampaloni, G. Lattanzi, A. Jonáš, T. Surrey, E. Frey, and E. L. Florin, “Thermal fluctuations of grafted microtubules provide evidence of a length-dependent persistence length,” *Proc. Natl. Acad. Sci. U. S. A.*, vol. 103, no. 27, pp. 10248–10253, 2006, doi: 10.1073/pnas.0603931103.

[46] V. VanDelinder, Z. I. Imam, and G. Bachand, “Kinesin motor density and dynamics in gliding microtubule motility,” *Sci. Rep.*, vol. 9, no. 1, pp. 1–10, 2019, doi: 10.1038/s41598-019-43749-8.

[47] J. Howard, A. J. Hudspeth, and R. D. Vale, “Movement of microtubules by single kinesin molecules,” *Nature*, vol. 342, no. 6246, pp. 154–158, 1989, doi: 10.1038/342154a0.

Appendix

In section 2.4 of Chapter 2, we used the access this information by Van den Heuvel et al. to calculate the radius of curvature of the microtubules under external forces in order to determine the path persistence length from the simulation path.

$$y\,(x) = R_0\, cos^{-1}\left(e^{-\frac{x}{R_0}}\right), \qquad \text{(a)}$$

$$R_0 = \frac{3k_B T L_p}{f\langle d\rangle^2}, \qquad \text{(b)}$$

where $\langle d\rangle$ is the average length of bending part of MTs, k_B is Boltzmann constant, T is absolute temperature, f is external applied force density. As we will observe later, L_p is either path or filament persistence lengths. R_0 are radii of the curvature of microtubule (MT).

We obtain at eq (a), which considers the MT tip's bending. In Figure 1, we calculated the average microtubule trajectory when the force density f_e was directed along the x-axis (a). The MT's path coordinates s, θ are shown in Fig (a).

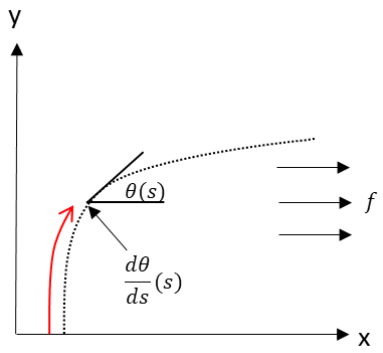

Fig (a). MT trajectory along the x-axis with force density f .The trajectory is represented by the path coordinates θ, s.

The microscopic bending of the MT tip $\theta'_m(s)$ is related to the average curvature of the MT path $\langle d\theta/ds \rangle$ as indicated in eq (a1) in Fig (b).

$$\langle \frac{d\theta}{ds}(s) \rangle \approx \langle \frac{\theta'_m(s)}{d} \rangle \qquad \text{(a1)}$$

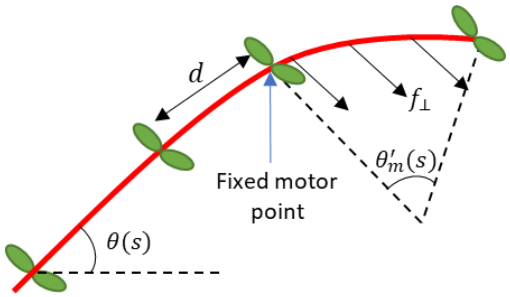

Fig (b). The microscopic bending of the MT tip θ'_m under the perpendicular force $f_\perp$ which magnitude depends on the MT's orientation, is used to explain the macroscopic route trajectory $\theta(s)$.

The material properties of the MT tip are related to its microscopic bending. We need to calculate the microscopic bending $\theta'_m(s)$ due to an external perpendicular force $f_\perp = f_e sin\theta(s)$ to determine the macroscopic $\theta(s)$. The bending of the free tip d fixed in position and orientation $(\theta' = 0)$ at the origin as shown in Fig (c). The microscopic tip curvature as a function of the bending momentum $M(s')$ as follows eq (a2).

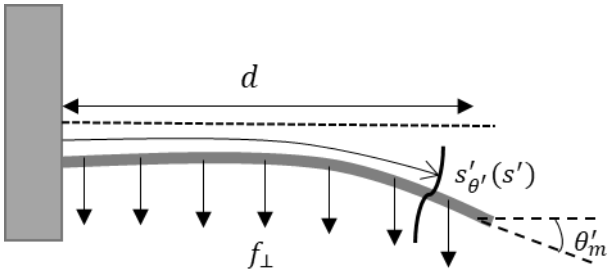

Fig(c). Bending of the tip in microscopic coordinates θ', $\theta s'$.

$$\frac{d\theta'}{ds'} = -\frac{M(s')}{EI} \qquad \text{(a2)}$$

where E is the bending modulus, I is the second moment of inertia.

On a cross section of the tip segment of length $(\langle d \rangle - s')$, we calculate the internal shear force $F(s')$ and internal bending momentum $M(s')$ as shown in Fig (d).

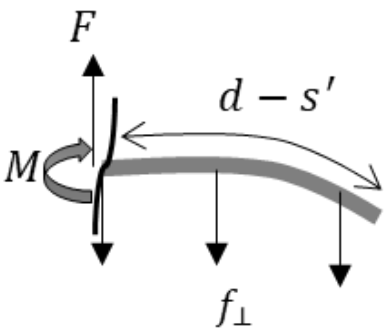

Fig(d). Internal shear force F and bending momentum M as a function of location s' in a free-body diagram of the MT tip.

From force balance, $F(s') = f_{\perp}(d - s')$ and from the momentum balance, $M(s') = -\frac{f_{\perp}}{2}(d - s')^2$. By substituting $M(s')$ into eq (a2) we get the following expression for the bent tip shape in eq (a3).

$$\frac{d\theta'}{ds'} = \frac{f_{\perp}}{2EI}(d - s')^2 \quad \text{(a3)}$$

By integrating the eq (a3) of the bent tip shape, solve this eqs with the boundary condition of' $\theta'(0) = 0$ to $\theta'(s')$ as follows.

$$\int_0^{s'} \frac{d\theta'}{ds'} ds' = \int_0^{s'} \frac{f_{\perp}}{2EI}(d - s')^2 \, ds' \quad \text{(i)}$$

$$\theta'(s') - \theta'(0) = \frac{f_{\perp}}{2EI} \frac{1}{3} [(d - s')^3(-1)]_0^{s'} \quad \text{(ii)}$$

$$\theta'(s') = \frac{f_{\perp}}{6EI} [(d - s')^3(-1) + d^3] \quad \text{(iii)}$$

$$\theta'(s') = \frac{f_{\perp}}{6EI} [-(d^3 - 3d^2 s' + 3d(s')^2 - (s')^3) + d^3] \quad \text{(iv)}$$

$$\theta'(s') = \frac{f_{\perp}}{6EI}(s'^3 - 3ds'^2 + 3d^2 s') \quad \text{(v)}$$

By deriving the eqs (i to v), the shape of the MT bent tip becomes the eq (a4).

$$\theta'_m = \frac{f_{\perp} d^3}{6EI} \quad \text{(a4)}$$

Substituting this into eq (a1), we get the following local curvature of the MT trajectory in eq (a5).

$$\left\langle \frac{d\theta}{ds} \right\rangle = \left\langle \frac{f_e d^2}{6EI} sin\theta \right\rangle \quad \text{(a5)}$$

The tip length d are exponentially distributed $\langle d^2 \rangle$ of an exponential distribution with mean $\langle d \rangle = 2\langle d \rangle^2$, when the right-hand site is averaged. This conclusion, as combined with the elastic rod theory $EI = k_B Tp$, proves that the substitution in eq (a6).

$$\langle \frac{d\theta}{ds} \rangle = \frac{f_e \langle d \rangle^2}{3k_b Tp} sin\theta \quad \text{(a6)}$$

Express the path curvature in cartesian coordinates,

$$\frac{d\theta}{ds} = \frac{1}{\left[1+\left(\frac{dy}{dx}\right)^2\right]^{3/2}} \frac{d^2y}{dx^2} \quad \text{(a7)}$$

We'll solve the trajectory of an MT that originates at the origin and moves along the x-axis, with force density along the y-axis.

$$\cos(\theta) = \left[1 + \left(\frac{dy}{dx}\right)^2\right]^{-1/2} \quad \text{(vi)}$$

By using differential equation (vi) to describe the MT trajectory in equation (a8).

$$\frac{d^2y}{dx^2} = \left[1 + \left(\frac{dy}{dx}\right)^2\right] \frac{f_e \langle d \rangle^2}{3k_b Tp} \quad \text{(a8)}$$

Using the initial condition $\frac{dy}{dx}|_0 = 0$, $y(0) = 0$ to solve the equations, we find that eq (vii).

$$y(x) = -R_0 \ln\left(cos \frac{x}{R_0}\right) \quad \text{(vii)}$$

We get the eq by changing the x and y coordinates as shown in Fig (a).

$$y\,(x) = R_0\, cos^{-1}\left(e^{-\frac{x}{R_0}}\right) \quad \text{(a)}$$

In order to determine the path persistence length from the simulation path, this eq(a) represents the radius of curvature of the microtubules under external forces.